DEVELOPMENT OF A THICK GAS ELECTRON MULTIPLIER-BASED MULTI-ELEMENT MICRODOSIMETRIC DETECTOR

DEVELOPMENT OF A THICK GAS ELECTRON MULTIPLIER-BASED MULTI-ELEMENT MICRODOSIMETRIC DETECTOR

By ZAHRA ANJOMANI, M.Sc., B.Sc.

A Thesis Submitted to the School of Graduate Studies in Partial Fulfilment of the Requirements for the Degree Doctor of Philosophy

DOCTOR OF PHILOSOPHY (Medical Physics) (2017)

McMaster University, Hamilton, Ontario

TITLE: Development of a Thick Gas Electron Multiplier-based Multi-element Microdosimetric Detector

AUTHOR: Zahra Anjomani, M.Sc. (Nuclear Engineering, Shahid Beheshti University)

SUPERVISOR: Dr. Soo-Hyun Byun

NUMBER OF PAGES: xviii, 168

Dedicated to

my husband and best friend, ***Omid Moeini****.*

Abstract

Tissue Equivalent Proportional Counters (TEPCs) are considered the standard instrument for microdosimetry, aiming at measuring the distribution of the energy deposited by ionizing radiation in a micrometric target, and have been employed for a number of radiation physics, radiation protection and radiation biology applications.

This study describes development procedure and performance of a novel multi-element TEPC. Following an extensive Geant4 simulation study, an advanced prototype multi-element gaseous microdosimetric detector was developed using the Thick Gas Electron Multiplier (THGEM) technique. The multi-element design was employed to increase the neutron detection efficiency. The prototype THGEM multi-element detector consists of three alternating layers of tissue equivalent plastic hexagons and each layer houses a hexagonal array of seven cylindrical gas cavity elements with equal heights and diameters of 17 mm. The final detector structure incorporates 21 gaseous volumes. Owing to the absence of wire electrodes, the THGEM multi-element detector offers flexible and convenient fabrication in contrast to the traditional wire-based methods. The detector responses to neutron and gamma-ray were investigated using the McMaster Tandetron ^{7}Li(p,n) neutron source. The dosimetric performance of the detector is presented in contrast to the response of a commercial tissue equivalent proportional counter. The collected spectra exhibit the expected features of the lineal energy distributions for given proton beam energies. Compared to the 2 inch TEPC response, the detector gave a consistent microdosimetric response with a maximum discrepancy of 15% in measured neutron absorbed dose. An improvement of a factor of 3.0 in neutron detection efficiency has been accomplished. The prototype detector offers a simple fabrication process and provides the fundamental basis for development of a high efficiency TEPC dedicated for monitoring weak neutron radiation fields.

Acknowledgements

I would like to extend my sincerest thanks to my supervisor, Dr. Soo-Hyun Byun. I am deeply grateful for giving me the opportunity to work on such an interesting and exciting topic. I enjoyed every second of it and learned a lot from you. Your extensive knowledge and experience gave me constant support and encouragement during my research. Your positive attitude provided me the initial orientation and greatly motivated my work and were essential to its completion.

I would like to thank my committee members, Dr. David Chettle, Dr. Anthony J. Waker and Dr. William V. Prestwich for their insightful comments and encouragements that provided me with a better understanding of the physical aspects of my research. In particular, thanks to Dr. William V. Prestwich for his encouragement, discussions and help in the revision of this manuscript.

Special thanks to Justin Bennett and Scott McMaster for running the Tandem accelerator and for their patience and dedication when training me to operate the accelerator on my own.

I want to thank my office mates and friends at TAB104C: Eric Johnston, Erica Dao, Nourhan Shalaby, Richard Garnett, Matthew Bernacci and Matthew Wong for making our office a nurturing, healthy and friendly space. Erica thanks for your endless positive energy and Eric thanks for all those long discussions.

To my mother whose endless love and support has always been a great source of inspiration for me. Thank you for being the lighthouse of my life. To my father, even though he is not physically with us anymore, I will always keep his spirit and wisdom deep in my heart.

To Omid, the love of my life. I can only say that I am very lucky for having you by my side. Thank you for encouraging me to push myself and always reach for greater goals.

Contents

List of Figures

Chapter 1

General Introduction

1.1 History and Objectives

For dosimetry in radiation fields of low count rates such as those encountered in radiation protection applications, detectors with high counting efficiency are desired. Neutron survey instruments, conventionally known as rem counters or rem meters, are routinely used for real-time neutron measurements. The operational quantity to be measured is the ambient dose equivalent H*(10) [1] that in general gives a conservative approximation to the primary limiting quantity effective dose [2]. The ambient dose equivalent is defined by the International Commission on Radiation Units and Measurements (ICRU) as the dose equivalent at 10 mm depth in the 30 cm diameter ICRU tissue equivalent sphere, irradiated by a parallel beam. The quantity dose equivalent is defined by the product of the absorbed dose D and a quality factor Q which takes into account the relative biological effectiveness of a radiation beam. The fluence to H*(10) conversion coefficients are calculated [3] and tabulated in ICRP report 74 [4]. The ratio of the detector reading to the true ambient dose equivalent is known as the ambient dose equivalent response. An ideal survey meter would have a response value of unity for all neutron energies.

Different approaches have been used in order to obtain relevant dosimetric information

in radiation protection. Among them, the two methods that are commonly used are either based on moderator based rem meters or microdosimetry techniques. The latter specifically has drawn more attention with the advancement in microelectronics and the ICRP [5] decision in defining the quality factor Q as a function of linear energy transfer LET [6, 7].

The first method involves moderating techniques to compensate for the inherently low detection efficiency of the available thermal neutron detectors for fast neutrons [8]. This principle was used by Almaldi [9] a few years after the discovery of neutrons in 1930. Conventional moderator based rem meters basically consist of a thermal neutron detector at the centre of a spherical or cylindrical moderator. Fast neutrons are moderated by passing through a polyethylene layer and then detected by a thermal neutron detector. In the original designs, LiI scintillators were used by Bramblett [10] and Leake [11] as the thermal neutron detectors that were replaced by BF_3 or ^3He proportional counters in further modifications of the counters designs to minimize the response of the detector to gamma radiations [12, 13]. The final detector configuration parameters such as the size of the moderator are optimized so that the detector reading over the energy range of interest approximates closely the fluence to $H^*(10)$ conversion coefficient curve. To this end, some designs employ internal neutron absorber layers to further tune the detector response [14]. The standard moderator based rem meters, such as the Leake counter [13, 15] or the Andersson–Braun type [14], are the most widely used detectors for real-time neutron dose monitoring at workplaces owing to their high detection efficiency.

The second approach is based on the principles of experimental microdosimetry. Given the fact that the radiobiological effectiveness of radiation strongly depends on the energy deposition pattern in the biological tissue, the intent of microdosimetry is to define the energy depositions that occur in micro-volumes on the order of cellular and sub-cellular structures [16], most often with the means of a tissue equivalent proportional counter (TEPC). The foundation of the experimental dosimetry and

principle properties of a TEPC were established in 1955 by Harald H. Rossi [17]. The low pressure proportional counters have been developed in a way that permits measurements of microdosimetric quantities at scales of the order of 1 μm. The detector wall and filling gas are made of tissue equivalent materials. The simulation of interactions and energy depositions in a microscopic tissue volume can be achieved by adjusting the pressure of the filling gas. A TEPC-based instrument measures the pulse height spectrum of energy deposition events. The collected pulse amplitudes are proportional to the size of energy deposition events and after calibration are expressed in terms of a lineal energy distribution from which the absorbed dose distribution can be obtained. The lineal energy is a microdosimetric quantity defined as the deposited energy in a volume by a single event divided by the volume mean chord length. The lineal energy is closely related to the LET of the secondary charged particles produced through neutron and photon induced reaction in the detector wall and filling gas. From the measured absorbed dose distributions, the mean quality factor and dose equivalent can be obtained. Moreover, in mixed neutron gamma radiation fields, the diagnostic properties of the absorbed dose distributions can be used to evaluate neutron and gamma absorbed dose fractions simultaneously [6, 18, 19]. These are the most appealing advantages of the experimental microdosimetry techniques in neutron radiation protection applications [6]. TEPC-based neutron monitors have been applied for measuring neutron dose distributions at nuclear power plants, proton therapy accelerators, aircraft, etc [20–26].

The two methods described above present different approaches to measure radiation protection quantities and each has its own limitations. Several publications report the use and intercomparison of the aforementioned methods [27–32].

The shortcomings associated with the conventional moderator-based rem meters are summarized by Rogers [33]. The heavy weight of the area monitors due to their massive moderator and the strong energy dependence of the detector dose equivalent response remain the major disadvantages of the moderator based devices for radiation protection

purposes [7, 34]. Particularly, the instruments tend to overestimate significantly the dose equivalent at intermediate neutron energies (below 100 keV) and the detection efficiency drops rapidly for the energy region above 9 MeV [35]. Moreover, for real-time field measurements they are usually calibrated in terms of dose equivalent in a reference radiation field. Given the fact that in practice most workplace fields such as those encountered in the nuclear power plants or near medical accelerators are broad range with neutron energies extending from thermal to several MeV, a single calibration source and geometry is not particularly suitable and can introduce large uncertainties in measurements as the instrument response depends strongly on energy [36].

Microdosimetric methods on the other hand have the advantage in providing information on the quality of the radiation beam and evaluating ambient dose equivalent due to neutrons and photons [6]. Although the complexity of microdosimetric instrumentation and data acquisition systems hampered the routine implementation of microdosimetric methods in operational health physics, it is generally accepted that TEPC-based radiation protection instruments provide the most elaborate and closest approach to realizing the radiation protection quantities as described by ICRU and ICRP guidelines [37]. However, TEPC-based instruments underestimate the ambient dose equivalent for low neutron energies (below 300 keV). In a study by Kawecka, Morstin and Booz [38], it was demonstrated that with respect to the ordinary TEPCs, known as Rossi counters, the detector properties such as the wall thickness can be optimized so that the detector dose equivalent reading fairly matches the $H^*(10)$ curve (see subsection 2.3.5). Further improvements in the dose equivalent response for the neutron energies below a few hundred keV can be achieved by operating the detectors at lower gas pressures [38]. To the same end, the material composition of the filling gas can be modified by adding small amounts of additives that are sensitive to thermal neutrons such as ^{3}He as is described by Pihet et al. [39].

Various groups have developed TEPC-based dose equivalent meter prototypes and their dosimetric properties have been investigated and intercompered in various radi-

ation fields of monoenergetic neutron beams with the energy ranging from thermal to 15 MeV, as well as workplace environments [28, 30, 32, 40]. Generally, compared to the conventional moderator-based rem meters, TEPC-based area monitors showed a smaller energy dependence [7, 30, 40]; however, the need for further improvements, particularly for the low neutron energy region, is likely to be continued [37].

Another problem that needs to be addressed for routine implementation of the conventional TEPC-based dosemeters for real-time neutron monitoring, is the fact that they generally suffer from low neutron detection efficiency. This is due to the low elastic scattering cross section of the interaction between neutrons and the TEPC detector. In an assessment of the application of TEPCs in the CANDU (CANadian Deuterium Uranium) nuclear power plant environment, Waker et al. [20] have shown that although microdosimetric methods can be applied to power plant neutron monitoring, the detection efficiency of the commercially available systems is not satisfactory and physically large TEPCs (12.7 cm in diameter and more) are required.

As discussed by Kliauga, Waker and Barthe [41], the detection efficiency of a spherical TEPC in terms of counts per unit dose is proportional to the square of the counter diameter or the surface area of the sensitive volume. Therefore, to increase the detection efficiency one can increase the detector sensitive volume size. For example, to obtain an efficiency comparable to a SNOOPY dosemeter [14, 42], a representative moderator-based instrument having an efficiency of 800 [counts/μSv], a TEPC with a diameter of about 28 cm is required [35]. Although it is technically not challenging to manufacture such a large size of TEPC detector, it will end up diminishing the advantages of TEPC.

To increase the surface area of the gaseous sensitive volume, without increasing the physical dimensions of the detector, so called "multi-elements" structures have been employed. This is based on the fact that the neutron interactions with the detector wall contribute predominantly to fast neutron detection in TEPCs in a wide energy region. For a fixed detector volume, the effective surface area of detector can be

increased by subdividing the sensitive volume into many smaller volumes, known as sub-elements. This idea was first proposed by Rossi [43] for monitoring low dose-rate mixed field exposures and later, a multi-element proportional counter was reported by Kliauga et al. [44]. This counter consists of 296 cylindrical sub-elements arranged in a hexagonal array in the alternative layers of TE plastic discs. In spite of the enhanced neutron detection efficiency, there are notable limitations with this design in terms of the detector fabrication aspect. The counter incorporates thirty seven stainless steel wires of 0.0635 mm diameter as anodes. To hold all the components in place additional structural components such as the anode wire support system are required [41]. Moreover, the electric field at the ends of each cylindrical cavity tends to be non-uniform [43], which requires field shaping septa [44], field tubes [45] or guard rings to eliminate the edge effects and keep the multiplication process spatially uniform. These efforts were demonstrated to be effective but resulted in a complicated fabrication process. The assembly process becomes even more tedious whenever more reduction in the size of the counter is required [45].

The aforementioned difficulties justify the efforts to develop a new type of TEPC-based dosemeter without any wire electrode. In the past two decades, a variety of gaseous micropattern detectors have been introduced. Among them, the most innovative are the MicroMegas, microstrip detectors and Gas Electron Multipliers (GEMs) [46–48]. Both microstrip and GEM detectors are wireless structures, in which an avalanche electric field is produced through using either alternating electrodes of fine strips or a hole-type structure.

To investigate the feasibility of modern tissue equivalent proportional counters for microdosimetry, Farahmand et al. employed a standard GEM detector [49] containing five cylindrical sensitive volumes with diameters and heights of 1.8 mm. The millimetric sensitive volumes operated independently and were sandwiched between two layers of A-150 plastic each with a thickness of 2.5 mm. Designed to be used for dosimetry in high intensity radiation fields as well as in nanodosimetry, the GEM-based TEPC was

exposed to a 14 MeV monoenergetic neutron beam and a californium (^{252}Cf) source. The measured spectra were found in excellent agreement with the microdosimetric measurements by traditional wire-based TEPC.

In successive studies, Dubeau et al. tried a microstrip detector [47] and a GEM detector [50], respectively. The first design consists of a gas region which configures wall-less sensitive volumes delimited at the top by a layer of A-150 plastic as the drift electrode and at the bottom by alternating anode and cathode of fine metallic strips lithographically printed on a substrate. Similar to the wire-based TEPC, electrons from ion pair creation drift to the anodes and the electron multiplication occurs in the vicinity of the anodes. The limitations encountered with the use of a microstrip detector such as the low yield of usable printed substrates and radiation damage due to frequent microdischarges at the anode and cathode strips were solved in their second study by inserting a GEM above the readout plane. Employment of a GEM in the detector structure decouples the multiplying element and the readout board and gives more flexibility in the design of the readout anode. Designed to be used as a personal neutron dosemeter, the H*(10) response of this detector was shown to be improved for low energy reactor-like fields compared to that of a conventional TEPC and its sensitivity was about 50% of the sensitivity found for 5 inch conventional spherical TEPC [51].

To the same end, in a search for a modern TEPC, our group developed a prototype microdosimetric detector based on the THick Gas Electron Multiplier (THGEM) concept [52–54]. This device utilizes a single cylindrical TEPC with equal height and diameter of 5 mm coupled to a THGEM. When compared with the standard GEMs, THGEMs are approximately ten times larger in diameter and insulator thickness and offer similar multiplication performance with an inexpensive and more convenient fabrication process. While Byun et al. [52] studied the variation of the electric field and avalanche gain for various combinations of insulator thickness, hole diameter and THGEM bias voltage, preliminary tests and microdosimetric measurements

were performed by Orchard et al. [54] for different THGEM thicknesses in a mixed neutron-gamma radiation field generated by a tandem particle accelerator at McMaster University. The results were promising and the acquired spectra followed the expected distributions. However, to date, there have been no activities dedicated to monitoring weak neutron fields using these new detectors. Although Wang et al. developed a GEM-based TEPC for neutron protection dosimetry [55], it is hardly feasible for weak field dosimetry since the sensitive volume consists of a single element and is relatively small.

Founded on the previous studies of the microdosimetric and THGEM detector research group, the main goal of this work is to design and develop a multi-element THGEM-based microdosimetric detector to enhance neutron detection efficiency. To simplify the detector structure and avoid the difficulties of the traditional methods in the construction of a multi-element TEPC, the central wire anode is replaced by a THGEM as the multiplying element. The application of a THGEM in the design of a microdosimetric detector makes it possible to stack multiple layers of the THGEM-based TEPCs together as one single detector to increase counting efficiency for measuring weak neutron radiation fields. Continuing on an extensive Geant4 simulation study presented in Chapter 3, a prototype detector has been successfully constructed to demonstrate the feasibility of a THGEM-based multi-element TEPC with a multi-layer structure and shed light on the likely path toward a modern TEPC with desired neutron detection efficiency.

1.2 Thesis Outline

Chapter 2 deals with an introduction to experimental microdosimetry, lineal energy concept and distribution as well as some basic principles of the proportional counter as the main device used in microdosimetry. The method of simulating microscopic tissue volumes and the way in which the microdosimetric spectra are usually represented

are described along with the specific features of the lineal energy spectrum in mixed neutron-gamma radiation fields. In addition, the TEPC calibration method used in this study is explained. To provide technical information for the design and construction of a new microdosimeter, a typical structure and the principles of operation of a THGEM-based TEPC are described. Finally, the fundamentals of neutron radiation interactions in tissue are briefly discussed.

A critical issue encountered in designing a multi-element detector is how to compromise the two conflicting requirements: enhancing detection efficiency versus simplifying detector structure for easy fabrication. To answer this question, Monte Carlo simulations were systematically carried out for various multi-element designs and the results are presented in Chapter 3. Using the Geant4 code, the microdosimetric responses were simulated for mono-energetic neutron beams and efficiencies in terms of absorbed dose and dose equivalent were compared with a conventional single cavity detector.

Based on the Geant4 simulation study results, a prototype Thick Gas Electron Multiplier (THGEM) based multi-element Tissue Equivalent Proportional Counter (TEPC) has been designed and constructed. Different components and the technical considerations of the detector are described in Chapter 4. Moreover, the signal stability and preliminary performance tests of the THGEMs carried out using an internal alpha source are presented.

To evaluate the performance of the prototype detector, the fundamental functioning tests of the detector were performed by employing the accelerator-based neutron source facility at the McMaster Accelerator Laboratory. The purpose of the initial tests was to observed the expected features of the event size distributions for a given neutron radiation field, measure the dose rate at a given distance from the neutron source and compare the outcome with the measurement result obtained with a standard

TEPC and finally estimate the detection efficiency of the prototype detector. The microdosimetric responses of the detector are discussed in Chapter 5 explicitly. The results are verified using the 0.5 and 2 inch commercial TEPCs.

Chapter 6 summarizes the steps taken to develop the THGEMs used in this study, the technical complications encountered in implementation of THGEMs within the prototype detector structure for microdosimetry of neutron beams and proposed and used solutions and outcomes. Production, treatment and conditioning procedures, and different characteristics of the THGEM packages employed are described along with their performance in mixed radiation fields.

Conclusions which can be drawn from this work and proposals for future work related to this study will be discussed in Chapter 7.

Chapter 2

Review: Microdosimetry

2.1 Introduction

The study of energy deposition in cellular and subcellular targets is known as microdosimetry and was first introduced by Rossi and Zaider [56]. As an ionizing radiation beam passes through a living tissue, its energy is deposited through ionization and excitation of atoms and molecules along the track of the particles. The density of energy deposition along particle tracks is related to the quality of the radiation involved. The biological damage induced by the ionizations and excitations is governed by the local pattern of energy deposition in individual cells [16]. Therefore understanding of the energy transfer mechanism and measurement of the radiation quantities in cellular and subcellular dimensions is essential. The fact that radiation types with different patterns of energy distribution have different effects for the same absorbed dose is well known and is quantified by the term relative biological effectiveness (RBE). The field of microdosimetry explains the effects of different radiation types through an analysis of the absorption of ionizing radiation at a scale comparable to the biological cells.
In this chapter the concept of experimental microdosimetry and the definition of lineal energy and its distribution are reviewed. The principles of operation and calibration of the low pressure TEPC for determination of dose and dose equivalent in mixed

neutron-gamma radiation fields are given. For comparison, the basic structure of a THGEM-based TEPC in contrast to the standard TEPC is explained. To understand the concepts of energy deposition in microscopic volumes, the fundamentals of neutron radiation interactions in tissue are briefly discussed.

2.2 Experimental Microdosimetry

Experimental microdosimetry is concerned with measurement and interpretation of single-event energy deposition spectra in microscopic scale using a low pressure tissue equivalent proportional counter, i.e. the most commonly used microdosimetric detector. The TEPC provides a pulse height distribution of amplified signals that are proportional to the individual energy deposition events inside the gas cavity. The pulse height distribution can be calibrated in terms of lineal energy (see subsection 2.2.1) to determine the absorbed dose and dose equivalent rates.

Application of microdosimetric techniques provides simultaneous information on the absorbed dose and dose equivalent rates caused by different components of a radiation field. Therefore, the TEPC-based instruments have been widely used for monitoring complex radiation fields where a mixture of radiation of different types and energy exists [19].

2.2.1 Lineal Energy

As formulated by the International Commission on Radiation Units and Measurements (ICRU) [16], lineal energy y is a principal microdosimetric variable in experimental microdosimetry. It is a stochastic quantity defined to describe micro-scale events (in contrast to the LET which is a macro-scale quantity describing the average property of incident particle). According to ICRU 36, lineal energy is defined as the energy imparted ε by a single event in a volume divided by the volume mean chord length $\bar{l}$

and is presented in unit of keV/μm:

$$y = \frac{\varepsilon}{\bar{l}} \tag{2.1}$$

The mean chord length in a convex volume that results from the random interception of the site by a straight line is equal to 4V/S, where V is the volume and S is the surface area of that site [57].

Since the definition of the lineal energy is restricted to the energy imparted in a single event, as a beam of particles interacts with a given volume, it can create a very wide range of energy imparted per event that generates a broad spectrum of lineal energy. The normalized distribution of the number of events is denoted as the frequency distribution of the lineal energy $f(y)$.

The dose distribution $d(y)$ determines the fraction of absorbed dose that is associated with certain values of y and is defined as the normalized distribution of the product $yf(y)$. This relationship indicates that the higher lineal energy deposit a higher dose. The relationship between $f(y)$ and $d(y)$ is given by

$$d(y) = \frac{yf(y)}{\overline{y}_F} \tag{2.2}$$

Where $\overline{y}_F$ is the frequency mean lineal energy and is given by

$$\overline{y}_F = \int_0^\infty y\ f(y)\ dy \tag{2.3}$$

However, for the event size distributions presented in this study, simply the number of events distribution denoted as N(y) is used and the yN(y) distribution is frequently referred as the lineal energy distribution. The acquisition method and derivation of the dose distribution from raw data is explained briefly in the following.

2.3 Tissue Equivalent Proportional Counters

A proportional counter is a gaseous detector which provides a distribution of amplified signals, proportional to the amount of energy released by individual ionization events within the gas. The low-pressure proportional counter, known as Rossi counter [17], was developed in the early 1950s to measure microdosimetric quantities at the site size of 1μm. To model the energy deposited in volumes similar to biological cells, tissue equivalent materials are employed as the detector walls and filling gas. Capable of providing both spectrometric and dosimetric information, TEPCs are extensively used in experimental microdosimetry to determine quality factors and hence the dose equivalent [19].

The traditional TEPC generally consists of a central wire anode surrounded by a spherical gas cavity in a conducting tissue equivalent A-150 plastic [58] of a specified thickness which provides a charged equilibrium condition for protons with energy range up to 20 MeV. The A-150 plastic acts as the detector cathode. In some designs, the anode is bounded by a helix to provide a uniform electric field along the anode. The entire detector assembly is encased in an aluminum chamber which provides electrostatic shielding and serves as a vacuum container. A schematic view of a typical wire-based TEPC is shown in Figure 2.1. As the ionizing radiations interact with the counter wall, secondary charged particles are created. When a secondary charged particle passes through the gaseous sensitive volume, ion pairs are produced along its track. The produced electrons drift toward the anode wire and are multiplied through the Townsend avalanche process with the help of the strong electric field in the vicinity of the anode wire. This phenomenon is called gas multiplication and is a unique characteristic of the proportional counters. In this process, drift electrons gain sufficient energy near the anode to initiate secondary ionizations that are proportional to the amount of primary ionization through the collisions with gas molecules. Finally, the electrons are collected at the anode. Proportional counters are operated in the pulse mode and the output signal is fed to a low noise charge sensitive preamplifier.

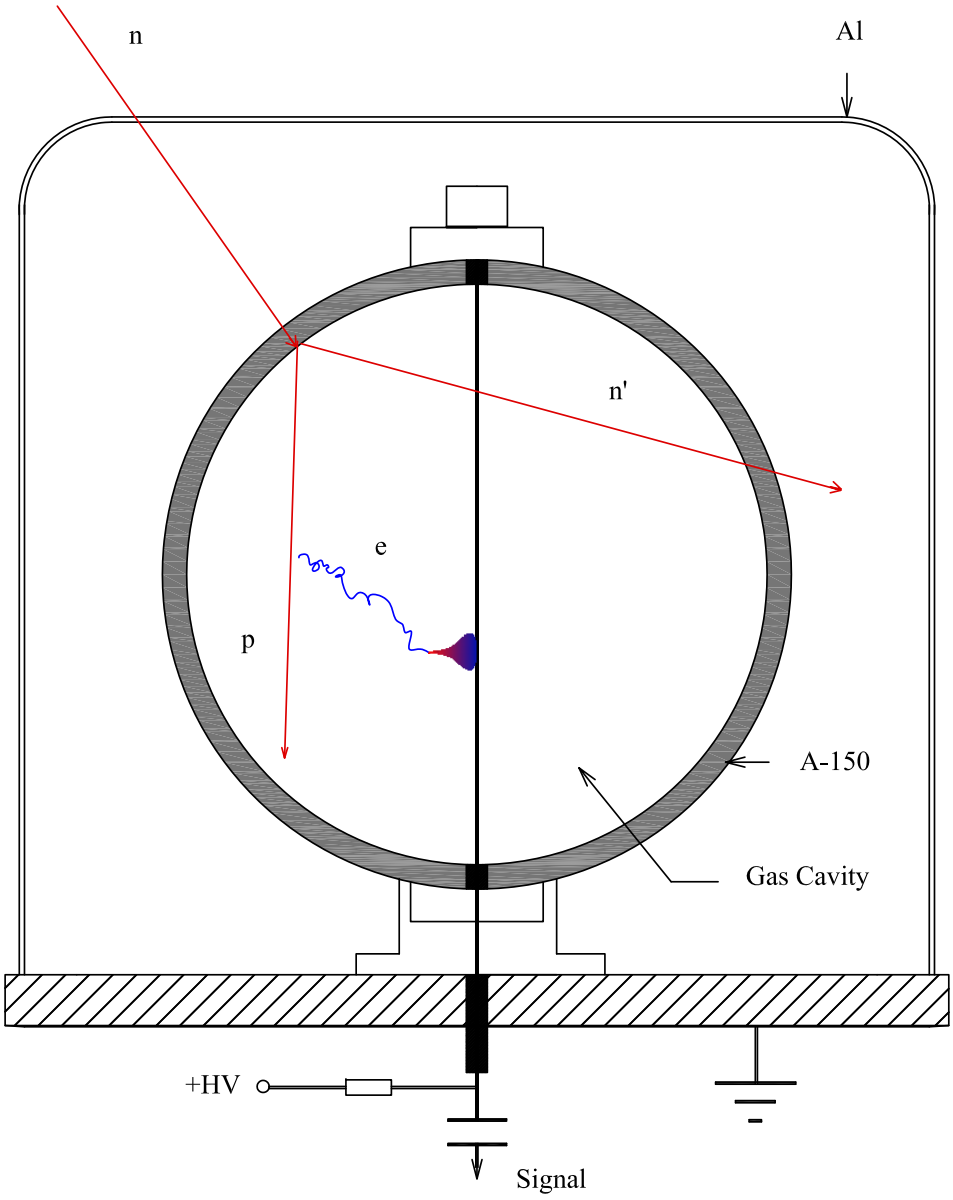

Figure 2.1: A schematic view of a typical wire-based TEPC. The figure is drawn based on a general description given for a conventional TEPC.

2.3.1 Simulation of a Microdosimetric Volume

To simulate a small tissue volume using a larger gas volume, the energy loss of the charged particles has to be identical in both tissue and gas volumes for equivalent trajectories. For a spherical tissue volume of density ρ_t and mass stopping power $(dE/\rho dx)_t$ and a gas volume with parameters ρ_g, $(dE/\rho dx)_g$, the required condition of equivalent energy loss is [16]

$$\Delta E_t = (dE/\rho dx)_t \ \rho_t \ \Delta x_t = (dE/\rho dx)_g \ \rho_g \ \Delta x_g = \Delta E_g \tag{2.4}$$

where ΔE_t and ΔE_g are the mean energy losses from the charged particle in tissue and gas respectively; Δx_t and Δx_g are the path lengths across the tissue and gas volumes. Given a gas with an identical atomic composition to that of tissue, the mass stopping powers of tissue and gas are the same which leads to

$$\rho_t \ \Delta x_t = \rho_g \ \Delta x_g \tag{2.5}$$

This implies that to simulate the energy deposition in a microscopic tissue volume, the product of the gas density and gas cavity diameter should be equal to that of tissue volume. The size of the detector volume is known. Therefore, for a given size of the tissue volume with a known density the required gas density could simply be achieved by adjusting the gas pressure using the ideal gas law

$$P_g = \rho_g \ \frac{RT}{M} \tag{2.6}$$

where R is the ideal gas constant, T is the temperature and M is the molecular mass of the gas. By substituting ρ_g from Equation 2.5, it can be concluded that the gas pressure of the counter is inversely proportional to the diameter of the sensitive volume. Given that RT/M is a constant for the TE gas at the standard laboratory temperature (i.e. 20 °C), pressures corresponding to various simulated sizes are calculated using

the following equation

$$P_g = \rho_g \frac{P_0}{\rho_0} \tag{2.7}$$

where P_g is the required pressure to simulate the desired tissue volume and P_0 is the standard pressure. For a propane based tissue equivalent gas ρ_0 is equal to 1.798 kg/m^3 at 20 °C and the standard pressure of 100 kPa (750.1 torr). The simulated site size is one of the parameters which has influence on the shape of the microdosimetric spectra. The site diameter of 2 μm of the unit density tissue has been most frequently used for a variety of TEPC applications [1, 18, 20–22, 30] and therefore was chosen in this study. Therefore, to simulate a 2 μm unit density tissue with for example a 2 inch commercial TEPC (with diameter of 5.08 cm), the gas pressure should be reduced to

$$P_g = \frac{1gr/cm^3 \times 2\mu m}{5.08cm} \cdot \frac{750.1torr}{1.798kg/m^3} = 16.4\ torr \tag{2.8}$$

2.3.2 Presentation of Microdosimetric Distributions

In practice the range of event sizes would cover several orders of magnitude. As a consequence a wide lineal energy range is observed in a typical microdosimetric spectrum (from 0.1 keV/μm to several hundred keV/μm) [19]. Therefore, the representation of the microdosimetric spectra is conventionally displayed as a semi-log plot with the ordinate multiplied by y such that the area under the curve between two values of y is proportional to the fraction of events or dose in that region. By definition, the frequency distribution $f(y)$ and dose distribution $d(y)$ are normalized to unity. When transforming the linear representation of lineal energy to a semi-log plot, this normalization should remain unchanged. For example for dose distribution, we can write

$$\int_0^\infty d(y)\ dy = \int_0^\infty y\ d(y)\ d(\ln y) = \ln 10 \int_0^\infty y\ d(y)\ d(\log y) \tag{2.9}$$

In a case that the logarithmic scale of y is subdivided into B increments per decade

$$\ln 10 \int_0^\infty y\ d(y)\ d(\log y) \simeq \frac{\ln 10}{B}\ \sum_{i=0}^{\infty}\ y_i\ d(y_i) \tag{2.10}$$

where $\mathrm{d}(\log y) \simeq \Delta \log y = 1/B$. Similar equations could be applied for $f(y)$.

Figure 2.2a is an example of the distribution of pulse heights in a mixed neutron-gamma radiation field. The raw data are recorded using a 0.5 inch commercial TEPC exposed to a radiation field generated by accelerated protons of 2.3 MeV acting on a Li target with a current of 50 μA. From the figure, it is evident that the linear representation doesn't reveal details of the distribution of events. Figure 2.2b shows the yN(y) distribution of Figure 2.2a in a semi-log plot in which the lineal energy y is computed for each event size and redistributed into equal logarithmic bins with a resolution of 60 bins per decade, that gives a detailed feature of the distribution while keeping sufficient smoothing of data.

The representation of the microdosimetric data in a semi-log plot, as described, is mainly done to provide a more convenient method in visual interpretation of the event size spectrum. It facilitates the evaluation of the contribution of the various types of secondary charged particles to the total dose. In other words, the spectrometric ability of TEPCs makes it possible to distinguish events from the various particle types. This is a unique advantage of proportional counters for microdosimetric measurement in a mixed neutron-gamma radiation field [19]. This feature may be seen from Figure 2.2b. The lineal energy distribution in this case has two components: below 10 keV/μm, and above 10 keV/μm. Low energy region is mainly created by secondary electron events caused by gamma ray interactions. The second component is corresponding to recoil protons generated mainly by the elastic interaction of neutrons with hydrogen nuclei as the predominant interaction mode of fast neutrons. Since the tissue equivalent materials have relatively high hydrogen content, a large portion of the neutron energy can be transferred to the proton of a hydrogen atom which results in a "proton peak" in lineal energy spectrum. The sharp drop on the upper end of the proton peak is

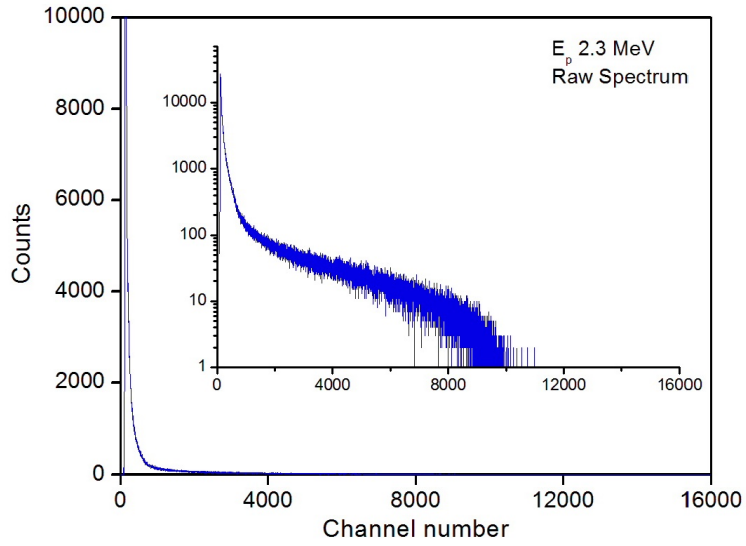

(a)

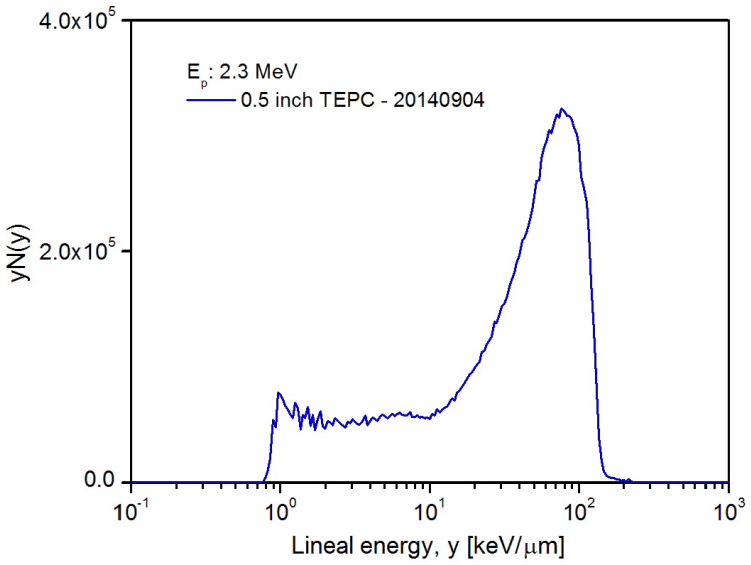

(b)

Figure 2.2: a) Distribution of pulse heights in a mixed neutron-gamma field. The raw data were recorded using the 0.5 inch commercial TEPC for the proton energy of 2.3 MeV at 50 µA current. b) The corresponding yN(y) distribution in a semi-log plot with the resolution of 60 bins per decade. Data were collected in tandetron accelarator lab in September 2014.

known as the proton edge. For a recoil proton crossing the sensitive volume along the diameter, the departed energy by the proton depends on the range of protons. The maximum value of the imparted energy will be obtained when the range of the recoil proton is equal to the sensitive volume diameter. For a 2 μm simulated site size the lineal energy value of the proton edge is 136 keV/μm [19].

2.3.3 Dose and Dose Equivalent Calculations

Given that the energy imparted in a single event in units of keV is given by $\varepsilon = y\bar{l}$, the total energy deposited in the gas cavity in units of Joules is found by

$$total\ deposited\ enery = (1.6 \times 10^{-16} J/keV) \sum_i (y_i \bar{l}_m)\ N(y_i)\ [J] \tag{2.11}$$

Where y_i is the lineal energy (keV/μm), $\bar{l}_m$ the mean chord length for the micrometric soft tissue volume (μm) and $y_i\bar{l}_m$ the deposited energy (keV) at the i^{th} logarithmic bin. The absorbed dose D is defined as the quotient of the total energy imparted by ionizing radiation to matter of mass m, of a given volume. Then, for a gaseous cavity of volume V_g [cm^3] and gas density ρ_g [g/cm^3], the absorbed dose can be written as

$$D = \frac{total\ deposited\ enery}{gas\ mass} = \frac{(1.6 \times 10^{-16} J/keV) \sum_i (y_i \bar{l}_m)\ N(y_i)}{(10^{-3} kg/g)\ \rho_g\ V_g}\ [Gy] \tag{2.12}$$

For a spherical simulated volume of diameter d_m, the mean chord length is $2d_m/3$. After applying the energy loss matching requirement between gas cavity and soft tissue, i.e. $\rho_g d_g(g/cm^2) = \rho_m d_m(g/cm^2)$, one can write

$$D = \frac{(2.037 \times 10^{-9})}{d_g^2} \sum_i\ y_i N(y_i)\ [Gy] \tag{2.13}$$

In which the density of the simulated soft tissue ρ_m is considered 1 g/cm^3. Equation 2.13 implies that the absorbed dose in tissue can be derived by taking the sum over the measured lineal energy spectrum where the geometry of the gas cavity is reflected in

an appropriate constant.

One of the important advantages of TEPC-based instruments in radiation protection is that they provide information on radiation quality in mixed radiation fields. According to ICRP 60, the mean quality factor $\overline{Q}$ can be obtained as

$$\overline{Q} = \frac{\int_0^\infty Q(L)\ d(L)\ dL}{\int_0^\infty d(L)\ dL} \tag{2.14}$$

where Q(L) is the quality factor and d(L) is the dose distribution as a function of linear energy transfer (LET) L. By approximating $y \simeq L$, the mean quality factor can be evaluated from the measured lineal energy distribution as following

$$\overline{Q} = \frac{\int_0^\infty Q(y)\ d(y)\ dy}{\int_0^\infty d(y)\ dy} \simeq \frac{\sum_i\ Q(y_i)\ y_i\ d(y_i)}{\sum_i\ y_i\ d(y_i)} \tag{2.15}$$

The functional dependence of the quality factor on the linear energy transfer is specified by ICRP 60 [2] as

$$Q(L) = \begin{cases} 1, & L < 10\ keV/\mu m \\ 0.32L - 2.2, & 10 < L < 100\ keV/\mu m \\ 300/\sqrt{L}, & L > 100\ keV/\mu m \end{cases} \tag{2.16}$$

The above mathematical expression is plotted in Figure 2.3 and is used in this work to calculate the mean quality factor from simulation data (see Chapter 3).

Having obtained the mean quality factor, the dose equivalent can be calculated as the product of the absorbed dose delivered to the sensitive volume of the TEPC and the mean quality factor of secondary charged particles that traversed the volume. This is stated mathematically as

$$H = D \times \overline{Q} \tag{2.17}$$

The quality factor is a dimensionless quantity that weights the absorbed dose according to biological effect. While the absorbed dose D is expressed in gray (Gy), the SI unit

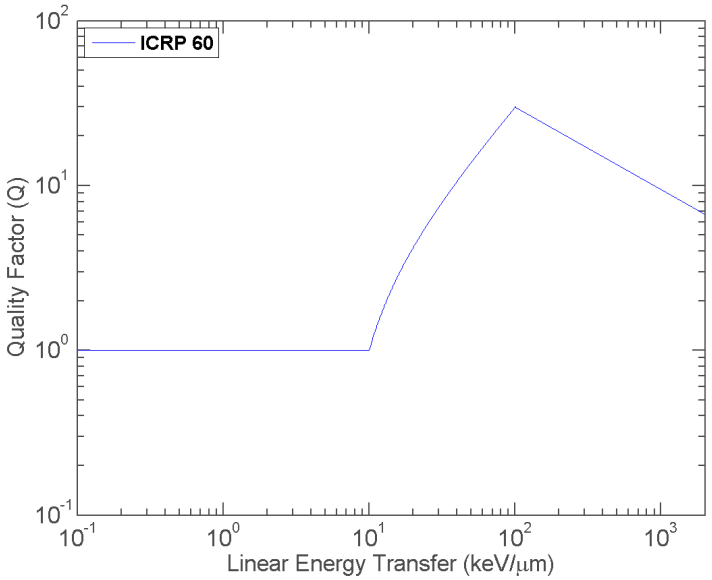

Figure 2.3: Quality factor Q(y), according to ICRP 60 [2].

for the dose equivalent H is sievert (Sv), i.e. 1 J kg^{-1}.

2.3.3.1 Neutron-photon Separation

As mentioned earlier, the TEPC allows identifying the contribution of low and high LET components of a mixed neutron-gamma radiation within a single measurement. To this end different approaches are described by Gerdung et al [59]. The microdosimetric method is based on the fact that secondary particles from interactions of photons (electrons) and neutrons (protons and heavier particles) with the sensitive volume gas content and wall contribute to different parts of the lineal energy spectrum. However, for the lineal energy values between 1 and 10 keV/μm, the two contributions overlap [60]. The fitting of a previously stored microdosimetric spectrum of events due to photon interactions in the counter can be used to unfold photon and neutron events. The absorbed dose of each radiation component can be determined by integrating each part of the dose spectrum and multiplying with the appropriate constant as described above.

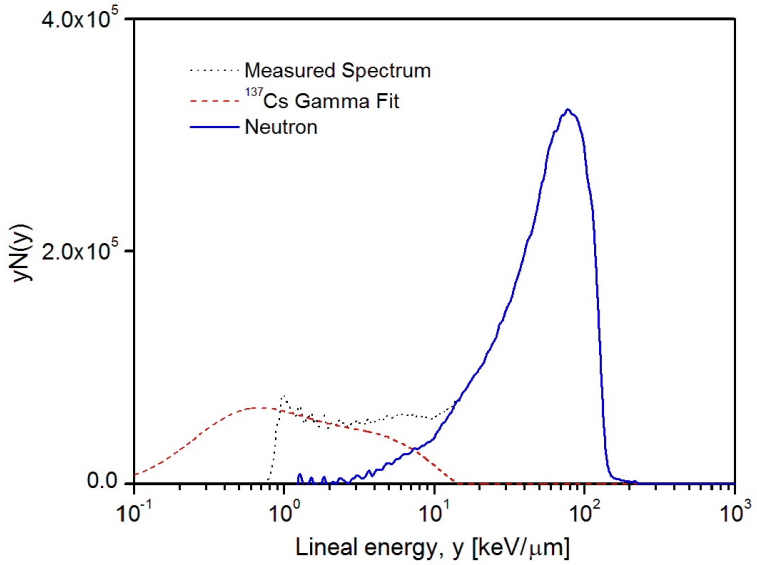

Figure 2.4: Illustration of neutron-gamma discrimination using a commercial TEPC.

To choose an appropriate photon event size spectrum, the knowledge of the photon energy distribution or at least the information on the average photon energy is required [59]. For example, in a mixed field with a high average photon energy, e.g. a field which is dominated by 2.2 MeV photons from neutron capture in hydrogen, a pure ^{60}Co or ^{24}Na spectrum can be used with overall uncertainty on the photon dose fraction of less than 13% [59, 60].

For the radiation facility described in this work (see subsection 5.2.1), the contaminating photons mostly come from two interaction modes: photons of 478 keV emitted from the first excited state of the Li target, ^{7}Li(p, p$'\gamma$), and 2.2 MeV capture gamma rays from the collimator and shielding, ^{1}H(n, γ), where the 478 keV mode is dominant in the spectrum [61]. Also, it is expected that most of these photons would be degraded in energy by scattering before reaching the detector. For this reason ^{137}Cs is considered to be an appropriate choice for the gamma component event size spectrum [61].

Figure 2.4 is an illustration of neutron-photon discrimination using a ^{137}Cs gamma fit for a lineal energy distribution obtained with the commercial 0.5 inch TEPC.

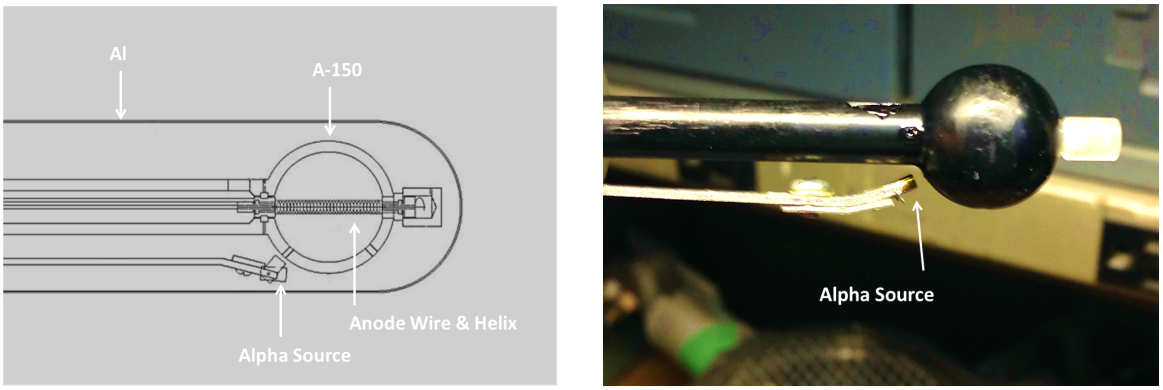

(a) (b)

Figure 2.5: a) A cross-sectional view of the 0.5 TEPC and b) a photograph showing the alpha source position inside the aluminum casing.

2.3.4 Calibration of a TEPC

The calibration of a proportional counter is aimed at converting the collected pulse height spectrum into the lineal energy spectrum. The conversion can be achieved using a collimated beam of mono-energetic alpha particles, the recoil proton edge of fast neutrons or soft X-rays [62–64].

Calibration by alpha particles requires a built in alpha source. In this study, for the commercial 0.5 inch TEPC the conversion is achieved by using a built-in collimated ^{244}Cm source emitting alpha particles with a mean energy of 5.78 MeV. The details of the detector structure after removing the aluminum cap is illustrated in Figure 2.5. As shown, the source is located inside the aluminum casing of the counter in vicinity of the A-150 sphere and is mounted in such a way that in one orientation of the counter the source pivots on a very thin wire into position and alpha particles can enter the sensitive volume through a small aperture in the counter wall. Alpha particles emitted from the source are directed to pass along the counter sensitive volume diameter. As the alpha particles cross the sensitive volume, the electrons created by ionization of the filling gas drift toward the central wire and are multiplied by the gas gain of the counter. The resulting charges collected on the anode produce voltage pulses that are fed into a preamplifier and then are stored in the appropriate channel of a pulse height

analyzer after electronic amplification. The pulse height spectrum exhibits a peak. By using a Gaussian function the centroid channel of the peak, corresponding to the average energy lost by the alpha particle, can be calculated. Figure 2.6 represents the pulse height distribution produced by alpha particles from the calibration source.
The average amount of energy deposited by alpha particles crossing the cavity can be derived from range tables [65] and the path length traversed by the alpha particles. For a simulated cite size of 2 μm, alpha particles deposit 170 keV in tissue-equivalent gas, corresponding to a lineal energy of 127 keV/μm. Then, for any event producing a signal with pulse height h_i, the lineal energy y_i can be determined by

$$y_i = \frac{h_i}{h_{alpha}} \times 127 \; [keV/\mu m] \tag{2.18}$$

To convert the channel numbers of acquired spectra to pulse amplitudes, a calibration curve was generated using a pulse generator illustrated in Figure 2.7.
It should be noted that the conversion of ionization yield into energy imparted requires a knowledge of the W-value, the average energy required to produce an ion pair, that differs depending on particle type and energy. However, the additional uncertainty introduced because of the difference between the W-values of the alpha particles used for the counter calibration and the protons generated by the neutron beam is relatively small [59, 60]. So no correction factor for W-value has been applied in this study.
To calibrate pulse height spectra measured by a 2 inch TEPC and the prototype multi-element THGEM detector, that don't have a built-in calibration source, the lineal energy value of the recoil proton peak of the 0.5 inch commercial TEPC was used so that the proton peak position of a collected spectrum matches that of a 0.5 inch TEPC collected in an identical condition.

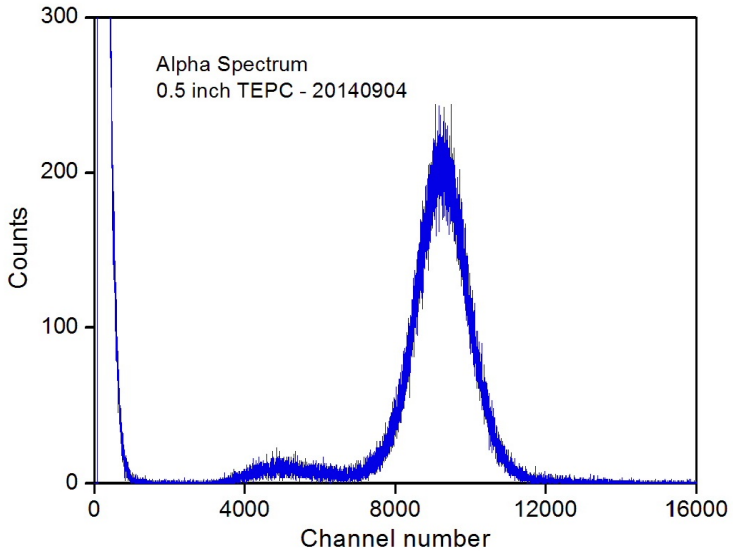

Figure 2.6: Pulse height distribution of alpha particles emitted by an internal calibration source of 0.5 inch TEPC (collected in September 2014).

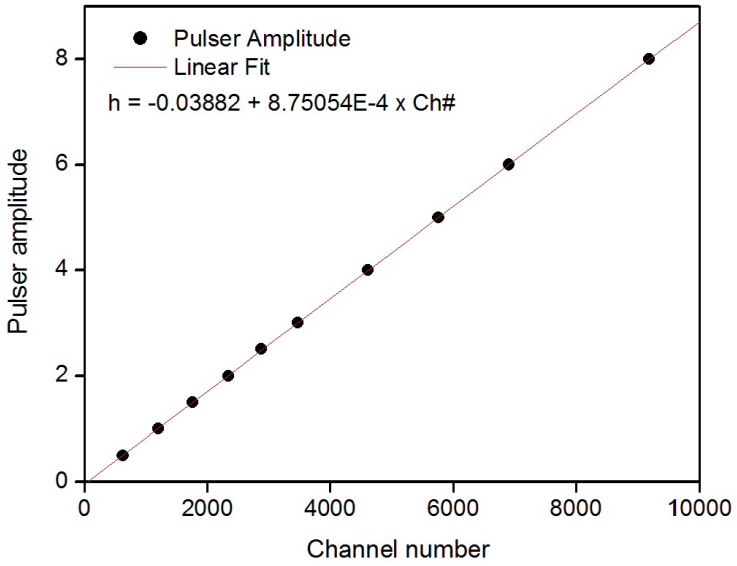

Figure 2.7: The curve generated to convert channel numbers of the collected pulse height spectra to the corresponding pulse amplitudes (collected in September 2014).

2.3.5 Detector Response Metrics

In mixed neutron-gamma radiation fields the operational quantity for area monitoring is the ambient dose equivalent $H^*(10)$, that is defined as the dose equivalent in a 30 cm tissue-equivalent sphere at a depth of 10 mm [1].

The dose equivalent response R_H (also known as the relative dose equivalent response) of a counter is defined as the ratio of the measured dose equivalent to the true $H^*(10)$ as

$$R_H = \frac{H_{Measured}}{H^*(10)} \tag{2.19}$$

In radiation protection applications, a TEPC with dose equivalent response close to unity is desired for the whole energy range of importance.

TEPC-based instruments give excellent dose equivalent response for neutrons above a few hundred keV. However, for the neutron energy range below 100 keV down to about thermal energy, the device response deteriorates [66]. This is partly due to the fact that the range of the recoil protons created by the neutrons becomes small compared to the simulated diameter by the TEPC. So the approximation of LET by lineal energy is no longer valid and both quality factors and measured dose equivalent tend to be underestimated [19, 66] (also see subsection 3.4.2). However, given the fact that the point of reference of $H^*(10)$ is at depth of at least 1 cm in tissue, the value of the ambient dose equivalent is strongly influenced by the neutron scattering properties of the ICRU sphere. Therfore, the underestimation in measured dose equivalent by the Rossi counter predominantly relates to the geometrical difference between the ICRU sphere and the Rossi detector [6, 66].

The counter wall thickness, material composition of the filling gas and wall, and the simulated site size are among the variables that can be optimized in order to increase the dose equivalent response of a TEPC design in low energy neutron fields [39, 66]. The response of a TEPC to neutrons has been systematically investigated for varying wall thicknesses in ref. [38] . Their counter consists of a spherical sensitive volume

with diameter of 7 cm and 1 mm A-150 plastic wall covered by a layer of polyethylene. As shown in Figure 2.8a, in comparison to a 2 inch Rossi counter, the dose equivalent response of the detector for the neutron energy range from thermal to 20 MeV can be improved by adding a polyethylene cap to the TEPC with the optimum thickness of 1.5 cm. They also showed that the dose equivalent response of the optimum design is a better match for the $H^*(10)$ for the smaller simulated diameters [6, 38]. This is illustrated in Figure 2.8b.

As the primary metrics in evaluating detector response characteristics, the quality factor and dose equivalent responses of the THGEM-based multi-element TEPC designs presented in this study are calculated and discussed explicitly in subsection 3.4.2.

In addition, as a principal design requirement of a TEPC for monitoring weak neutron radiation fields the detector must have an adequate detection efficiency (or sensitivity) while be of relatively small physical dimension to allow for portability. For a dose equivalent meter, the detection efficiency is usually defined as the total count per unit dose equivalent and is directly proportional to its surface area [43].

In the course of the current study, the emphasis is put on the detection efficiency enhancement of a TEPC-based instrument that can provide a similar dose equivalent response as the standard TEPCs.

2.4 THGEM-based TEPC: Principles of Operation

The basic concept of the THGEM consists of a compact array of micro holes in a copper coated substrate. The holes are obtained by drilling using standard printed circuit board manufacturing techniques. That allows fabrication of THGEMs with large areas at reduced costs compared to the standard GEM. Due to their rigidity, THGEMs don't need additional mechanical support, making them very easy to implement in a gaseous detector. The geometrical parameters of THGEMs, PCB thickness and holes diameter and pitch, cover wide ranges typically from a hundred micron to about 1 mm.

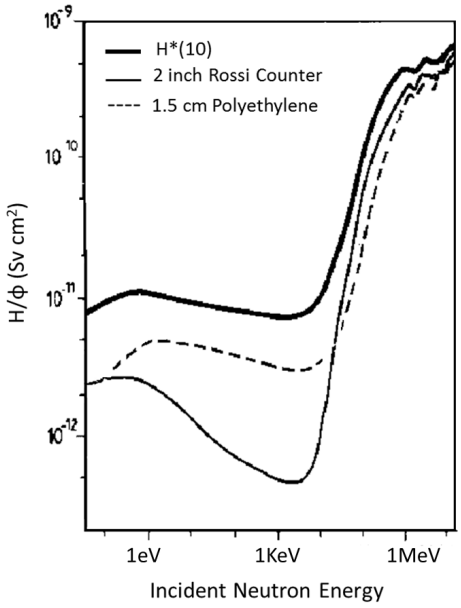

(a)

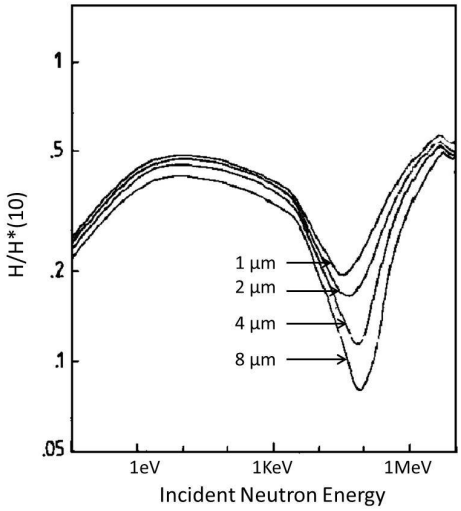

(b)

Figure 2.8: a) Calculated dose equivalent per unit incident fluence as a function of incident neutron energy for 2 inch Rossi counter and the optimum design. b) Dose equivalent response of the optimized design calculated for several simulated diameters. The counter consists of a spherical sensitive volume with diameter of 7 cm and 1 mm A-150 plastic wall covered by a 1.5 cm thick layer of polyethylene [38].

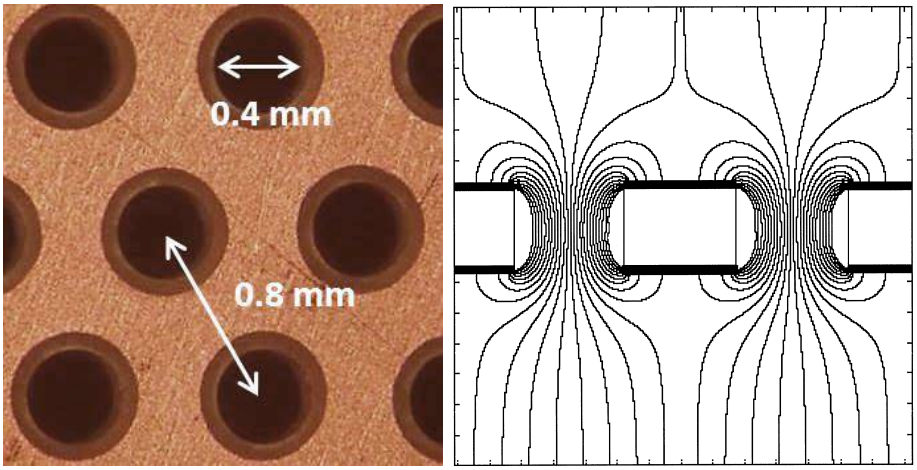

(a) (b)

Figure 2.9: a) A microscopic photograph of a typical THGEM electrode. The one shown has a hole diameter of 0.4 mm with an etched rim around holes that are spaced by 0.8 mm in a hexagonal array [67]. b) Electric field profile of a biased GEM [68].

Extensive studies on THGEMs have been performed to characterize and evaluate their performance and some of them can be found in ref. [67, 69–71]. A close view of a typical THGEM is shown in Figure 2.9a. The THGEM operation principle is similar to that of a standard GEM. By application of a high potential difference across the THGEM top and bottom layers, a strong electric field is established within the holes as schematically illustrated in Figure 2.9b. A quantitative illustration of the electric field strength at the center of a THGEM hole along the axial direction is presented in Figure 2.10a for three different insulator thicknesses with hole diameter of 0.6 mm and THGEM bias of 800 V. Electrons released by ionization in the upper gas region (sensitive volume) drift into the THGEM holes, where they multiply in an avalanche process and are directed to the lower gas region (see Figure 2.10b). Depending on the size and direction of the electric field, a fraction of the resulting avalanche electrons may be drawn to the bottom of the THGEM while the rest can be further transferred to a second THGEM or be collected by a readout board. In this work, measurements were carried out with a single-THGEM detector configuration, as described in Chapter 4.

The aforementioned geometry offers two unique advantages. It should be noted that

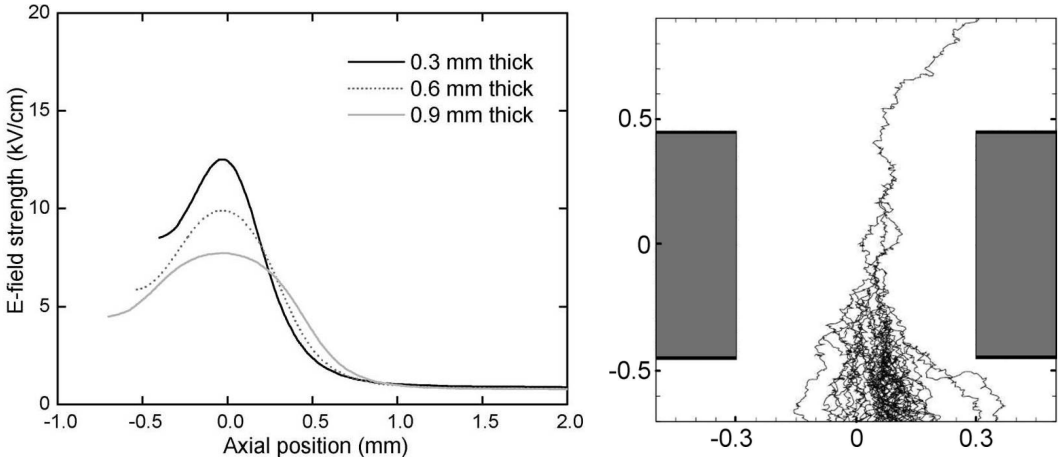

(a) (b)

Figure 2.10: a) An example of calculated electric field values along the hole axis for three different insulator thicknesses for a THGEM bias of 800 V and b) an electron avalanche formation inside a THGEM hole [52].

each avalanche is kept within a hole and is independent from other avalanches. The avalanche confinement within the holes has the advantage of reduced photon-mediated secondary effects [67, 69]. The other advantage is that the multiplication region can be detached from the readout electrode to reduce the risk of spark induced damage frequently seen in gas avalanche micropattern detectors, e.g. microstrip detectors [72]. Within our group, THGEMs have been employed in development of several novel detectors including single and multi-element TEPCs for microdosimetry [52, 54, 73] and a THGEM-based imaging detector whose performance was evaluated using a collimated alpha source and X-ray beam [74]. More recently, a graduate student, Matthew Bernacci, is designing and procuring the necessary components to assemble a THGEM-based detector for efficient tritium detection in CANDU reactors.

For microdosimetry in mixed neutron-gamma radiation fields, a novel configuration of a THGEM-based TEPC was proposed by Byun et al. [52]. The conceptual drawing of the detector is shown in Figure 2.11. The dependence of the electron multiplication gain on the THGEM geometrical parameters was systematically investigated for propane-based tissue equivalent gas using the GARFIELD code [75] to find an optimum configuration

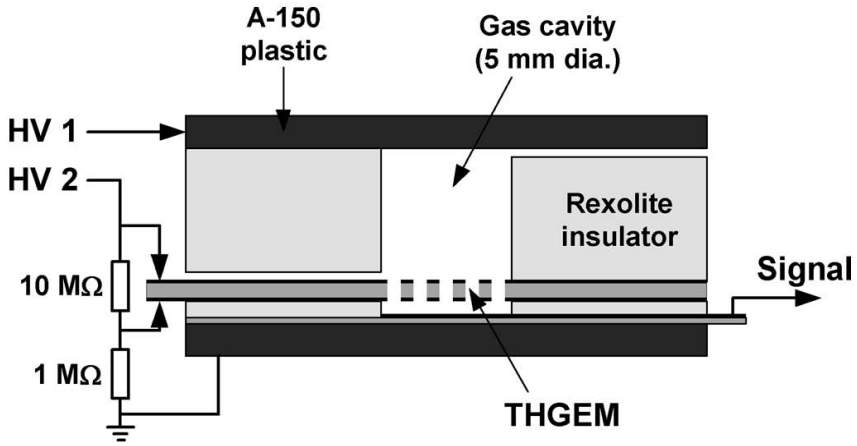

Figure 2.11: Conceptual drawing of the THGEM-based detector proposed by Byun et al. [52].

for the THGEM developments. Orchard et al. [54] developed a prototype detector that incorporates a cylindrical sensitive volume with equal height and diameter of 5 mm. The preliminary experimental tests were promising and acquired spectra showed the expected distributions in neutron-gamma radiation field. Hanu et al. [53] used Geant4 simulation code to evaluate the microdosimetric distributions of the same detector configuration for various neutron energies. The prototype multi-element detector presented in this study is founded on the aforementioned studies and follows similar operation principles.

2.5 Interactions of Neutrons in Tissue

Neutrons carry no charge and hence are not subject to Coulomb's interaction. They can travel appreciable distance in matter without any interaction. Therefore, most neutron detectors are designed based on conversion of the incidental neutron into directly detectable secondary charge particles. When neutrons interact with matter the energy is lost by interaction with the nuclei of the target material. A Neutron can interact with an atomic nucleus through several mechanisms depending on its

energy. However, the ionization in the human body exposed to neutrons is mainly produced by recoil protons, carbon, oxygen or other heavier nuclei and products of nuclear reactions [76]. In hydrogenous matter (e.g. tissue) the main interaction modes of neutrons are

a) Elastic scattering of fast neutrons with the hydrogen, giving rise to a recoil proton.

b) The radiative capture reaction of thermal neutrons or (n, γ) reaction that plays an important role in attenuation of neutrons.

Elastic scattering of neutrons is the most important process for slowing down neutrons. In this process, the total kinetic energy is conserved so that energy lost by the neutron is transferred to the recoiling nucleus. Using the conservation laws of energy and linear momentum, for incoming neutron kinetic energy of E_n the energy transferred to the recoil nucleus E_R is given by

$$E_R = \frac{4A}{(1+A)^2}\ cos^2(\theta)\ E_n \tag{2.20}$$

where A is mass of target nucleus and θ is scattering angle of the recoil nucleus in the laboratory system [8]. It can be concluded from the Equation 2.20 that for a head-on collision ($\theta \cong\ 0$), the energy transfer is most efficient if the colliding particles have the same mass, e.g. a neutron colliding with a hydrogen nucleus. This mechanism is the basis for the conversion of neutrons to directly detectable charged particles in tissue equivalent proportional counters.

Chapter 3

Monte Carlo design study for THGEM-based multi-element microdosimetric detector

3.1 Introduction

To accomplish an enhanced neutron dose response with high detection efficiency, a set of multi-element microdosimetric detectors was designed using a THick Gas Electron Multiplier (THGEM). THGEM generates a strong electric field within micro holes of a sub-millimeter thick insulator, which makes electron multiplication possible without the traditional anode wire electrodes. Owing to the absence of wire electrodes, the newly designed neutron dosemeters offer flexible and convenient fabrication in contrast to the traditional multi-element tissue-equivalent proportional counters.

In order to investigate the dependence of the neutron dosimetric response and detection efficiency on detector design, five designs with a different numbers of gas cavities and an identical outer diameter of about 5 cm were created. For each design, a Monte Carlo simulation was developed using the Geant4 code to calculate the deposited energy spectrum in the gas cavities for mono-energetic neutron beams ranging from

10 keV to 2 MeV.

From the simulation results, the microdosimetric and the absorbed dose responses of each multi-element design were consistent with the responses of the conventional single cavity detector. The quality factor and the dose equivalent responses were subsequently obtained and showed reasonable agreement with the ideal values for neutron energies above 300 keV while underestimating in the lower energy region. The neutron detection efficiency of each design was analyzed in terms of the neutron counts per incident fluence and the counts per dose equivalent. As the number of the multi-element cavities increased, both efficiencies increased greatly. The efficiency of the highest cavity density with 61×9 multi elements was on average 5.6 times higher than that of the single cavity design. The 37×7 design could be chosen as a reasonable compromise between the two conflicting requirements, high efficiency and convenience in fabrication. Given the fact that the surface area of the 37×7 design is comparable to that of a 5 inch standard detector, it offers the same detection efficiency while is as compact as a 2 inch standard TEPC. This chapter presents the Geant4 Monte Carlo simulation results for the proposed THGEM detector designs.

The work presented in this chapter was published in Nuclear Instruments and Methods in Physics Research A [73]. The simulation code development, computing and data analysis work was performed by the author of this thesis under the supervision of Dr. Soo Hyun Byun and with guidance of Dr. Andrei Hanu.

3.2 Conceptual design

To investigate the performance of different THGEM multi-element detectors with regard to dosimetric response and efficiency, five different designs were studied through Monte Carlo simulations. Table 3.1 summarizes the detailed specifications of the five detector designs. For each design, the outer dimension was fixed to a cylindrical volume with 5.5 cm diameter and the number of the gas cavities was gradually increased by

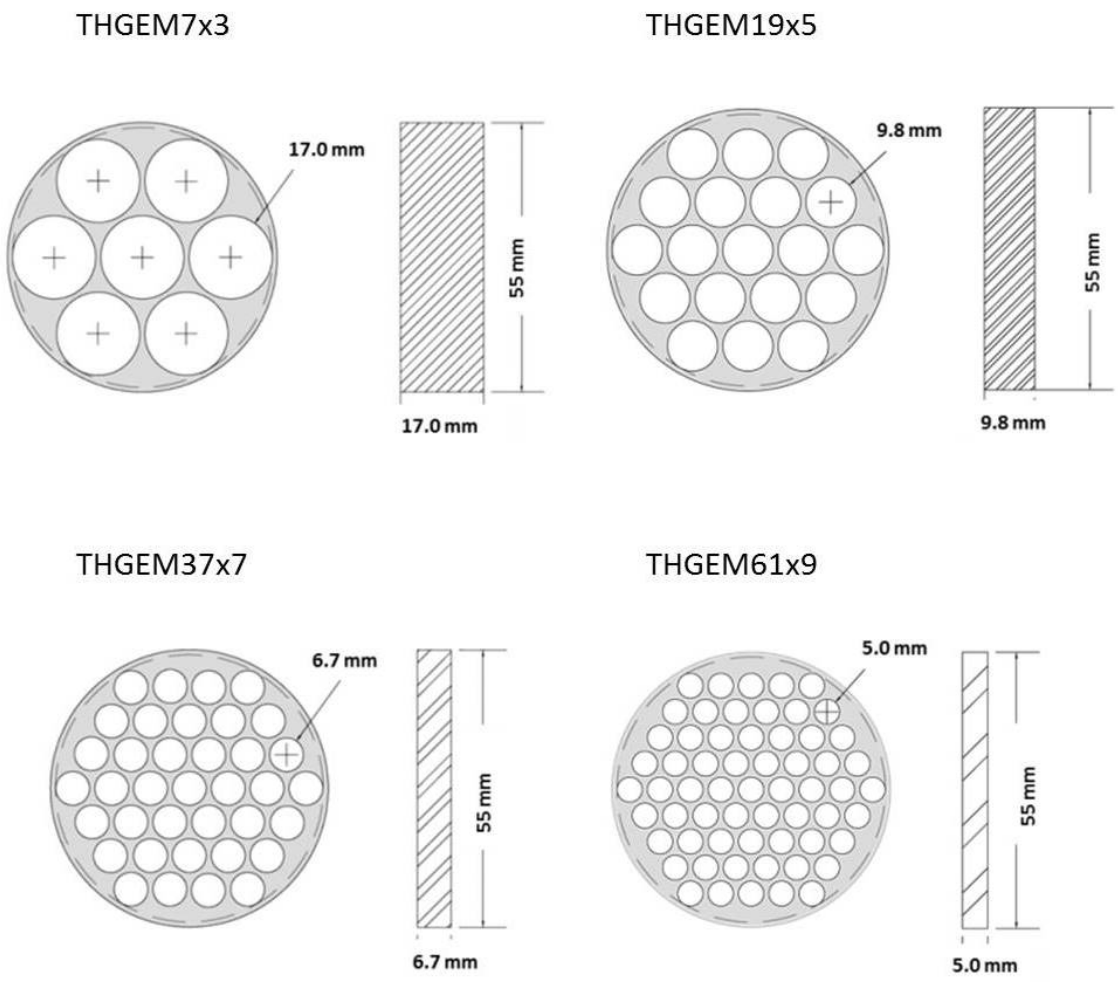

Figure 3.1: A schematic illustration of the top and side views of the designed insulators housing hexagonal patterns of sensitive volumes.

subdividing the entire gas volume into cylindrical sub-elements. This allows for a full investigation of the dependence of the detection efficiency on the multi-element density through simulations. Figure 3.1 is a schematic illustration of the designed insulators housing hexagonal patterns of sensitive volumes.

Table 3.1: Specification of the THGEM multi-element detector designs. The detector configurations are named in such a way that the first number next to the THGEM letter represents the number of subelements in each Rexolite layer and the second one is the total number of Rexolite layers.

	THGEM1×1	THGEM7×3	THGEM19×5	THGEM37×7	THGEM61×9
SV Diameter & Height (cm)	5.30	1.70	0.98	0.67	0.50
Total Number of Sub-Elements	1	21	95	259	549
Total SV Surface Area (cm^2)	132.30	285.85	429.73	549.95	646.45
Mass of Gas (mg)	4.41	9.53	14.32	18.33	21.55
Gas Density (mg/cm^3)	0.04	0.12	0.20	0.30	0.40
Gas Pressure (torr)	15.74	49.08	85.14	124.27	166.87

The simplest design, THGEM1 × 1, has a single gas cavity element with a diameter and length of 5.3 cm (132 cm^2) while the most complicated design, THGEM61×9, consists of 549 cavity elements, which gives the largest surface area (646 cm^2). Figure 3.2a shows a three dimensional view of the THGEM61×9 design and two options for stacking the THGEM and signal pad layers. The structures of the other three designs (7 × 3, 19×5 and 37 × 7) were determined in the same manner with the 61 × 9 design.

As shown in the figure, the multi-element detectors consist of alternating layers of Rexolite insulator (Rexolite 1422, C-LEC Plastics, Inc.) discs, which houses a hexagonal array of cylindrical gas cavity elements with equal height and diameter. Each Rexolite layer is sandwiched between 1mm thick A-150 conducting plastic [58] and a THGEM layer. The charge collection regions are located next to each THGEM layer. The wall thickness between each sub-element was kept at least 1 mm to satisfy the charged particle equilibrium condition, i.e. balance between the incoming and outgoing charged particle energy flows, for neutrons with energies applied in this study.

To keep a consistent microdosimetric response, each detector is filled with propane based tissue equivalent gas [77] at the pressure listed in Table 3.1 to simulate the

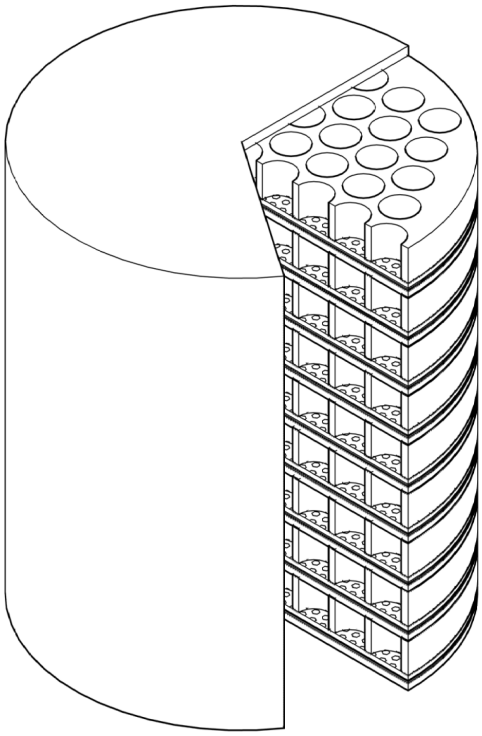

(a)

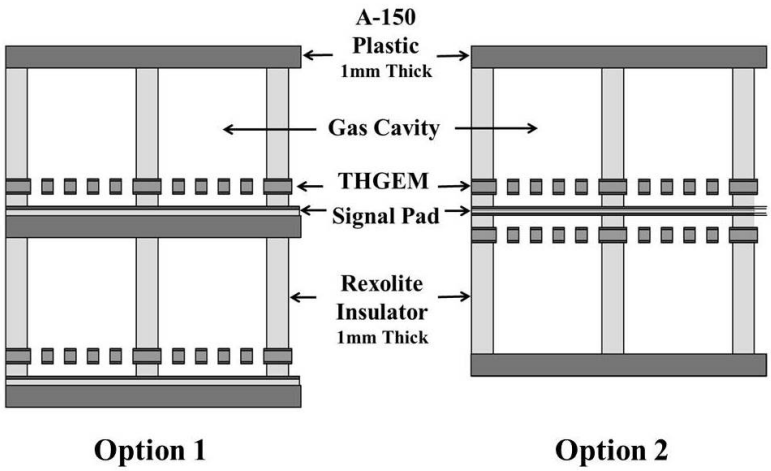

(b)

Figure 3.2: a) 3D view of the THGEM61×9 design and b) details of the assembling option 1 and option 2.

energy loss of charged particles in 2 µm of unit density soft tissue. The site diameter of 2 µm has been most frequently used for a variety of TEPC applications [1,18,20–22,30] and therefore was chosen in this study. The gas pressure of each design is inversely proportional to the diameter of the sensitive volume to keep the energy loss in each design identical.

Figure 3.2b shows two options for stacking constituent materials. In the option 1, the A-150 conducting plastic is positioned on top of each Rexolite layer and the THGEM positioned on the bottom of the Rexolite layer while their positions are mirrored in the option 2. Referring to the angular response of the detector (see subsection 3.4.4) and a Monte Carlo simulation study by Hanu [53] that uses a single 5×5 mm cavity, it is expected that option 2 will have a slightly lower efficiency but a better angular response over option 1. As the main focus of this study is to investigate the dependence of the microdosimetric response on the multi-element design, only option 1 was used in Monte Carlo simulations.

3.3 Monte Carlo simulation

The microdosimetric response of a single element (5 mm by 5 mm) THGEM detector was simulated using Geant4 by Hanu [53] and the simulated microdosimetric spectra were compared with reported experimental results for a standard 0.5 inch TEPC. The simulation results showed reasonable agreements with experimental data over a wide range of neutron energy. In the present study, the simulation is extended to the multi-element detector designs.

The Monte Carlo simulations were performed using version 9.5 of the Geant4 toolkit on a Linux based parallel computing cluster, available from Sharcnet [78]. Typical computational times of 3-4 days produced a statistical uncertainty of 0.1% in the deposited energy. As used in these simulations, the physics list includes models describing elastic and inelastic neutron scattering, neutron induced fission, and neutron

capture. For charged particles, such as protons, alpha particles and other heavy ions, the ionization process is described by the continuous slowing down approximation using data from ICRU Report 49 [79]. Geant4 provides a range cut-off parameter. For each material and particle, the range cut-off is converted to a threshold energy below which the production of secondary particles stops and the remaining energy is locally deposited. In all simulations, the default cut range of 1 mm was used for all materials. Given the mean value of the THGEM electron multiplication factor is constant and the total charge collected after multiplication is proportional to the original charge produced by a detection event, the detector response aimed in the present study can be fully understood from the energy deposited in the sensitive volume per each detection event.

For each multi-element detector design, the geometry file was coded to reflect the design. Simulations were carried out for a wide range of mono-energetic neutron beams, from 10 keV to 2 MeV. For each incident neutron energy, a uniform planar neutron source with mono-directional emission was created. Each simulation was carried out for 5×10^8 normally incident neutrons. A tally was coded to write an output file reporting the energy deposited in a sensitive volume for each incident particle history. A schematic diagram of some of the decisions that are made to perform a simulation with Geant4 is shown in Figure 3.3.

More details on the Geant4 simulation code written to assess microdosimetric responses of the multi-element THGEM-based detectors can be found in Appendix A.

3.4 Results and discussion

3.4.1 Microdosimetric response

Figure 3.4 shows microdosimetric spectra simulated for multi-element detector designs for incident neutron energies of 75 keV, 1.0 MeV and 2.0 MeV. For the deposited energy of each detection event, the lineal energy is computed and distributed into equal

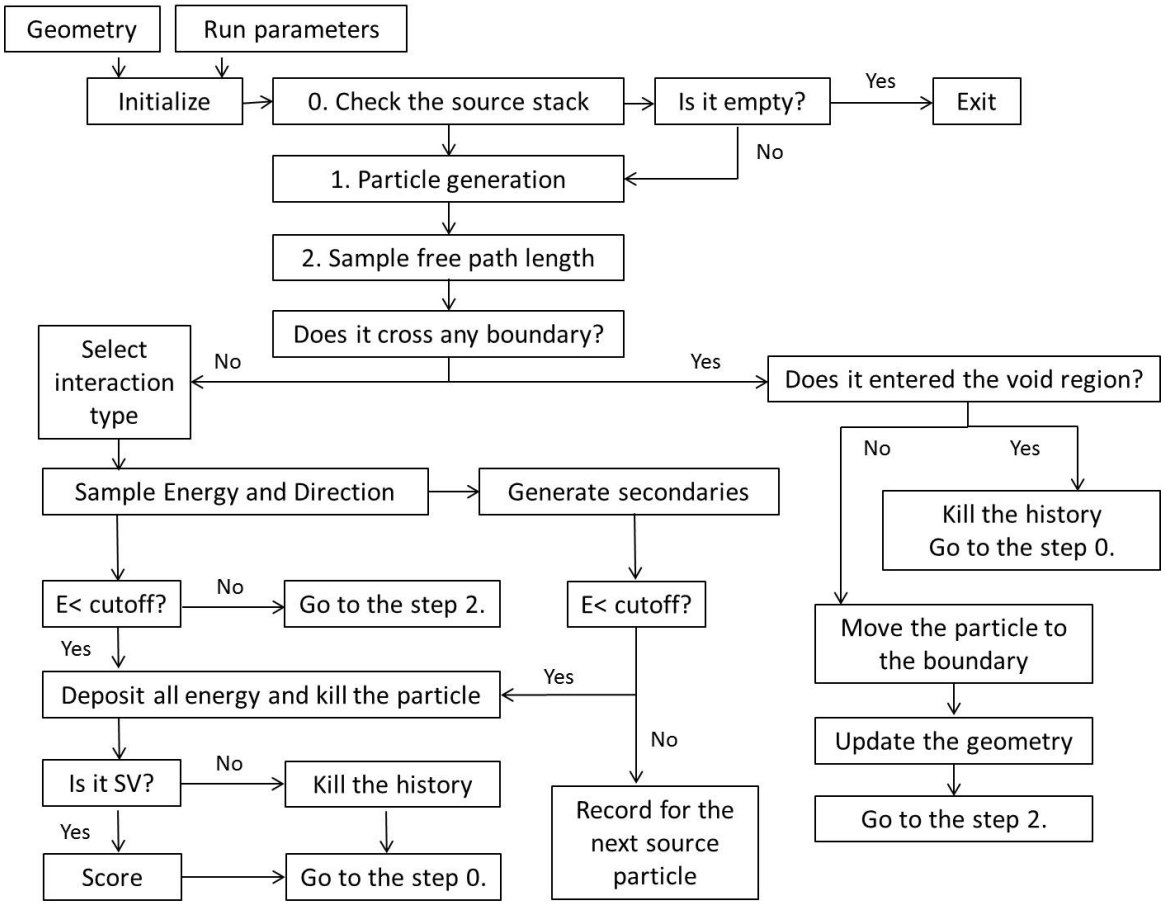

Figure 3.3: A schematic diagram of some of the decisions that are made to perform a simulation with Geant4.

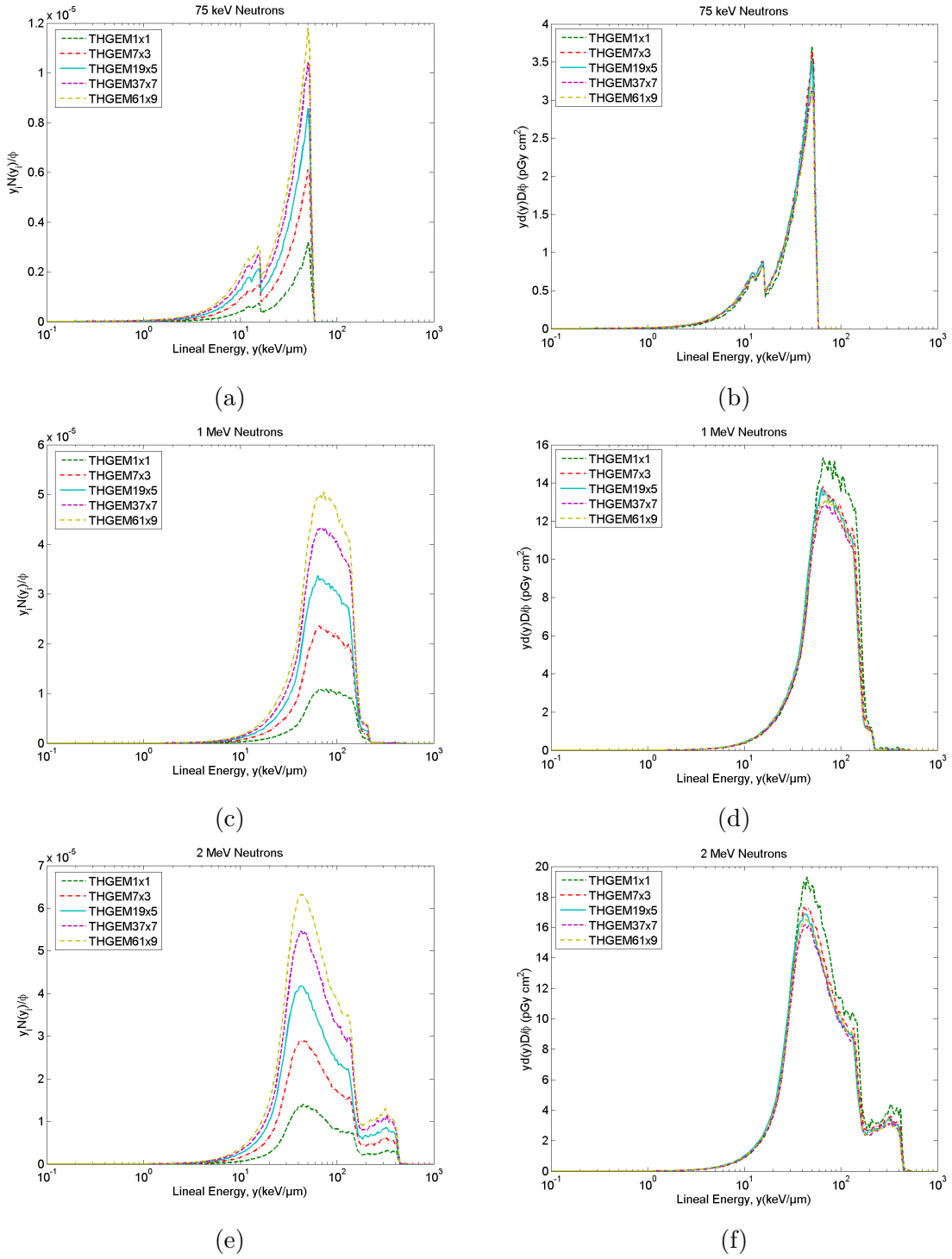

Figure 3.4: Microdosimetric spectra simulated for multi-element detector designs at the simulated site diameter of 2 μm.

logarithmic bins with a resolution of 60 bins per decade, which gives a detailed feature of the distribution while keeping sufficient smoothing of data. For each simulation data set, two semi-log plots were created. In both plots, the ordinate is multiplied by the lineal energy y such that the area under the curve between two values of y is proportional to the fraction of dose in that region. The two plots are different only in terms of normalization. In the left side plots, $N(y_i)$, the number of counts in the i^{th} logarithmic bin, was conserved in order to compare the number of the detected events while in the right side plots, $N(y_i)$ was converted into d(y), the probability density function of the absorbed dose, and the distribution was normalized to the absorbed dose D. As the integral of the function yd(y) in the logarithmic y scale (or the integral of d(y) in the linear y scale) physically means the fractional dose for a given y interval of interest, the integral of the yd(y)D distribution represents the absorbed dose. For convenience, both distributions were normalized by the incident neutron fluence, ϕ. The absorbed dose D for each simulation data set was determined by integrating the $y_i N(y_i)$ distribution. For a cylindrical gas cavity of diameter d_g [cm] and gas density ρ_g [g/cm^3], the absorbed dose is calculated as the following

$$D = \frac{(1.6 \times 10^{-16} J/keV) \sum_i (y_i \bar{l}_m)\ N(y_i)}{(10^{-3} kg/g)\ \rho_g \pi\ (d_g/2)^2\ d_g} = \frac{(1.358 \times 10^{-9})}{d_g^2} \sum_i\ y_i N(y_i)\ [Gy] \quad (3.1)$$

In the $y_i N(y_i)$ plots, it is apparent that the number of detected events increases with the increase of the number of the cavities at all neutron energies. A detailed quantitative analysis on detection efficiency follows below. In the yd(y) distributions, it is hard to find any difference in the distribution pattern between designs and all designs show a consistent microdosimetric response, except for slightly higher doses of THGEM1×1. This is caused by the neutron scattering effect with the plastic walls, which shifts the mean neutron energy to a lower energy and leads to a slightly lower fluence to dose conversion coefficient. However, it is not clear why the scattering effect is detectable from the THGEM1×1 to THGEM7×3 and not significant between the

Table 3.2: The neutron absorbed dose obtained from different THGEM detector configurations for the applied neutron energy range of 10 keV to 2 MeV. The values are in pGy cm^2.

Neutron Energy (keV)	THGEM1×1	THGEM7×3	THGEM19×5	THGEM37×7	THGEM61×9
10	0.385	0.381	0.369	0.364	0.364
25	0.949	0.924	0.872	0.870	0.842
50	1.853	1.819	1.707	1.710	1.647
75	2.716	2.666	2.515	2.524	2.413
100	3.696	3.608	3.363	3.368	3.217
250	7.434	7.318	7.025	6.926	6.803
500	12.324	12.195	11.774	11.586	11.549
750	15.873	15.734	15.327	15.020	15.078
1000	19.047	18.988	18.585	18.152	18.318
1250	22.363	21.975	21.599	21.046	21.261
1500	24.956	24.475	24.087	23.556	23.820
1750	27.122	26.740	26.335	25.673	25.921
2000	28.941	28.284	27.870	27.189	27.553

other designs. A response comparison between different cavity elements for a given design may reveal the underlying physics clearly.

The average absorbed doses per fluence are 2.567 pGy cm^2 at 75 keV, 18.618 pGy cm^2 at 1 MeV and 27.967 pGy cm^2 at 2 MeV, respectively. The discrepancy in absorbed dose with reference to THGEM1×1 is 7% at 75 keV, 2% at 1 MeV and 4% at 2 MeV, respectively. Therefore, all five designs show quite a consistent absorbed dose response. Table 3.2 shows the calculated absorbed doses obtained from different THGEM detectors.

At the neutron energy of 75 keV, there are additional peaks located at the lower energy side of the proton recoil peak. These are ^{12}C, ^{14}N and ^{16}O recoil peaks produced by the neutron elastic scattering with these nuclei in the gas [53]. As the neutron energy increases from 10 keV to 500 keV, the proton edge, the maximum y value produced by a recoil proton, extends to higher values of lineal energy due to increase in the amount of deposited energy inside the cavity volume. For the neutron energy above 500 keV, the maximum range of the recoil protons becomes larger than the cavity diameter and the proton edge appears at the y value of 136 keV/μm, which is independent of

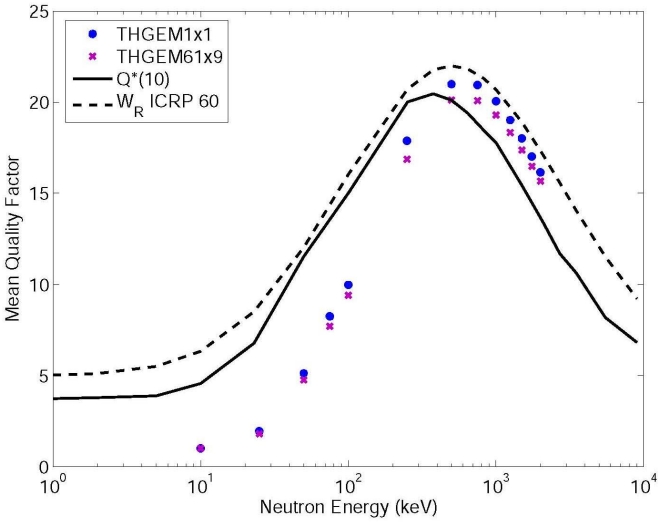

Figure 3.5: The computed mean quality factor, $\overline{Q}$, the radiation weighting factors, W_R, from ICRP 60 [2], and the values of $Q^*_{\text{eff}}(10)$ at the 10 mm depth in the ICRU sphere reported by Leuthold et al. [80].

the incident neutron energy [20]. When the neutron energy is further increased, the contribution of alpha particles and other heavy recoil ions such as carbon, nitrogen and oxygen appear beyond the proton edge.

3.4.2 Quality factor and dose equivalent responses

From each simulated lineal energy spectrum, the mean quality factor, $\overline{Q}$, at a given neutron energy was determined by

$$\overline{Q} = \int Q(y)\ d(y)\ dy \tag{3.2}$$

where Q(y) denotes the quality factor at the lineal energy y. The quality factor as a function of the lineal energy was obtained by approximating $y \simeq L$ and using the relationship between quality factor and LET, L, given by ICRP publication 60 [2].

Figure 3.5 shows the mean quality factor and the effective quality factor, $Q^*_{\text{eff}}(10)$, as a function of the neutron energy. $Q^*_{\text{eff}}(10)$ is defined as the ratio of the ambient

dose equivalent $H^*(10)$ and the ambient absorbed dose $D^*(10)$ at the 10 mm depth in the ICRU sphere. The $Q^*_{eff}(10)$ data are from the ref. [80]. For reference, the radiation weighting factor, W_R, from ICRP 60 [2] is also plotted. As already found out in Figure 3.4, there is little discrepancy between d(y) distributions for different detector designs, which leads to consistent $\overline{Q}$ values. Owing to this, only two sets of data, THGEM1×1 and THGEM61×9, were plotted in Figure 3.5.

As shown in the figure, the $\overline{Q}$ and $Q^*_{eff}(10)$ curves show a consistent pattern in the neutron energy region above 500 keV. The $\overline{Q}$ values slightly overestimate the $Q^*_{eff}(10)$ values with the maximum discrepancy of 13% in this energy region, that is to be expected within the uncertainties of experimental data.

In the lower neutron energy region, on the other hand, the $\overline{Q}$ curve shape deviates from the shape of the $Q^*_{eff}(10)$ curve and the deviation becomes steeper with the decrease of neutron energy. At 300 keV, the $\overline{Q}$ value underestimates the $Q^*_{eff}(10)$ value by 10%, which is tolerable, however, the underestimation is more significant at lower energies. This underestimation in quality factor stems mainly from the fact that the range of recoil protons is shorter than the simulated diameter (2 μm) in this energy region, as discussed earlier. This makes the approximation of LET by the lineal energy not valid. The underestimation problem has been reported in many articles [7, 30] and a simple way to minimize it is to keep the range of the charged particle as long as possible by operating the detector at lower pressures, i.e. by simulating smaller sites [38]. To this end, the designed multi-element detectors will be operated at a pressure corresponding to 0.5 or 1 μm in real operations rather than 2 μm simulation site size (see subsection 2.3.5).

The dose equivalent H at a given neutron energy was determined from each simulation data set by

$$H = D \times \overline{Q} \tag{3.3}$$

Figure 3.6a shows the computed dose equivalent per neutron fluence as a function of the neutron energy. For comparison, the ambient dose equivalent, $H^*(10)$, and

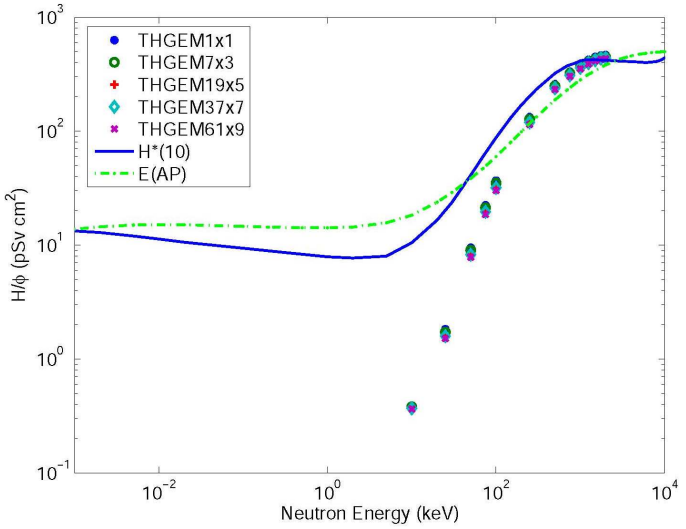

(a)

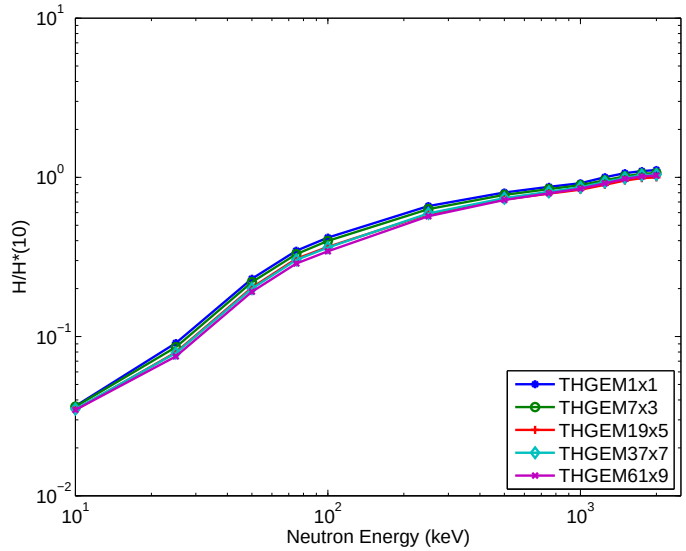

(b)

Figure 3.6: a) The computed values of dose equivalent normalized to neutron fluence, H/ϕ, the ambient dose equivalent, H*(10)/ϕ, and effective dose, E(AP)/ϕ, defined by ICRP 74 [4]. b) Relative dose equivalent response, R_H, as the ratio of calculated dose equivalent to true H*(10) for all simulated designs as a function of the incident neutron energy.

effective dose, E(AP), from ICRP 74 [4] were also plotted. In Figure 3.6b, the relative dose equivalent response R_H, defined as the ratio of the dose equivalent value from a multi-element detector to true $H^*(10)$ is given. The dose equivalent values from different designs are consistent with each other, which is in agreement with the fact that both mean quality factors and absorbed doses are consistent between different designs.

Overall, the ambient dose responses of the multi-element designs are acceptable in the MeV energy region; however, the responses are relatively poor in the energy region below 300 keV. This problem has already been reported in the pioneering works on TEPC-based radiation protection dosimetry [7, 30].

The underestimation in H comes partly from the underestimation in the mean quality factor $\overline{Q}$, but predominantly from the geometric difference between the ICRU sphere and the THGEM multi-element detectors. Since the ICRU sphere is a large volume sample exposed to a neutron field and modifies the neutron field by scatterings, in some energy region the neutron spectrum and the fluence rate at the 10 mm depth becomes significantly different from those of the incident field. Therefore, if the contribution of the scattered neutrons to H is not negligible, it is unavoidable that real radiation detectors can hardly meet radiation absorption at the 10 mm depth of the ICRU sphere.

To overcome the underestimation problem, Schuhmacher et al. carried out a Monte Carlo simulation study [7] on the use of a 0.5 inch TEPC embedded at 1 cm depth in a spherical tissue-equivalent phantom of 30 cm diameter. As their geometry is very close to the definition of $H^*(10)$, the simulated ambient dose equivalent response was extremely good in a wide energy range. In spite of the promising result, this idea can not be adopted to the present study due to a small detector size and low efficiency as well as a poor angular response expected from the geometry. Another way is to add moderators on the outer surface of the detector. In a Monte Carlo simulation study on optimizing the detector design [38], 1.5 cm thick polyethylene moderator enhanced

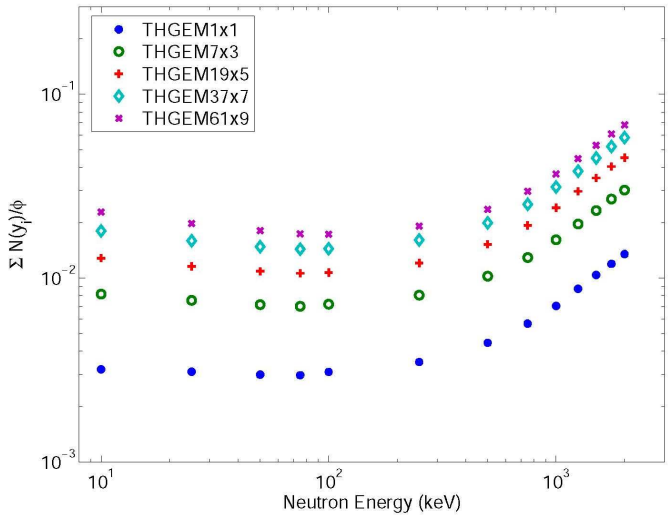

Figure 3.7: The efficiency of the detector per unit neutron fluence as a function of neutron energy.

the ambient dose equivalent response significantly as discussed in chapter two.

3.4.3 Detection efficiencies

To do a quantitative comparison of neutron detection efficiencies between different multi-element detector designs, the efficiency values for each design were computed from the Geant simulation results. For convenience, the efficiency is defined in two ways in this study: $\sum N(y_i)/\phi$, the number of total detected events per incident neutron fluence and $\sum N(y_i)/H$, the number of total detected events per dose equivalent. The former is most frequently used for any kind of neutron detector while the latter is vital information as a dose equivalent meter.

Figure 3.7 shows $\sum N(y_i)/\phi$ for different detector designs as a function of the neutron energy. The efficiency of the THGEM61×9 design is higher than the efficiency of the THGEM1×1 by a factor of 5.6 at 100 keV and a factor of 5.2 at 1 MeV. From the figure, it is evident that the high density multi-element arrangement can enhance the efficiency by about a factor of 5.6 over the single-element detector with an equivalent

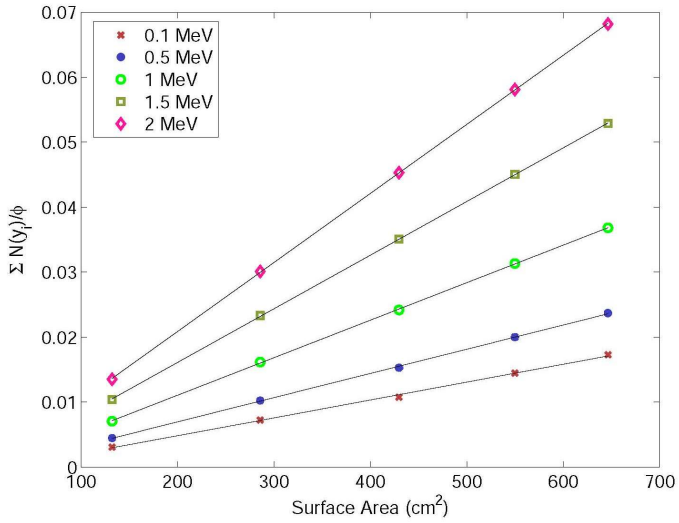

Figure 3.8: The efficiency of the detector per unit neutron fluence as a function of detector surface area.

volume. To observe the efficiency dependence on the detector surface area, $\sum N(y_i)/\phi$ is presented as a function of the surface area of each design in Figure 3.8. For all neutron energies, the efficiency increases in a linear fashion with the surface area. The linear slopes are 2.75×10^{-5} for 100 keV and 5.78×10^{-5} for 1 MeV, respectively.

Figure 3.9 shows the detection efficiency in terms of detected events per unit dose equivalent, $\sum N(y_i)/H$, as a function of the neutron energy. The energy dependence of this efficiency is a little different from Figure 3.7, given that the dose equivalent includes the fluence to absorbed dose conversion coefficient and quality factor, both of which have neutron energy dependencies. Again, the efficiency at a given neutron energy is strongly dependent upon the detector design. The efficiency of the THGEM61×9 design is higher than the efficiency of the THGEM1×1 by a factor of 9.8 at 100 keV and a factor of 7.5 at 1 MeV.

Table 3.3 lists the radiation protection parameters described earlier for the THGEM61×9 at the applied neutron energy range.

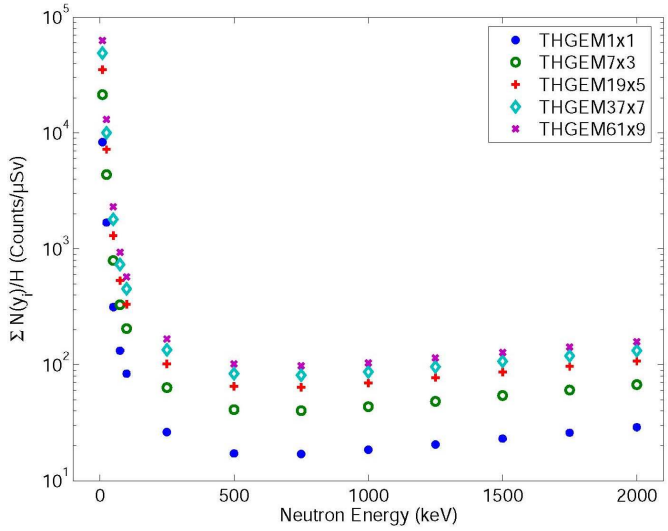

Figure 3.9: The efficiency of the detector per unit dose equivalent as a function of neutron energy.

Table 3.3: The calculated radiation protection parameters obtained with THGEM61×9 for monoenergetic neutrons for energy range of 10 keV to 2 MeV.

Neutron Energy (keV)	Detection Efficiency (counts/μSv)	Dose ϕ^{-1} (pGy cm^2)	H ϕ^{-1} (pSv cm^2)	$\overline{Q}$
10	63009	0.4	0.4	1.0
25	13099	0.8	1.5	1.8
50	2308	1.6	7.8	4.8
75	937	2.4	18.6	7.7
100	572	3.2	30.2	9.4
250	167	6.8	114.7	16.9
500	102	11.5	232.1	20.1
750	98	15.1	302.8	20.1
1000	104	18.3	353.4	19.3
1250	115	21.3	389.6	18.3
1500	128	23.8	413.7	17.4
1750	142	25.9	427.0	16.5
2000	158	27.6	431.4	15.7

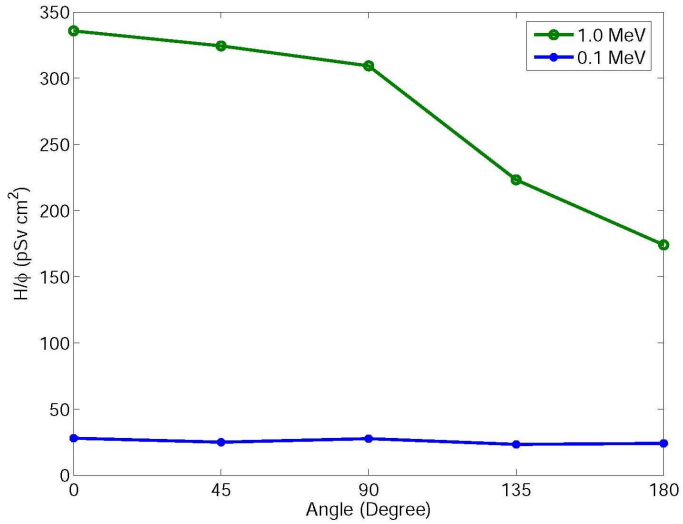

Figure 3.10: Angular response of the THGEM 61×9 design.

3.4.4 Angular response

Using the 61×9 design, Geant4 simulations were carried out to investigate the angular response of the THGEM multi-element detector. The lineal energy spectra were collected for the incidence angles of 0°, 45°, 90°, 135° and 180° relative to the central vertical axis of the detector.

Figure 3.10 shows the angular responses of the detector for 0.1 and 1.0 MeV neutrons. For 100 keV neutrons, the dose equivalent is almost independent of angle and the response is close to the ideal case. On the other hand, for 1.0 MeV neutrons, there is a significant angular dependence and the dose equivalent at 180° is about a half of the value at 0°. A similar angular dependence was reported in our previous publication [53] on the 5×5 mm single element cavity detector.

The angular dependence could be explained by the contributions of the wall interactions. For 0.1 MeV, the wall interaction contribution is negligible while for 1.0 MeV, the wall interactions dominantly contribute to the cavity dose. The THGEM assembly option 1 (Figure 3.2b) was employed in angular dependence simulations. In this case, for large incident angles, only the recoil particles from the Rexolite insulator can reach

the gaseous sensitive volume; This is the gaseous volume above the THGEM layer. If the option 2 (Figure 3.2b) is employed, it is expected that the angle dependent doses at 0° and 180° will be about 75% of the 0° dose for the option 1 while the dose at 90° will be about 90%. Therefore, an enhanced angular response may be able to be achieved by taking the option 2.

3.5 Conclusion

To overcome the complicated fabrication and assembly process required for building the multi-element microdosimetric detectors using the traditional proportional counter technology, versatile multi-element detector designs based on THGEM were presented. Through extensive Geant4 Monte Carlo simulations, neutron microdosimetric, quality factor and dose equivalent responses were investigated for five different designs including the conventional single cavity configuration. Moreover, the dependence of the detection efficiency on the multi-element design was systematically analyzed.

In the microdosimetric and absorbed dose responses, all multi-element designs were consistent and were in excellent agreement with the conventional single volume detector within 4%. These close agreements indicate that the perturbation of the incident neutron field by adding additional plastic walls in the multi-element detectors is negligible. Given that the efficiency increases rapidly from the 1×1 to the 37×7 design while the efficiency increase is slowed down from the 37×7 to the 61×9 design, the 37×7 design could be chosen as a reasonable compromise.

In the analyses of the quality factor and dose equivalent responses, the responses were overall reasonable. However, notable underestimations were identified in the neutron energy region below 300 keV. A gas pressure corresponding to 0.5 or 1 μm rather than 2 μm simulation site size will be beneficial to address the quality factor underestimation [38]. To enhance those under-responses in this energy region, additional simulations will be carried out in search for a better design. To this end, a single

element detector was covered with a polyethylene moderator of varying thicknesses in ref. [38], which led to a greatly enhanced response with a 2 cm thick moderator.
Given that option 1 showed a severe angular dependence for MeV neutrons while the option 2 is expected to give a better angular response with slightly lower efficiency, the option 2 will be pursued as priority. Moreover, the option 2 is preferable for keeping the high voltage leakage current minimum. After successful development, the THGEM multi-element detector can be used for neutron dose equivalent measurements at nuclear power plants and other neutron facilities.
In the next chapter, the construction procedure and technical consideration in development of a prototype multi-element THGEM detector are described. Among the proposed detector designs in this chapter, the prototype detector is developed based on the simplest design, i.e. the THGEM7×3.

Chapter 4

Construction of the designed THGEM-TEPC and Procedures

4.1 Introduction

To address the structural complication that is unavoidably encountered with the traditional technology, a THGEM-based multi-element neutron dosemeter was proposed. The Monte Carlo simulation results reported in the previous chapter gave clear insight on the neutron efficiency dependence on the multi-element geometry. This chapter describes a THGEM multi-element neutron detector consisting of 21 sub-elements that was developed as a proof of principle. The prototype detector is founded on the Monte Carlo simulation study and the previous work of our group using THGEM TEPC technology [53, 54, 73, 81]. In the following sections, the prototype detector structure, the essential components and the design considerations are fully described. The signal stability and fundamental performance of the THGEMs were tested using an internal ^{244}Cm alpha source and the results are presented. Moreover, the quality of the vacuum tightness of the aluminum chamber and the ability of the chamber to maintain a stable filling gas pressure were ensured through long term (several days) measurements. The work presented in this chapter was accepted for publication in Nuclear Instruments

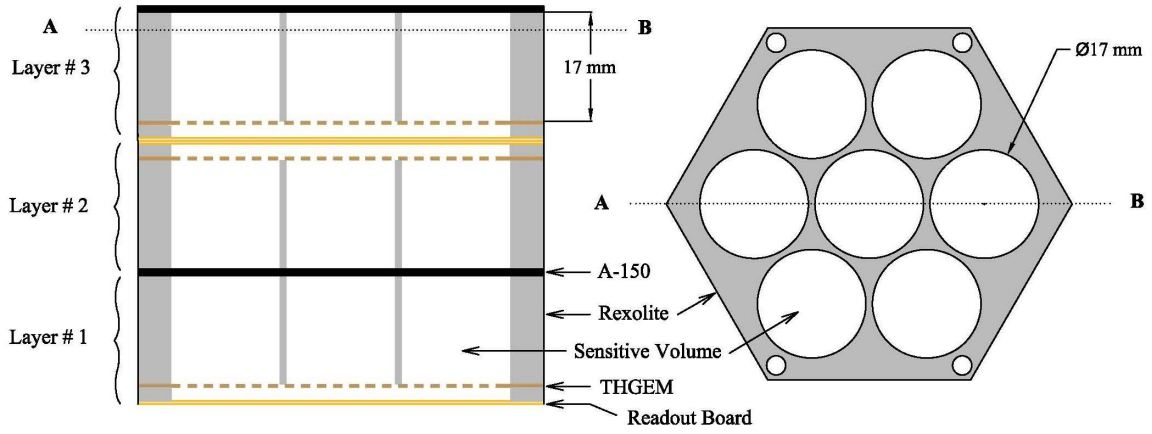

Figure 4.1: Side and top cross sectional views of the prototype multi-element TEPC. Each Rexolite insulator layer houses a hexagonal array of seven cylindrical gas cavities with equal heights and diameters of 17 mm and is sandwiched between a layer of A-150 cathode and a THGEM electrode. The charge collection region is located next to the THGEM in each layer.

and Methods in Physics Research A [82]. The detector design and fabrication work was performed by the author of this dissertation under the supervision of Dr. Soo Hyun Byun and with guidance of Dr. Bill Prestwich and Dr. Andrei Hanu.

4.2 Detector Description

Fig. 4.1 shows the layout of the prototype multi-element THGEM microdosimetric detector. As shown in the figure, the detector consists of three alternating layers of Rexolite insulator (Rexolite 1422, C-LEC Plastics, Inc.) hexagons. Each layer houses a hexagonal array of seven cylindrical gas cavity elements, known as the sensitive volumes, with equal heights and diameters of 17 mm so that the final detector structure consists of 21 sub-elements. To pump out the air and fill the sensitive volumes with the operating gas, a set of grooves has been machined on the top and bottom of the Rexolite insulator. The wall thickness between each sub-element was kept to at least 1 mm to satisfy the charged particle equilibrium condition for neutrons with the energies

up to 10 MeV. In each layer, the Rexolite insulator is sandwiched between a 1 mm thick A-150 conducting plastic and a THGEM layer. The charge collection regions are located next to each THGEM layer and consist of common readout boards that are separated from the THGEM layer by employing an arrangement of ceramic spacers with a thickness of 1 mm. Four holes are drilled on the corners of all layers to position various layers during assembly.

As presented schematically in Fig. 4.2, for a single sub-element, the distinct gas regions provide three different functional areas:

a) the conversion and drift region, i.e. the region between the drift electrode and the THGEM.

b) the multiplication area inside the THGEM holes.

c) the charge collection gap, i.e. the region between the THGEM electrode and the readout board.

In this design, each A-150 layer serves as the cathode. The gas cavities in the Rexolite layers form conversion and drift gaps, in which the electrons are produced by ionization and drift along the electric field toward the THGEM layer. With the application of a high potential difference between the top and bottom of the THGEM, a strong electric field is produced inside the THGEM holes, where electron multiplication happens. The electric field strength inside the THGEM holes is strong enough to initiate an electron avalanche. After multiplication, by the use of an efficient potential difference across the collection gap, the avalanche electrons are collected by a common collection electrode. The amplitude of the collected signal by the readout anode is linearly proportional to the total deposited energy of a single event. While each individual sub-element operates as an independent detector, the signal outputs of all layers are united to provide a single output. It should be noted that for stacking layers, as shown in Fig. 4.1, the positions of the constituent materials for the layer number 2 are mirrored to avoid having the cathodes and readout electrodes next to each other and minimize the leakage current across the neighboring layers. As discussed in the previous chapter

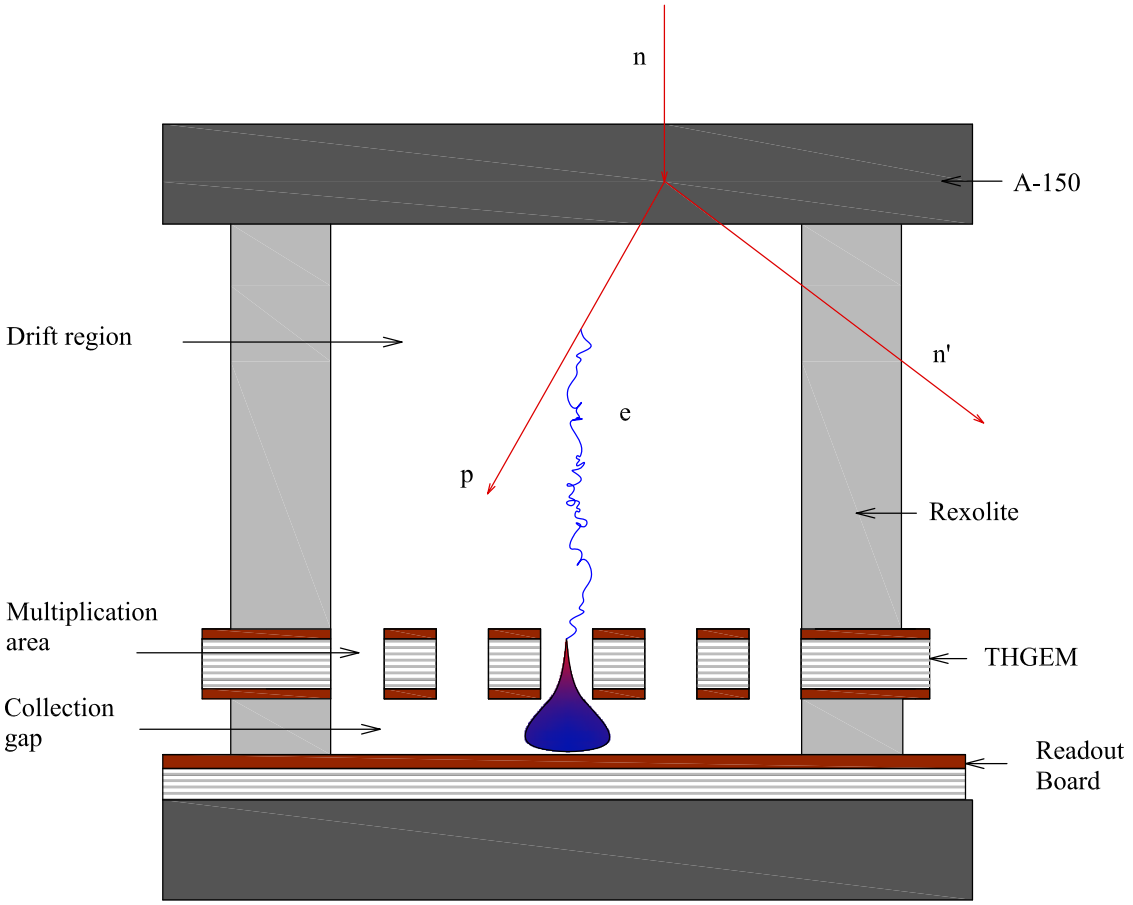

Figure 4.2: A schematic view of different functional gas areas in a single gas cavity of the prototype THGEM-based detector. The distinct gas regions provide three different functional areas: a) the conversion and drift region, b) the multiplication area and c) the charge collection gap.

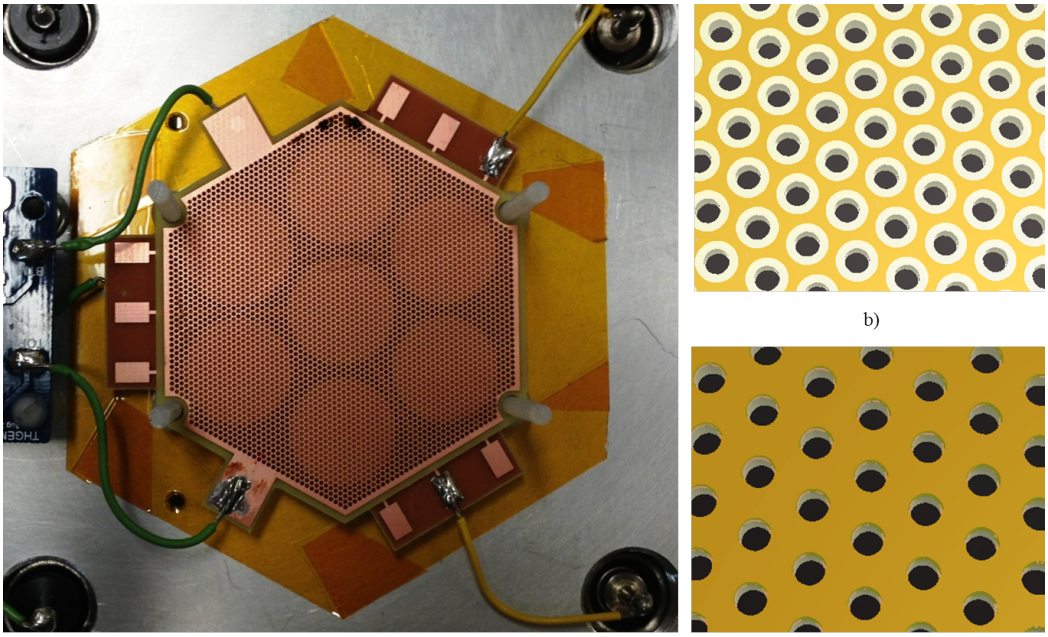

Figure 4.3: a) A photograph of a spark damaged THGEM and the 3D views of THGEM b) with rim around the holes and c) without rim.

and Ref. [73], it is expected that this configuration will have a slightly lower efficiency but a better angular response over the other case.

4.3 THGEMs

Fabricated using standard printed circuit board manufacturing techniques, the THGEM layout employed in this study is composed of a 0.4 mm FR4 insulator coated with 0.05 mm of copper on both sides with a hexagonal pattern of 0.4 mm diameter holes and a hole pitch of 0.8 mm.

The responses of two sets of THGEMs were studied in this research. In the first set which was ordered from MyroPCB Inc. (www.myropcb.com), double-sided copper-clad plates were drilled with almost 4000 holes per unit and a 0.1 mm etched rim, a metal free clearance ring, around each hole. A THGEM with etched rim geometry is recommended as the optimum THGEM design [83–85] in terms of multiplication gain

improvement and THGEM stability for low gas pressure counters. But as is discussed by Hanu [74] and was observed during the experiments (see Chapter 6), having an eccentric hole-rim pattern over a relatively large effective area makes the THGEM more open to spark induced breakdowns and having multiple gains issue. Therefore, it was decided to employ the THGEM design with no rim around holes. THGEMs without rim were ordered from Milplex Circuit Inc. (www.milplexcircuit.com) which offers a more precise drilling and polishing technique as well as a computerized quality control system to detect imperfections in the final product. A photograph of a spark damaged THGEM within the detector assembly and the 3D views of THGEM with and without rim are included in Figure 4.3.

After drilling, to have better shaped holes and avoid copper debris produced during drilling, a combination of a mechanical brushing procedure using pumice stone followed by rinsing with high pressure water, and a micro etch chemical process was employed. The chemical contains approximately 10% nitric acid. Finally, THGEMs were washed with demineralized water and dried in an oven at 180 °C for 24 hours. This procedure helps to avoid high electric field values for sharp edges and have a better field uniformity [86]. The post production procedures are fully described in chapter 6.

4.4 Construction Procedure

4.4.1 Detector Assembly

Photographs of the fabricated detector components are shown in Figure 4.4. All electrodes and insulators are hexagons with a side dimension of 3.18 cm. Moreover, an aluminum vacuum chamber was designed and constructed to encase the entire detector assembly. Designed to be used in the neutron microdosimetry measurements, the assembled aluminum chamber is capable of keeping a steady pressure of several torr. This guarantees the reproduction of the measurements over an adequate data acquisition time.

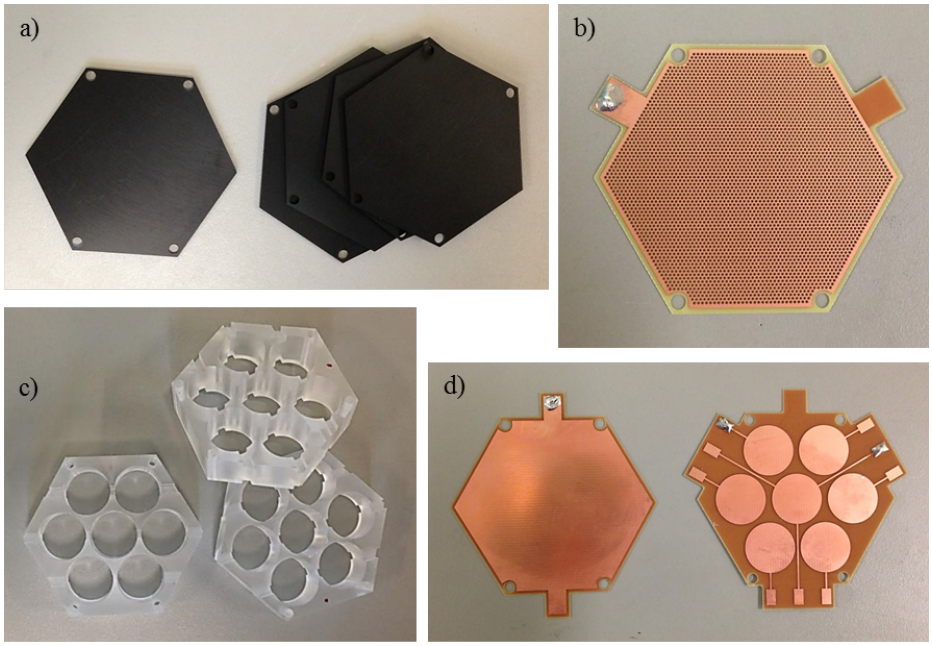

Figure 4.4: THGEM detector components a) A-150 plastic b) THGEM c) Rexolite isolator d) read-out boards with single and multiple signal outputs.

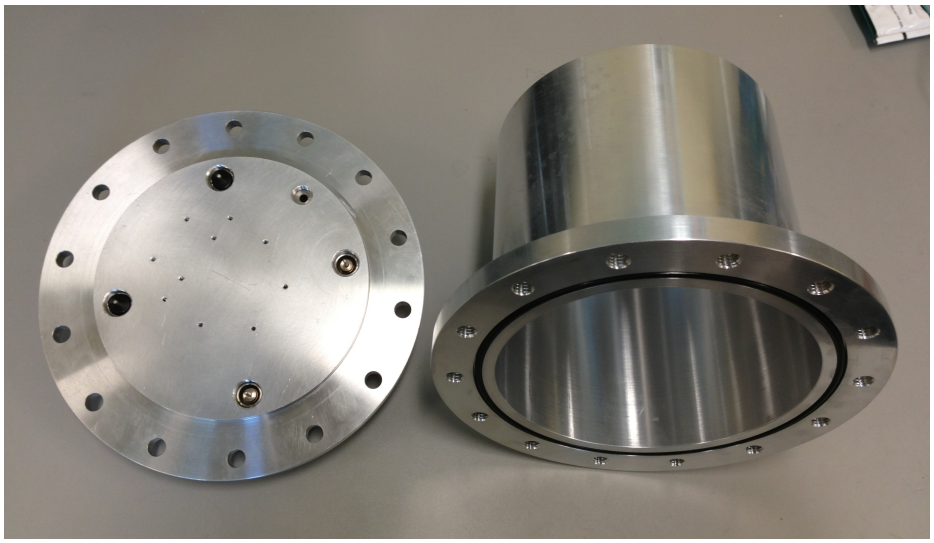

Figure 4.5: A photograph of the prototype detector aluminum chamber. The chamber consists of two pieces: a base and a cylindrical cap.

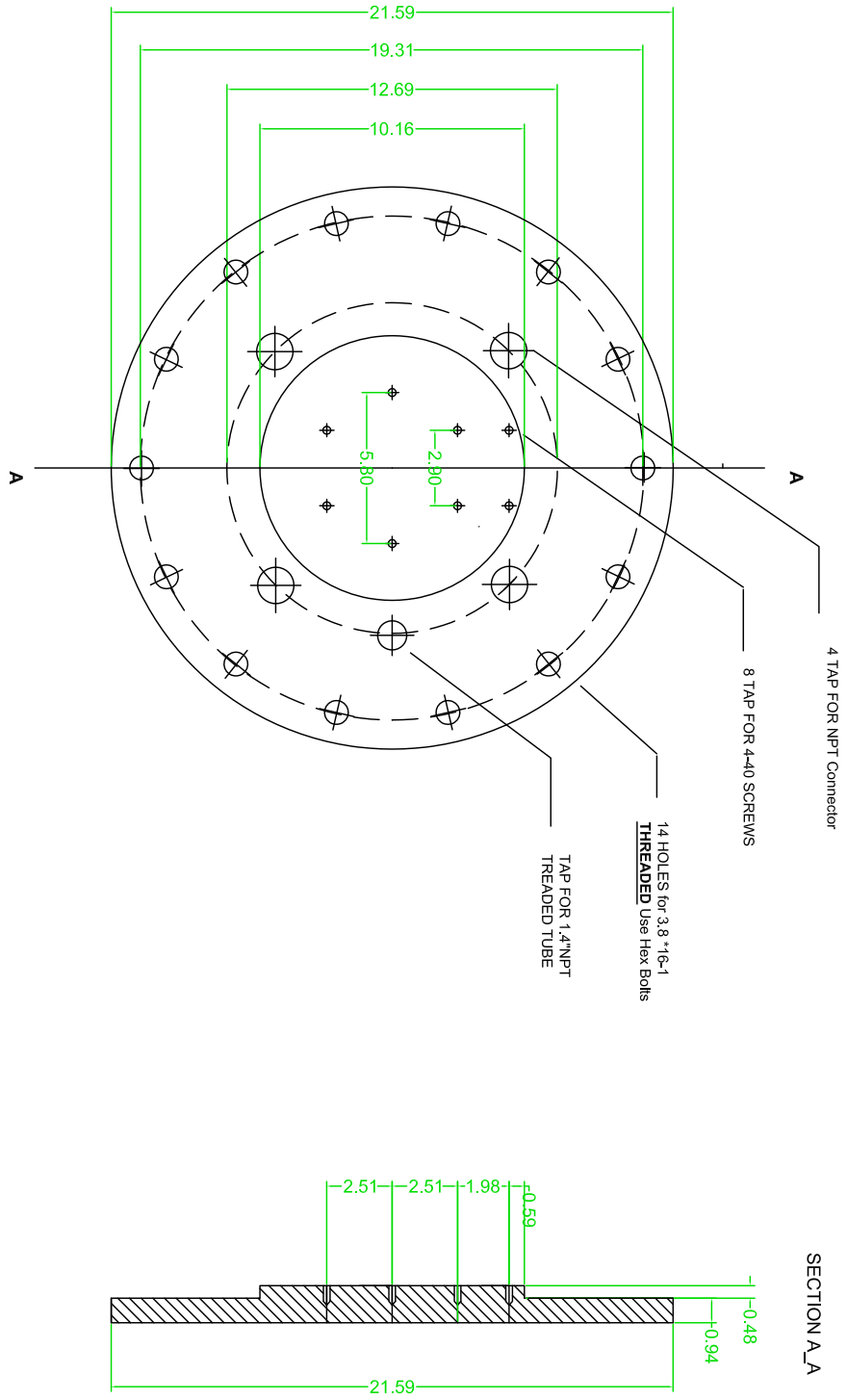

Figure 4.6: The details of the aluminum vacuum chamber designed to encase the prototype detector.

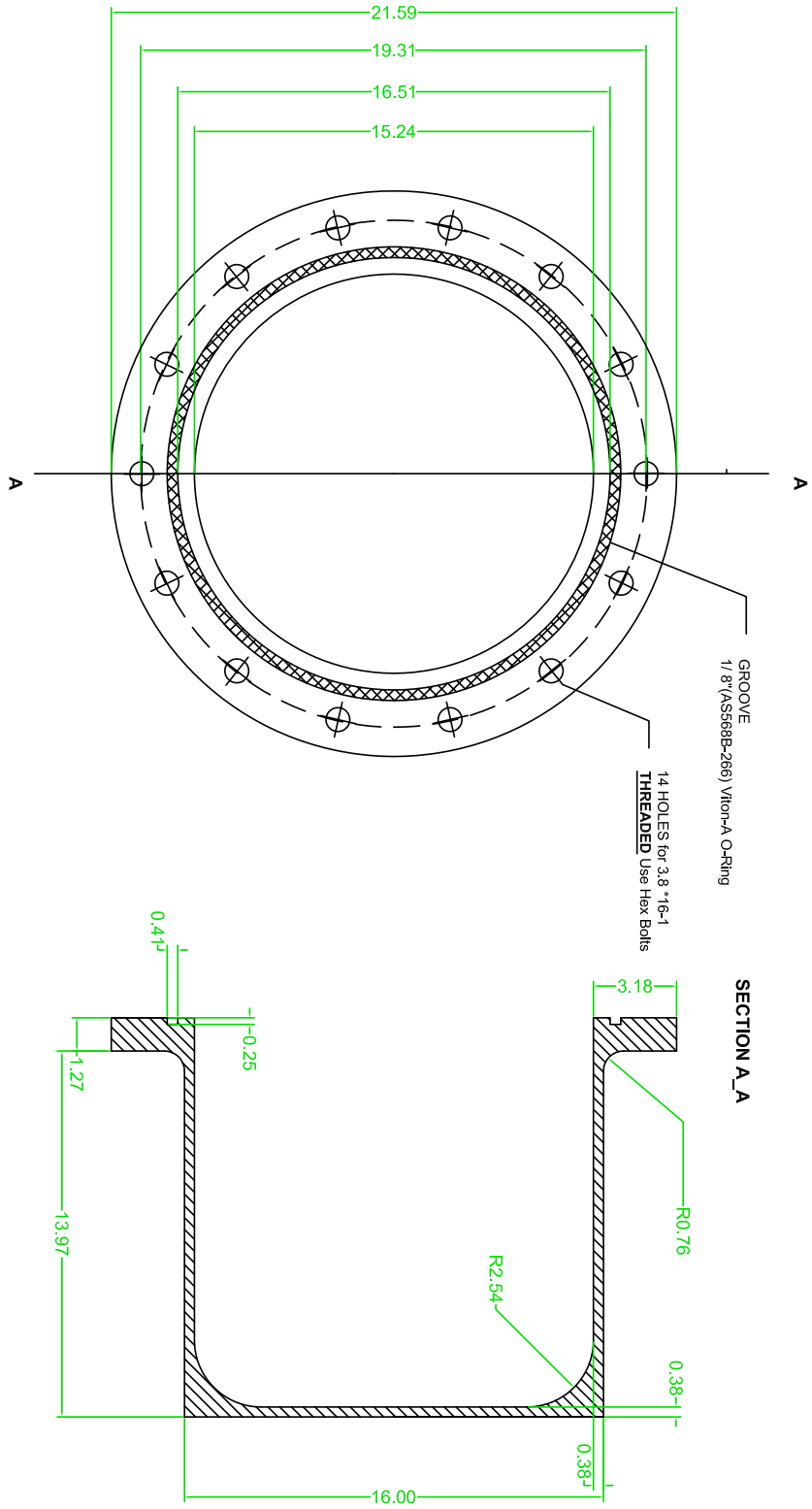

Figure 4.7: The details of the aluminum cap designed for the prototype detector vacuum chamber.

The chamber consists of two pieces: a base and a cylindrical cap. Carrying the assembled THGEM detector, the base houses two high voltage (SHV5) and two BNC signal connectors as well as a gas filling port. The hermetic sealed connectors were glued to the chamber base using a low out-gassing epoxy (Loctite 1C Hysol) to maintain the required gas tightness. The epoxy glue used has a typical curing period of 24 hours. During assembly, the electrical wire connections of the high voltage divider, THGEMs, cathodes and connectors were carefully insulated.

A 3 mm thick cylindrical enclosing cap was made to ensure that the container does not disturb the incoming radiation beam and yet is capable of tolerating the vacuum pressure of 10^{-3} torr. A photograph of the aluminum container before inserting the THGEM detector is shown in Figure 4.5. The details of the chamber design is included in Figure 4.7 and Figure 4.6.

After assembling, the vacuum chamber was sealed using a Viton O-Ring (ordered from Able Seal & Design Inc., www.ablesealanddesign.ca) and degassed using a rotary vane vacuum pump to a gas pressure below 10^{-3} torr using a custom made setting depicted in Figure 4.8. After vacuuming for a couple of days to remove all trapped air and absorbed gasses, the detector was filled with propane-based tissue equivalent gas, consisting of 55.0% C_3H_8, 39.6% CO_2 and 5.4% N_2, at the pressure of 49.1 torr to simulate the energy loss pattern of charged particles in 2 μm of soft tissue.

The type of the filling gas and its pressure are among the variables that influence the electron multiplication gain of the detector. Propane and methane based tissue equivalent gases are most common options for the filling gas used in microdosimetry of mixed neutron gamma radiation fields. Both methane and propane based tissue equivalent gases are commercially available. A propane based mixture was developed by Srdoc [77]. The propane mixture permits higher gas gains compared to the methane mixture [87]. However, the methane based mixture more closely models the ICRU muscle tissue composition [88].

Table 4.1 summarizes some general characteristics of the standard 2 inch TEPC and

Table 4.1: General characteristics of the standard 2" TEPC and the prototype multi-element THGEM-based TEPC.

	2" TEPC	Prototype Detector
Geometrical Shape	Spherical	Cylindrical
SV Dimensions (cm)	5.1	1.7
Number of Sub-elements	1	21
Simulated Diameter (μm)	2	2
Mean Chord Length (μm)	1.33	1.33
SV Surface Area (cm^2)	81.67	285.85
Mass of Gas (mg)	2.7	9.53
Gas Pressure (torr)	16.4	49.08

the prototype multi-element THGEM-based TEPC. The prototype detector has an overall size comparable to the standard 2 inch TEPC.

4.4.2 Electronics and Signal Processing

Figure 4.9 represents a schematic diagram of the bias voltage connections to the different components of the prototype THGEM detector. In each layer, a negative high voltage (HV) of several hundred volts was applied to the A-150 as the detector drift cathode, while the readout board was kept at ground potential. By employing a custom made voltage divider circuit, the top and bottom layers of the THGEMs were biased to produce an avalanche electric field inside the THGEM holes and to direct the electron cloud to the collection readout board in each layer. The values of resistors are 10 and 2 MΩ and were chosen as recommended by Orchard [54] and Hanu [53] to provide an efficient potential difference across the THGEM and collection gap. Using the basic principle of a resistor ladder, the voltage difference across the THGEM copper layers denoted by ΔV_{THGEM} is equal to

$$\Delta V_{THGEM} = \frac{10M\Omega}{10M\Omega + 2M\Omega} \times THGEMHV \tag{4.1}$$

The A-150 layers and THGEMs were biased by using two separate power supply units (Bertan Associates Model 305). For all measurements, the drift potential difference

Figure 4.8: The vacuum set up used with the prototype THGEM-based TEPC. The vacuum was made with a rotary vane vacuum pump. After vacuuming, the detector was filled with propane-based tissue equivalent gas at the pressure of 49.1 torr to simulate the energy loss pattern of charged particles in 2 μm of soft tissue.

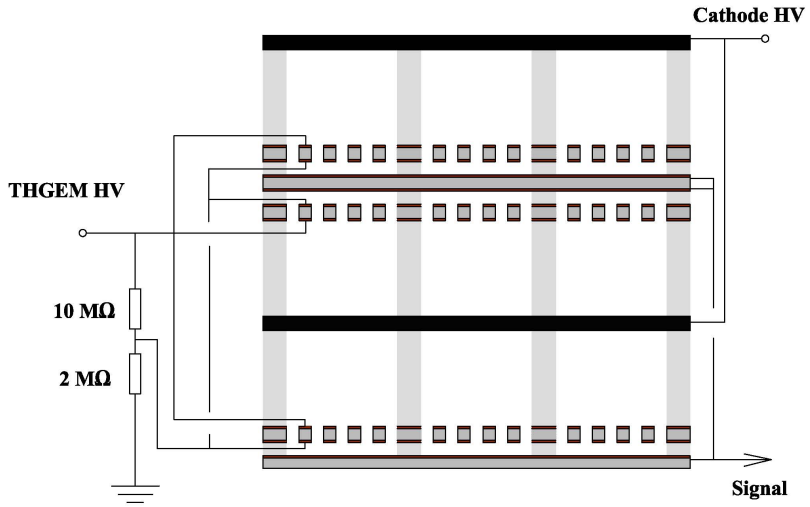

Figure 4.9: A schematic diagram of the bias voltage connections of the Prototype multi-element THGEM detector.

across A-150 and THGEM was chosen to be a hundred volts. A photograph of the multi-element THGEM detector within the aluminum casing is shown in Figure 4.10. The output signal of the THGEM detector was connected directly to a low-noise charge sensitive preamplifier (Model A1422, CAEN) located as close as possible to the detector. To process pulse signals from the detector, the preamplifier output signal was connected to a commercial digital pulse processing system (Model DSPEC, Ortec) with 14-bits of resolution. The gain settings and THGEM operating high voltage were adjusted so that all of the events can be entirely covered in one spectrum. During all measurements the preamplifier and amplifier traces were continuously monitored on an oscilloscope. A schematic diagram of the pulse processing chain used in experimental measurements is depicted in Figure 4.11.

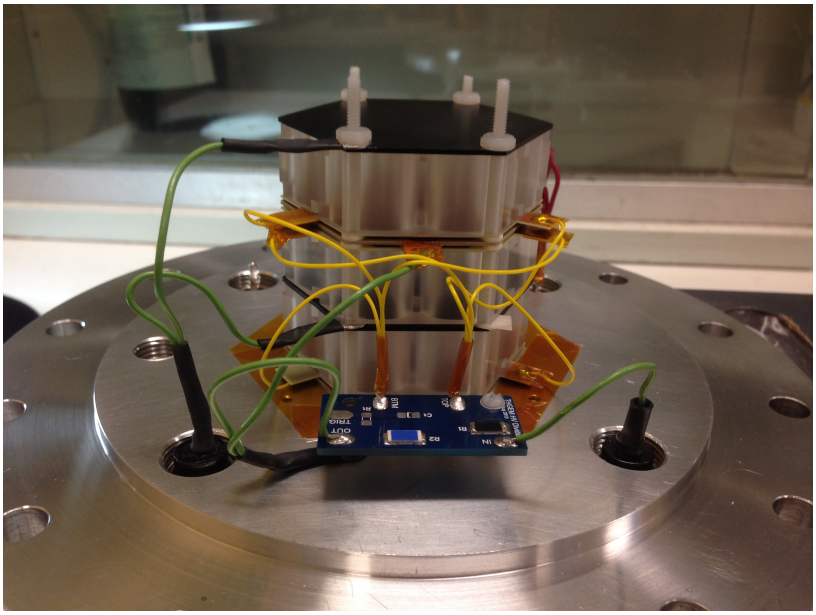

Figure 4.10: A photograph of the multi-element THGEM detector within the aluminum casing.

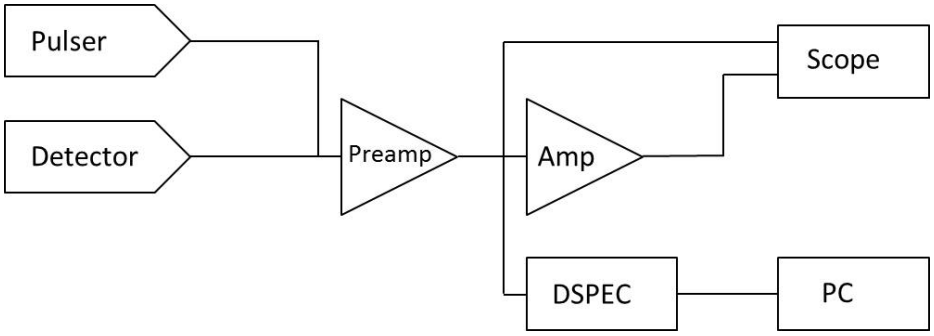

Figure 4.11: Schematic diagram of the pulse processing chain used in experimental measurements.

4.5 THGEM Operation and Stability Tests

For each THGEM sample, prior to taking neutron-gamma field measurements, its multiplication gain and stability was tested using a ^{244}Cm alpha source. For this test, the A-150 cathode was replaced with a 2 mm thick copper plate with a 1 mm diameter collimation hole at the center (see Figure 4.12). The ^{244}Cm alpha source was

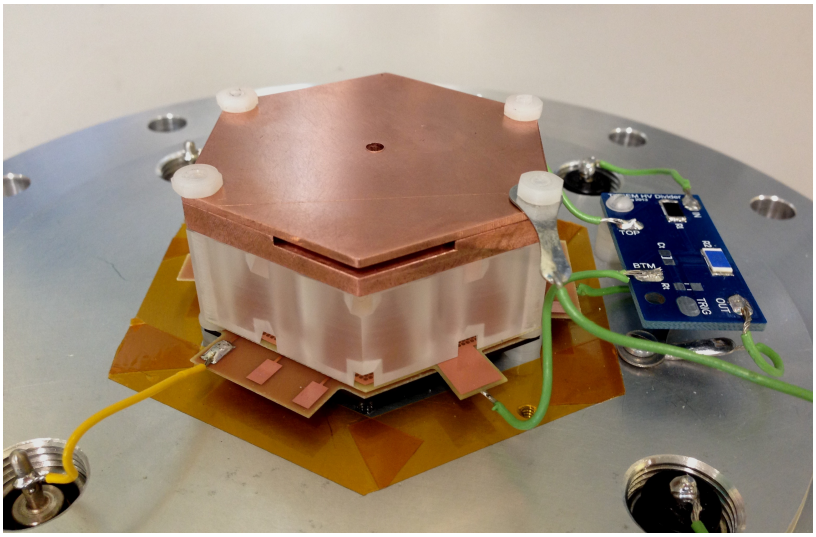

Figure 4.12: A photograph of the counter layout for alpha source measurements. A beam collimator was made from copper to hold the ^{244}Cm source inside the THGEM detector.

placed on top of the copper cathode. Figure 4.13 displays the experimental setup and the preamplifier and shaping amplifier traces on the oscilloscope along with the pulse height spectra collected from the MCA output.

Prior to collecting pulse height spectra, the signal dependence on the applied potential across the THGEM, ΔV_{THGEM}, was investigated. The amplitude of the observed pulse from the shaping amplifier is plotted as a function of ΔV_{THGEM} in Fig. 4.14. The first indication of signal for this data collection set was found at ΔV_{THGEM} of 290 V. As expected, the observed pulse height increases exponentially with the applied voltage after a small shoulder at the beginning. Discharge was observed above ΔV_{THGEM} of 550 V. Nevertheless, by lowering the high voltage, the detector operation returned back to the normal condition.

Fig. 4.15a shows a pulse height spectrum measured for the ^{244}Cm source along with a Gaussian fit. For this spectral collection, the cathode was biased to -750 V and THGEM setup biased to -650 V which corresponds to 540 V across the THGEM layer. The average count rate was about 10 counts per second (cps). Compared to the

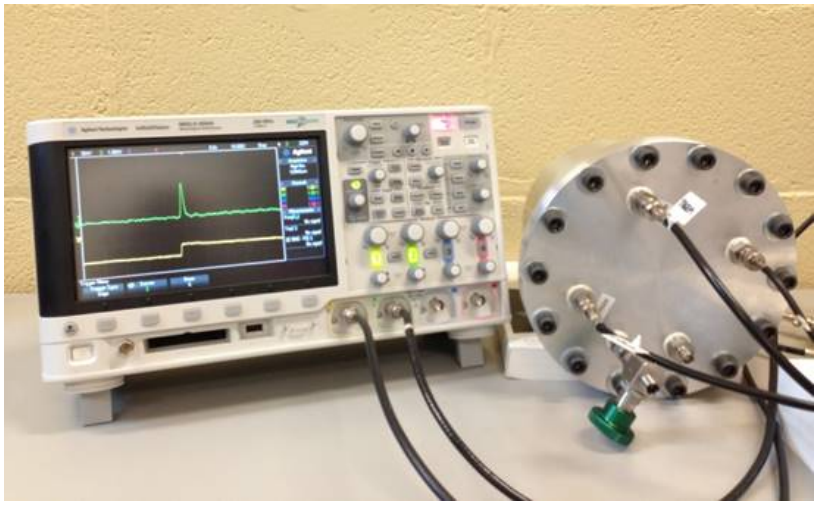

(a)

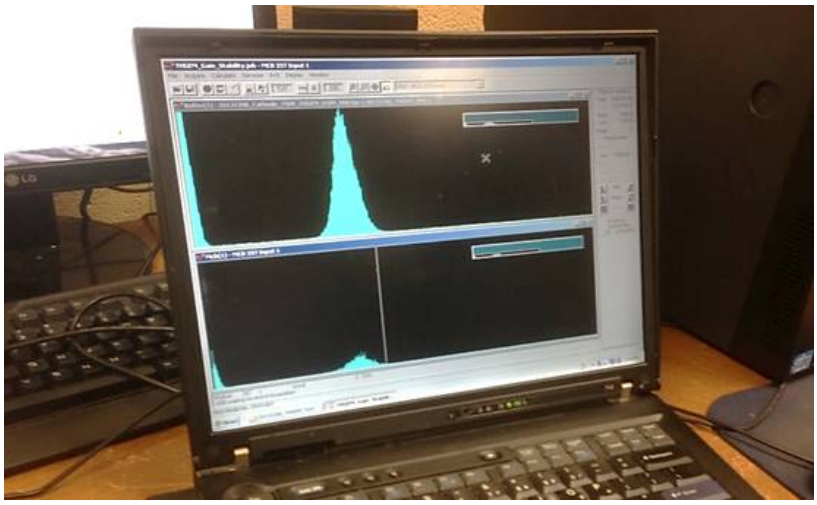

(b)

Figure 4.13: a) The experimental setup and the preamplifier and shaping amplifier traces on the oscilloscope along with b) the pulse height spectrum collected using the MCA output from the ^{244}Cm alpha source.

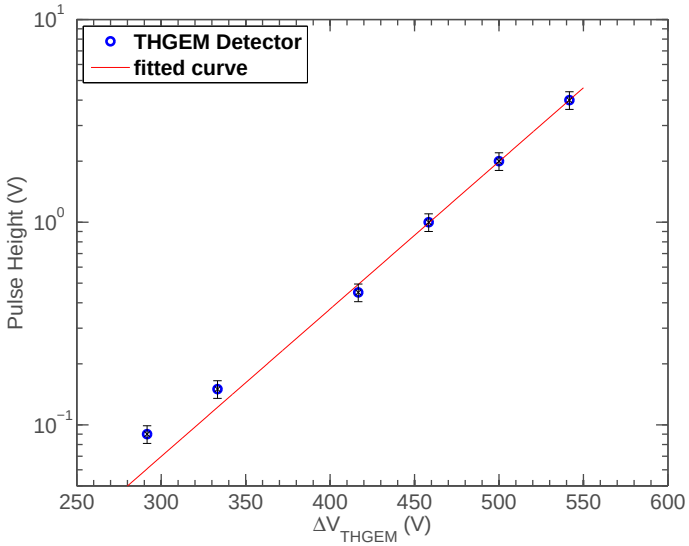

Figure 4.14: The amplitude of the observed pulse from the detector as a function of ΔV_{THGEM}.

Gaussian fit, the alpha peak shows a barely evident tail at high channel numbers of the collected spectrum. A similar but much more evident feature has been reported by De Nardo and Farahmand for an alpha energy deposition spectrum measured with a GEM-based TEPC [89] and by Hanu in the simulated and measured spectra of the alpha particles for a THGEM imaging detector [74]. The high energy tail can be related to the physical dimensions of the collimation hole that allows longer tracks for some alpha particles with respect to those directed along the axis of the sensitive volume.

To investigate the THGEM detector stability, the alpha pulse height spectra were collected every 30 minutes for 60 hours and for each spectrum the peak center was analyzed. Fig. 4.15b shows the time dependence of the peak center. As shown in the figure, in the time interval of 0 and 4 hours, the peak center linearly shifts to 83% of its initial value and then in the following interval of 4 to 10 hours, the peak position drops an additional 5% at a slower non-linear rate. In the interval from 10 to 60 hours, the peak center is quite stable over time and its fluctuation is within ±1%. The same

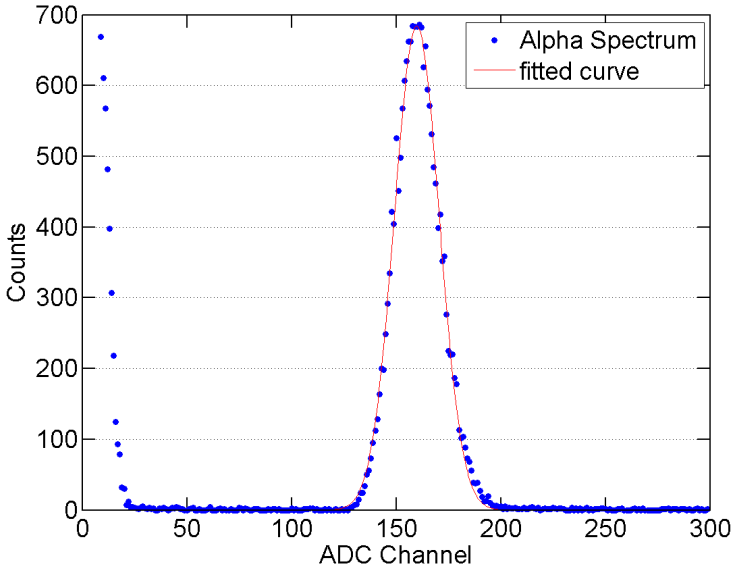

(a)

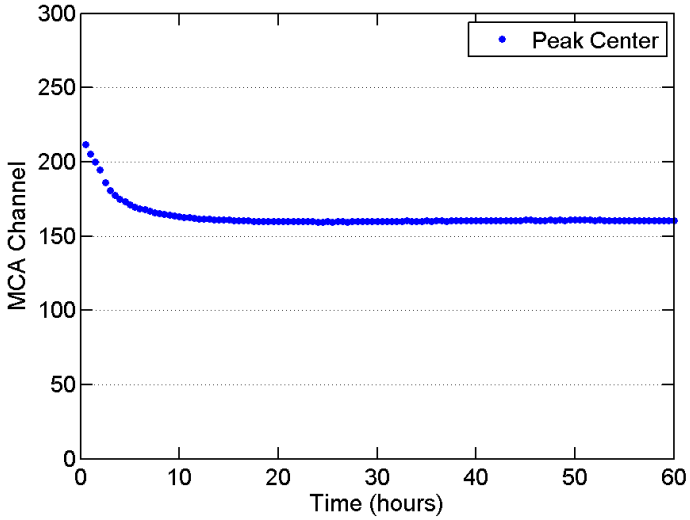

(b)

Figure 4.15: a) The ^{244}Cm source spectrum along with a Gaussian fit; peak center at 160 ± 10. b) The alpha peak position as a function of time.

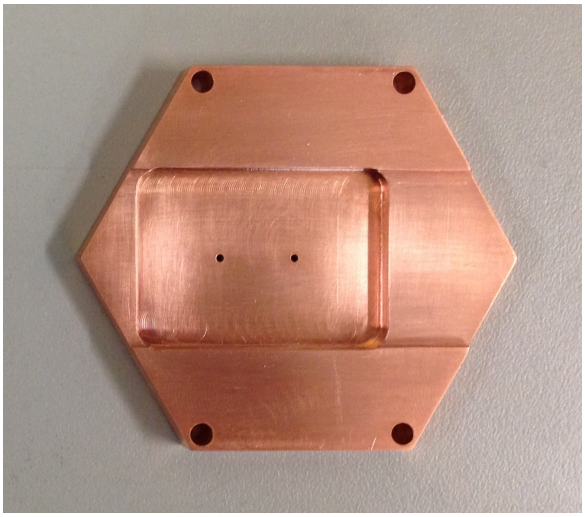

Figure 4.16: A photograph of the alpha source holder consisting of two collimation holes.

pattern was observed for all the THGEM samples used in this study. The peak shift observed in the early time interval implies a drift in the electron multiplication gain over time. This drift was caused by the charge accumulation on THGEM insulator layer, which reduces the effective potential difference across THGEM layer over time [90]. To verify the response consistency over a THGEM surface, the alpha source holder design was adjusted by drilling another collimation hole next to the center of one of the neighboring holes as shown in Figure 4.16. Then in one orientation of the counter the source swings into the position where alpha particles can enter one of the sensitive volumes through either of the collimation holes. This geometry provides the possibility of extracting alpha source signals from two elements in identical conditions simply by rotating the detector. Figure 4.17 shows the pulse height spectra collected from two neighboring elements. The spectra were collected after waiting for an adequate amount of time when the THGEM gain became stable. It can be seen from the figure that the collected spectra from the two neighboring holes are in good agreement.

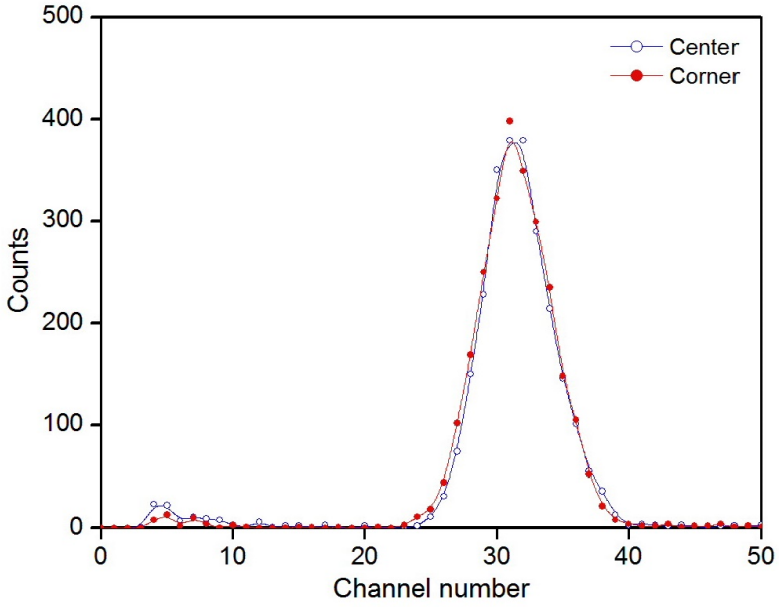

Figure 4.17: The alpha pulse height spectra collected from the center and one of the corner sensitive volumes.

4.6 Conclusion

To overcome the difficulties encountered in the construction procedure of a multi-element TEPC based on the central wire anode, a new type of TEPC based on the THGEM concept is designed and constructed for neutron microdosimetry applications. The prototype multi-element detector layout consists of three alternating layers of Rexolite insulator hexagons. Each layer houses a hexagonal array of cylindrical gas cavity elements with equal heights and diameters. In this design cylindrical geometry was chosen for gas cavities because it matches the THGEM geometry very well and is easy to construct.

The preliminary tests were carried out using a ^{244}Cm alpha source placed inside the prototype detector to examine the signal and stability performance of the detector. Detector stability was observed within several days and the result shows that the THGEM gain drops as a function of time at the beginning due to the charging up

effect and then reaches a stable level.

In the next chapter, the microdosimetric responses of the prototype detector in a mixed neutron-gamma beam is investigated and the resulting spectra are compared with the commercial 2 and 0.5 inch TEPCs.

Chapter 5

Response evaluation of the multi-element THGEM-based TEPC

5.1 Introduction

In the previous chapters, a novel configuration of a multi-element TEPC based on a THGEM was proposed and the prototype detector was assembled. This chapter summarizes initial experiments conducted to evaluate the microdosimetric detector response. Preliminary tests were performed in order for different detector configurations from a single element to the 21 elements. The prototype detector was irradiated with a mixed neutron-gamma field using the McMaster Tandetron accelerator facility. The purpose of the response studies provided in this chapter was to observe the expected features of the event size distributions for given neutron fields, measure the dose rate using the prototype detector and compare the result with that obtained from a standard TEPC in identical irradiation condition and estimate the detector efficiency in counts per μSv. The work presented in this chapter was accepted for publication in Nuclear Instruments and Methods in Physics Research A [82]. The experimental work

was performed by the author of this thesis under the supervision of Dr. Soo Hyun Byun and with guidance of Dr. Bill Prestwich.

5.2 Methods and Materials

5.2.1 Neutron Radiation Source

To produce mixed neutron-gamma radiation fields, the Tandetron tandem accelerator at the McMaster Accelerator Laboratory was used. The Tandetron can accelerate protons up to 2.5 MeV with a maximum current of 1 mA. When energetic protons hit a thick lithium target at the end of the proton beam path, a continuous wide-range spectrum of neutrons is produced via the ^{7}Li(p,n)^{7}Be reaction with a threshold energy of 1.88 MeV. The neutron yield of the lithium target increases with an increase in the proton beam energy [91–93]. At any selected proton beam energy ranging from above the threshold energy to 2.5 MeV, a mixed neutron-gamma field can be generated with a mean neutron energy extending respectively from about 30 keV to above 300 keV [93–95]. Inelastic scattering of protons with the lithium target produces 478 keV photons via ^{7}Li(p, p'γ) reaction that dominate the low LET component of the radiation field. The low LET component of the mixed radiation field also contains 2.2 MeV capture gamma rays originating from the polyethylene moderator in the target assembly via the ^{1}H(n,γ) reaction [61]. The ratio of photon to neutron dose changes with the beam energy and is highest at the threshold of the neutron production reaction and decreases with an increase in the beam energy.

5.2.2 Experimental Setup and Procedure

The Li target assembly is surrounded by an irradiation cavity which is designed to be used for medical and radiobiological studies such as *in vivo* neutron activation analysis [61]. The detailed information on the cavity design and construction can be

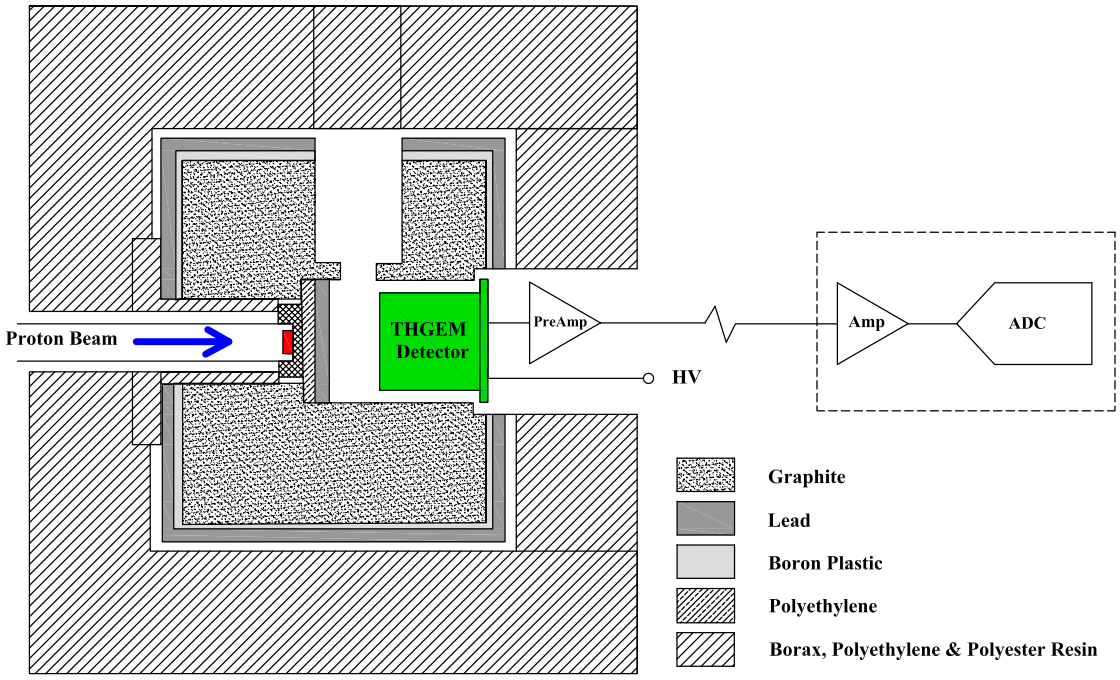

Figure 5.1: The arrangement of the measurement setup with THGEM detector.

found in ref. [96,97]. The detector was placed inside the irradiation cavity centered on the beam path and about 30 cm away from the target. The A-150 layers and THGEMs were biased by using two separate power supply units (Bertan Associates Model 305). The layout of the experimental arrangement is depicted in Fig. 5.1.

To compare the result with the standard data, the commercial 2 inch and 0.5 inch TEPCs (Models LET-2 and LET-1/2, Far West Technology Inc.) were used in this study. The detectors are based on designs originated by Rossi [17]. The FWT LET-1/2 is a spherical cavity in A-150 tissue equivalent plastic with a 1.27 cm (0.5 inch) internal diameter housed in a vacuum tight container. A fine wire anode is placed along the cavity diameter centered in a cylindrical grid of a wire helix to maintain the electric field uniformity along the anode. For the lineal energy calibration, a finely collimated internal ^{244}Cm source introduces alpha particles into the sensitive volume. The FWT LET-2 is a 5.1 cm (2 inch) inner diameter counter consisting of a tissue equivalent sphere made of A-150 plastic and a single wire anode. After data collection, the pulse

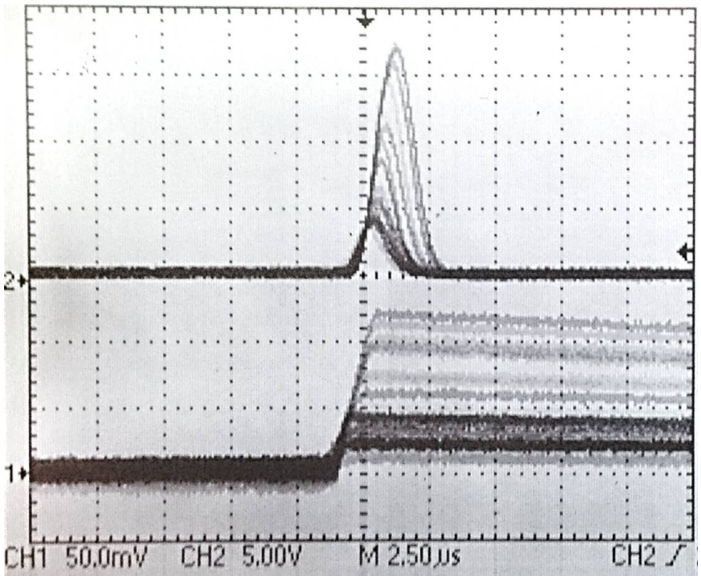

Figure 5.2: The oscilloscope traces of the preamplifier (channel 1) and shaping amplifier (channel 2) signals of the THGEM detector exposed to the neutron-gamma radiation field of the Tandetron accelerator.

height spectra were calibrated in terms of the lineal energy and the dose distributions were derived as outlined in the previous chapters.

5.3 Neutron Response of a Single Sensitive Volume

5.3.1 Gas Multiplication

Following the ^{244}Cm alpha source tests, the response of the prototype multi-element detector to neutrons was comprehensively examined and measured using the McMaster Tandetron ^{7}Li(p,n) neutron source. As the first step of the detector response evaluation in a neutron field, the performance of each gaseous detector element and the consistency of responses between individual detector elements were investigated. To this end, the readout board with 7 circular pads, each collecting the signal from a single detector element, was used so that for a single element desired for testing, its signal could

be readout independently of the other elements (see Figure 4.4d). The oscilloscope capture of the preamplifier and shaping amplifier signals of the THGEM detector is illustrated in Fig.5.2.

Fig. 5.3 shows pulse height spectra of a single sensitive volume collected with different THGEM bias voltages at the proton energy of 2.3 MeV. It can be seen from the figure that the proton drop point (the midpoint of the region with the greatest negative slope corresponding to the maximum energy deposited by recoil proton) increases with the increase of ΔV_{THGEM}. The gas multiplication gain for various THGEM bias voltages was calculated and is displayed in Fig 5.4. As expected, data points follow an exponential trend. The measured data points are extended to the ΔV_{THGEM} of 533 V where the maximum safe gain of 610 was obtained at which no discharge was observed. The THGEM gains were calculated as the ratio of the collected to initial number of electrons using the proton drop point channel numbers and the channel number of a known test pulse amplitude delivered on the preamplifier test input. To estimate the maximum initial number of electrons produced in a sensitive volume, the proton edge lineal energy value of about 115 keV/μm from the measured lineal energy spectrum and the mean energy per ion pair of 28.2 eV [98] were used (see Appendix B for calculation details.)

5.3.2 Lineal Energy Spectrum

For the collected pulse height spectra, the corresponding lineal energy distributions were computed and are presented in Fig. 5.5 along with the 2 inch TEPC response. To create the lineal energy spectrum for each data set, the lineal energy of each detected event was calculated using a proper calibration line and redistributed into equal logarithmic bins with a resolution of 60 bins per decade. For the vertical axis, the number of counts in each logarithmic bin, N(y), was multiplied by the corresponding lineal energy such that the area under the curve between two values of y is proportional to the fraction of the absorbed dose in that region. For the standard TEPC data, the

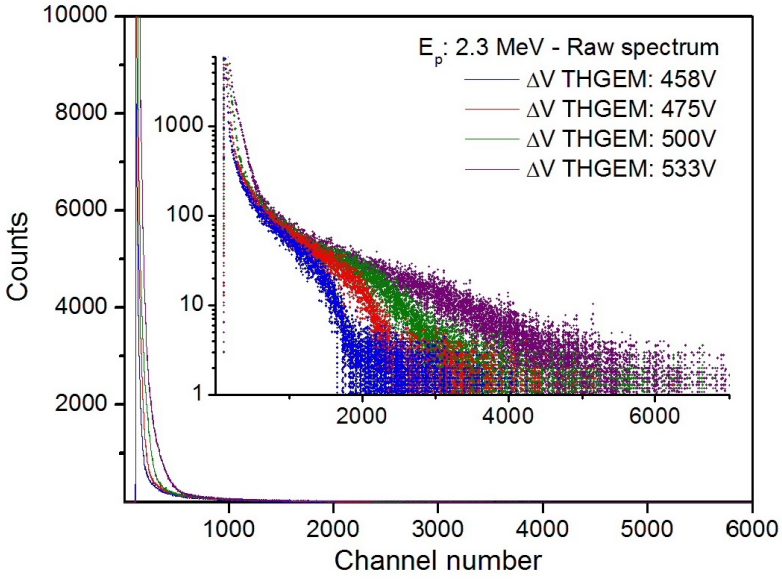

Figure 5.3: The pulse height spectra of a single sensitive volume collected with different THGEM bias voltages at the proton energy of 2.3 MeV.

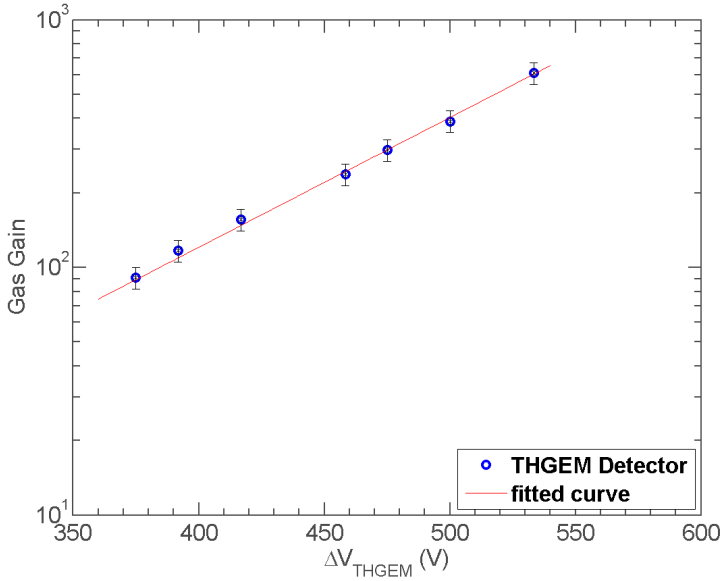

Figure 5.4: The measured THGEM gains as a function of applied voltage across the THGEM for the propane-based tissue equivalent gas at the pressure of 49.1 torr.

lineal energy was calibrated with a built-in ^{244}Cm alpha source. For the prototype detector, which does not have a built-in calibration source, the energy conversion factor has been determined using the proton recoil peak position of the standard TEPC operated in the identical neutron field and a pulser calibration curve. For comparison, all spectra are scaled to the standard TEPC proton recoil peak.

From the figure it is apparent that for the lineal energy region above 10 keV/μm, corresponding to the proton recoil peak, the microdosimetric patterns are consistent between the THGEM detector and the standard TEPC with a comparable energy resolution for the neutron peak. For the lineal energy region below 10 keV/μm which is mainly produced from the contribution of gamma-ray interactions, however, there are discrepancies between patterns. When compared to the standard detector, The THGEM detector exhibits a higher relative dose for the gamma-ray component. For the ΔV_{THGEM} up to 475 V, an increase in the applied voltage across the THGEM improves the minimum detectable lineal energy from about 9 keV/μm at ΔV_{THGEM} of 417 V to 3 keV/μm at ΔV_{THGEM} of 475 V while the spectral patterns of the THGEM detector remain consistent. The deviation from the commercial TEPC pattern increases when ΔV_{THGEM} is increased further above 500 V, which led to a distortion in the spectrum at ΔV_{THGEM} of 533 V. For the lineal energy region above the proton edge, a small tail is evident in the THGEM detector spectrum for all applied voltages. This must have been caused by high electric field values created in THGEM holes with sharp edges which leads to higher local multiplication gains (see chapter 6). To address this minor problem, a better THGEM conditioning method will be sought for in the future.

It was observed that the neutron detection efficiency increases slowly by increasing the applied voltage across the THGEM with the average rate of 1.4% per 10 V. However, as shown in Fig. 5.6, for the last four data points, from ΔV_{THGEM} of 467 V where the lineal energy cut off is well below 10 keV/μm up to the maximum safe voltage of 533 V, the average fluctuation of the proton peak area is about 2% with respect to the average value.

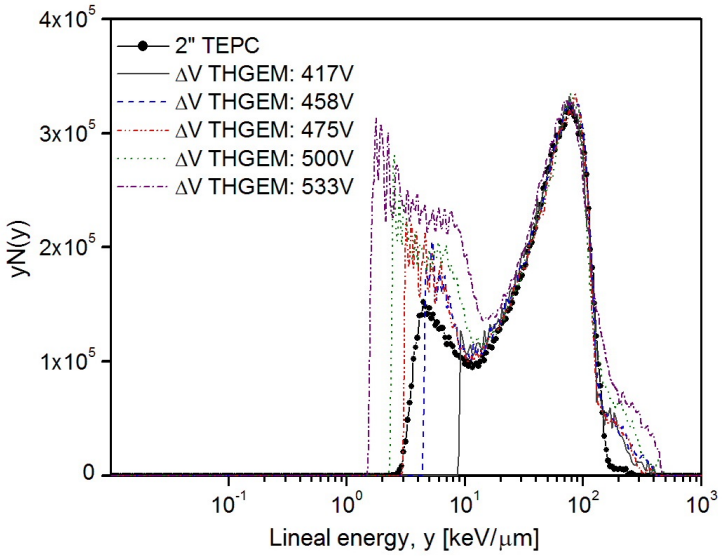

Figure 5.5: Microdosimetric responses of a single sensitive volume for different THGEM bias voltages and 2 inch standard TEPC at the proton energy of 2.3 MeV. For comparison, all spectra are scaled to the standard TEPC proton recoil peak.

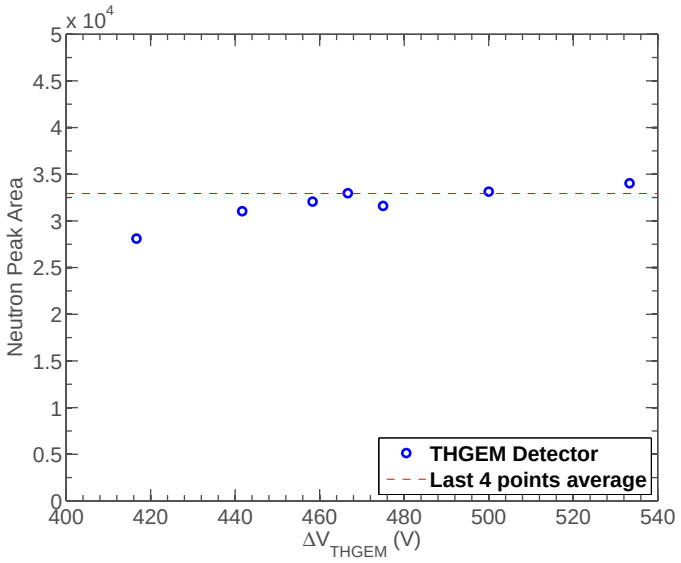

Figure 5.6: The neutron detection efficiency as a function of THGEM bias voltage.

5.3.3 THGEM Gain Stability and Consistency

To evaluate the stability of the THGEM multiplication gain and ensure the reproduciblity of the experimental data in a neutron-gamma radiation field, pulse height spectra of the central sensitive volume are collected every 5 minutes and the proton drop point and count rate were monitored. As shown in Figure 5.7, the proton drop point and count rate decrease during the first 10 minutes and then became stable. The count rate starts with about 1.7 kcps in the first collection time interval and decreases to about 1.4 kcps after 10 minutes and then stays fairly stable for the rest of the data collection intervals. In a similar trend, the proton drop point channel number shifts to 91% of its initial value at the first data set within 10 minutes. A consistent time-dependent gain stability behavior was observed within almost all the THGEMs tested from the same package.

The initial drop in the multiplication gain can be explained by charge up effects. As discussed in section 4.5, some of the ions created inside the THGEM holes during the multiplication will attach to the insulator walls of the THGEM holes. This will decrease the effective electric field across the THGEM and decreases the gain. Depending on the count rate, the THGEM gain becomes stable when a maximum amount of ions has been attached to the insulator and the electric field across the THGEM is constant. To ensure the gas gain stability, all data collections were carried out at least 10 minutes after applying high voltage across the THGEM.

Moreover, with two signal connectors installed on the aluminum casing of the detector, signals from two elements were readout simultaneously. The pulse height spectra collected from two neighbouring gas cavities are shown in Fig. 5.8. While the overall spectral patterns are consistent, the total counts for central element is slightly higher than the corner one. This is expected because of the fact that the neutron field is not uniform and is more concentrated toward the center of the beam.

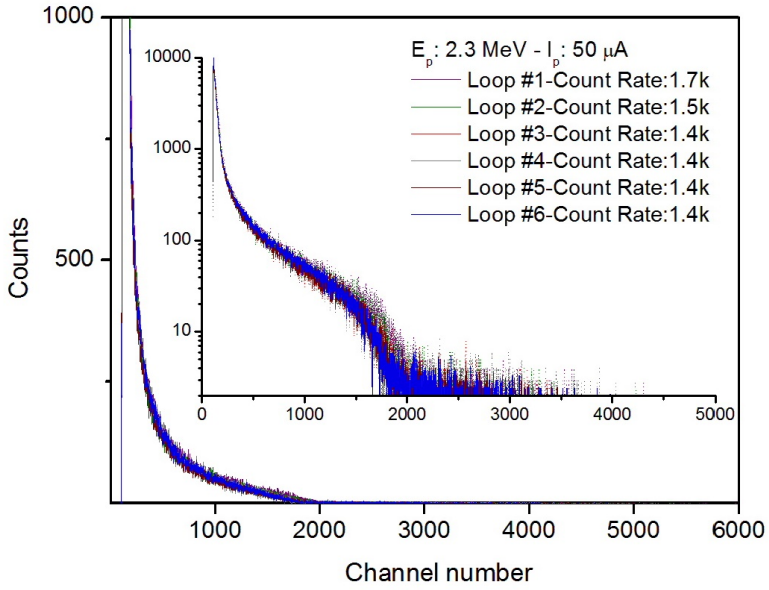

Figure 5.7: The pulse height spectra collected from the central sensitive volume for every 5 minutes at proton energy of 2.3 MeV and 50 μA.

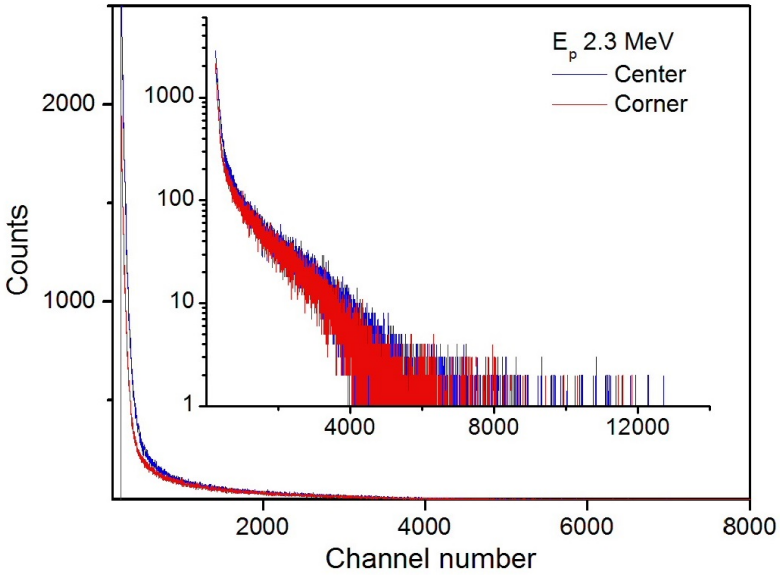

Figure 5.8: The pulse height spectra collected from two neighbouring gas cavities within a layer.

5.4 Neutron Response of the Multi-element THGEM Detector

5.4.1 Detection Efficiency

Experimental measurements for the multi-element configurations were carried out in a sequential way, i.e. starting with seven elements (single layer), then fourteen elements (double layers) and finally ending with twenty one elements (triple layers). This allows investigating a) the consistency of THGEMs' responses between layers and b) the detector counting efficiencies as a function of the number of sensitive volumes. To acquire collectively the response of the individual sensitive volumes of a layer for each detector configuration, the readout board with 7 outputs was replaced with a large collection readout which integrates the response of an entire layer. The arrangement of different layers for each detector configuration is depicted schematically in Figure 5.9. All the THGEMs used in double and triple layers assemblies were tested with the single layer configuration before implementation to ensure the consistency of their responses and electron multiplication gains.

Microdosimetric responses of different detector configurations for the proton energy of 2.3 MeV are presented in Fig. 5.10. For comparison, distributions are normalized by the total proton charge, μC. It is obvious from the figure that the number of detected events increases with the increase of the number of the gaseous cavities. As the number of sub-elements increases from 1 to 7, the area under the proton peak increases by a factor of 6.1 in average among the different sets of measurements. This result is in agreement with our observation of the center and corner sensitive volumes' responses as described in section 4.2. From the single layer to the double and triple layers, the neutron detection efficiency increases in average by a factor of 1.9 and 2.6, respectively. No energy resolution degradation was observed in the proton peak for the single layer assembly with reference to the single element. However, for the triple layer assembly, the width of the proton peak was slightly wider compared to the single element, which

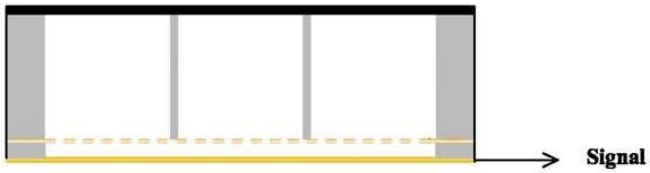

(a) Single layer assembly.

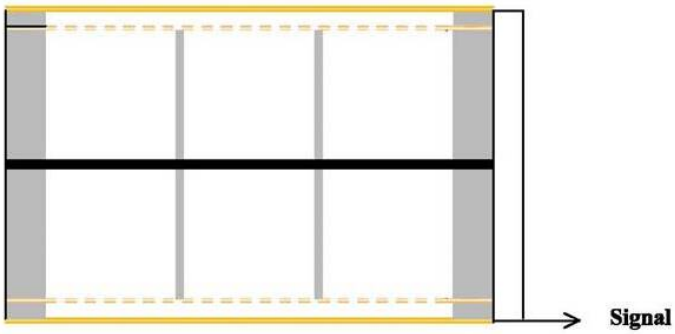

(b) Double layers assembly.

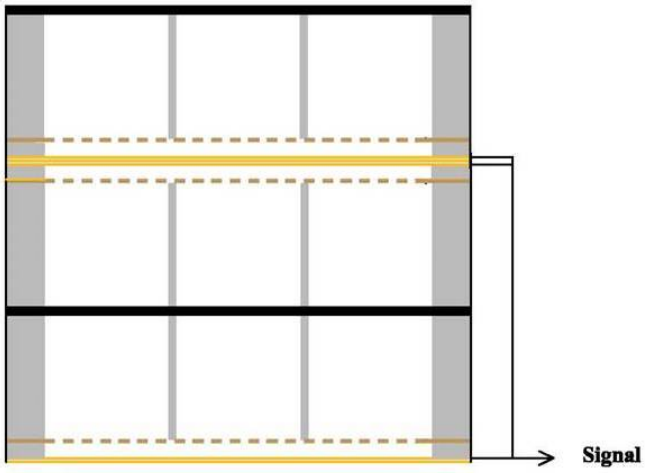

(c) Triple layer assembly.

Figure 5.9: Schematic diagrams of the arrangement of different layers for each detector configuration.

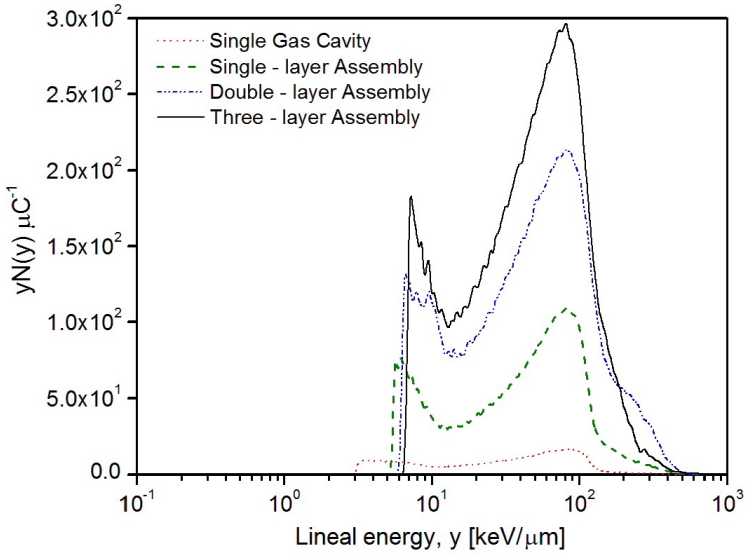

Figure 5.10: Microdosimetric responses of a single sensitive volume, single layer, double and three-layer assemblies collected at proton energy of 2.3 MeV.

was caused by gain variation of the THGEMs. By comparing the area under the recoil proton peak, the prototype multi-element THGEM detector improved the neutron detection efficiency by a factor of 3.0 with reference to the standard spherical 2 inch TEPC. This is in agreement with the simulation result presented in ref. [73].

From the figure, it is notable that the cut off lineal energy of the single element is about 3 keV/μm where both gamma and neutron components are detectable. For the same applied voltages, this value shifts to about 5 and 6 keV/μm for 7 and 14 elements, respectively. This stems from the fact that the detector capacitance increases with the increase of the number of gas elements, which leads to worse signal to noise ratios. The cut off for the 21 elements (triple layers) increases to about 6.5 keV/μm where the gamma-ray component is almost not detectable. The cut off lineal energy can be lowered down to 5 keV/μm for the triple layer assembly by pushing ΔV_{THGEM} very slowly to the maximum safe voltage of 533 V. In a case that more gamma-ray component spectral information is required, the minimum detectable lineal energy can be improved by increasing the multiplication gain through using THGEMs with more

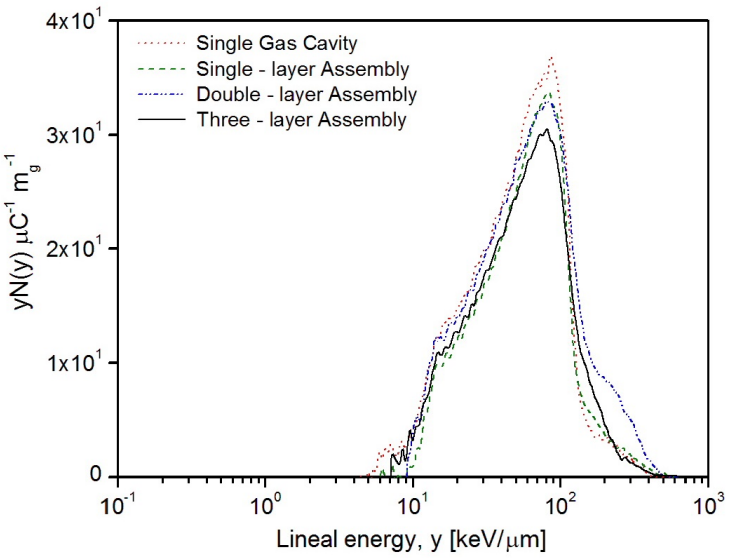

Figure 5.11: Microdosimetric responses of the prototype detector configurations normalized by the mass of the counting volume gas and also by the total proton charge.

round and soft hole edges which allow for higher bias voltages, or by employing two THGEMs in each layer.

To validate the neutron responses of the different detector configurations, the gamma-ray components were subtracted from the original spectra using a ^{137}Cs spectrum fitted to each spectrum. Then, all spectra are normalized by the total mass of the gas in the sensitive volumes, m_g. The result is shown in Fig. 5.11. It can be seen from the figure that the spectrum patterns are quite consistent for all detector configurations. Since the area under each plot is proportional to the measured neutron dose, it can be concluded that all detector configurations are capable of measuring neutron dose rates reliably. From a single element to 7 elements, the measured dose rate decreases as expected. It increases from 7 elements to 14 elements as the second layer is a little closer to the target. Finally, a slight decrease was observed for 21 elements with respect to 14 elements. This may have been caused by the neutron scattering effect within the layers, which leads to a slightly lower neutron fluence. The average discrepancy in measured neutron absorbed dose with reference to the standard TEPC was 8%.

Table 5.1: Activation and decay data for copper.

Nuclide	Fraction	$\sigma(n,\gamma)$	Activated nuclide	$t_{1/2}$	Emitted radiation
^{63}Cu	69.1%	4.3 b	^{64}Cu	12.7 h	β^-, β^+, γ
^{65}Cu	30.9%	2.1 b	^{66}Cu	5.1 min	β^-, γ

5.4.2 Measured Absorbed Dose

In order to explore the prototype multi-element THGEM detector response versus the incident beam energy, pulse height spectra were collected for different proton beam energies ranging from 1.9 to 2.3 MeV. Figure 5.12 and Figure 5.13b display examples of the collected pulse height spectra and the corresponding lineal energy distributions for the proton energy of 2.1 and 2.3 MeV, respectively. The yN(y) distributions are plotted along with the 2 inch TEPC spectra collected at the same proton energy. The microdosimetric spectra are normalized by the total proton charge and mass of the gas in the sensitive volume.

From the figures it can be concluded that the patterns of the microdosimetric spectra show the same features with variation in neutron energy as the standard 2 inch TEPC. However, the low LET component of the prototype detector shows a noticeable deviation from the standard detector for all proton energies. This can be partly because of the high copper content of the THGEM detector structure and therefore activation of the copper layers of the THGEMs by neutrons. Natural copper consists of two isotopes of ^{65}Cu (30.9%) and ^{63}Cu (69.1%). Both isotopes are being activated by neutrons via ^{65}Cu(n, γ)^{66}Cu and ^{63}Cu(n, γ)^{64}Cu with emitted gamma energy of 1.04 and 1.35 MeV, respectively, along with 0.511 MeV photons from the positron annihilation. More information on the neutron interactions with Cu can be found in Table 5.1.

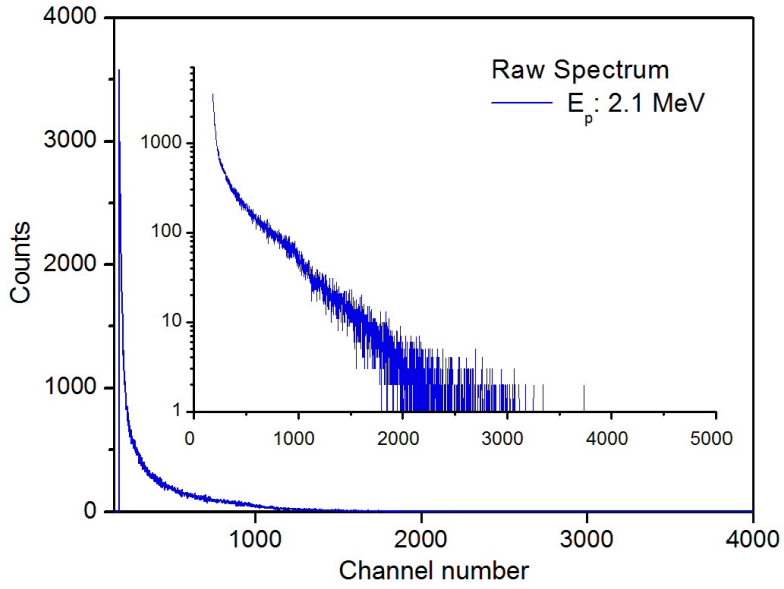

(a)

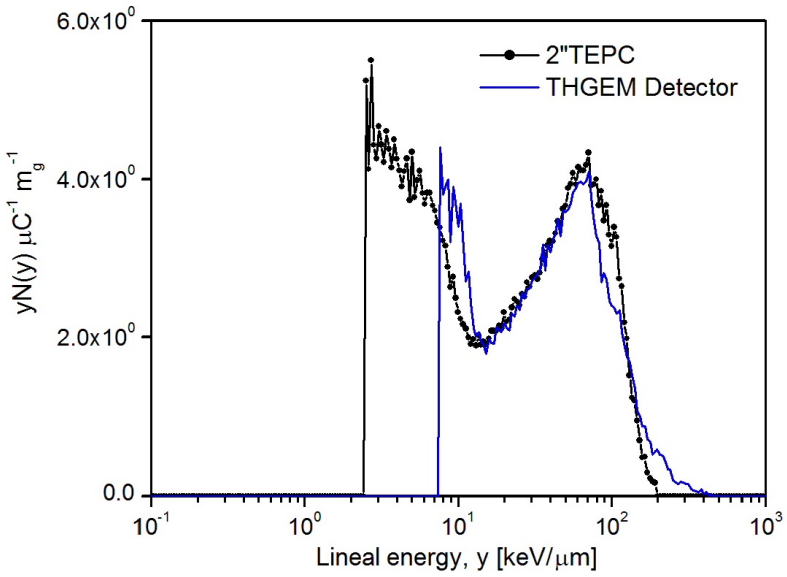

(b)

Figure 5.12: a) The collected pulse height spectrum using the prototype multi-element THGEM detector at the proton energy of 2.1 MeV. b) The corresponding lineal energy spectrum after calibration along with the standard 2 inch TEPC spectrum. The yN(y)distributions are normalized by the total proton charge and mass of the gas in the sensitive volume.

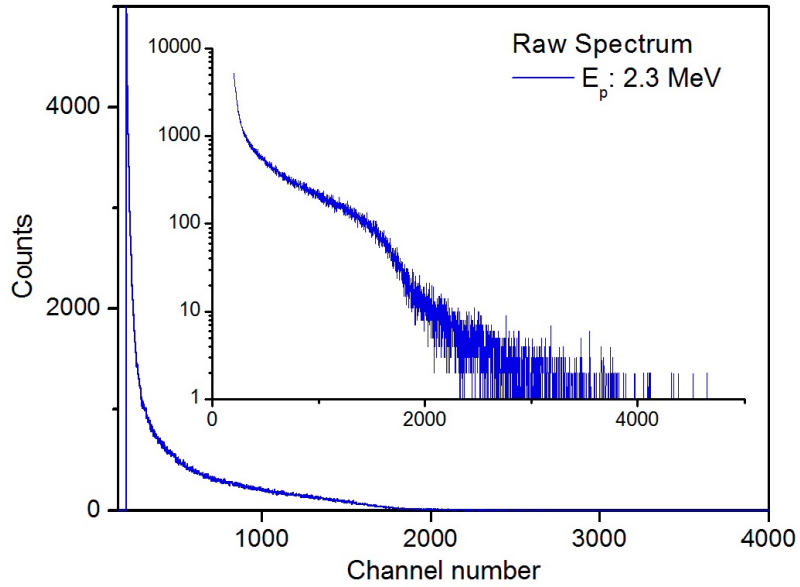

(a)

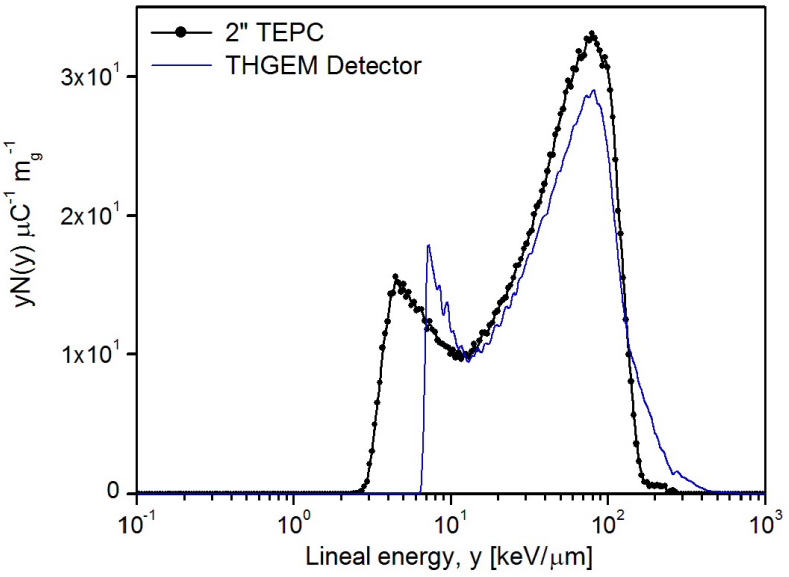

(b)

Figure 5.13: a) The collected pulse height spectrum using the prototype multi-element THGEM detector at the proton energy of 2.3 MeV. b) The corresponding lineal energy spectrum after calibration along with the standard 2 inch TEPC spectrum. The yN(y)distributions are normalized by the total proton charge and mass of the gas in the sensitive volume.

Table 5.2: The measured neutron absorbed dose rates for the prototype detector and standard TEPCs.

	Proton Energy (MeV)				
	1.9	2.0	2.1	2.2	2.3
0.5 inch TEPC	2.21E-07	9.49E-07	2.62E-06	8.53E-06	1.77E-05
2 inch TEPC	1.99E-07	7.48E-07	2.59E-06	8.03E-06	1.80E-05
Multi-element THGEM Detector	1.83E-07	7.04E-07	2.17E-06	7.82E-06	1.60E-05

Values are in $mGy\ \mu A^{-1}\ min^{-1}$ $\pm 10\%$

To calculate the neutron absorbed dose from each spectrum, the gamma-ray component was fitted with a standard gamma-ray microdosimetric spectrum from ^{137}Cs and subtracted from the entire spectrum. The measured neutron absorbed dose rates for the prototype multi-element THGEM detector and the standard TEPCs are summarized in Table 5.2 for the proton energy range of 1.9 to 2.3 MeV. For comparison, the results are plotted in Figure 5.14 and all measurement results are quoted in $mGy/\mu A^{-1}min^{-1}$ for convenience. As expected, the dose rate increases with increasing the proton beam energy due to increase in neutron yield in the lithium target.

The measured absorbed dose rates with the standard detectors were not conducted at the same day with the THGEM detector. Therefore, to carry out a more reliable comparison the reported dose rate values for the standard detectors are averaged between three sets of different measurements in different dates conducted under identical experimental conditions at a given proton energy.

To take a closer look at the discrepancies in measured neutron dose rates with the reference detectors, the ratios of the absorbed dose measured with the prototype multi-element THGEM detector to that of 2 and 0.5 inch TEPCs are calculated for different proton beam energies and depicted in Figure 5.15. As illustrated, the estimated dose rates with the prototype detector is consistently smaller than that of standard detectors with the maximum discrepancies of 26% and 15% for 0.5 and 2 inch TEPCs, respectively.

It should be noticed that the measured absorbed dose rate values obtained with

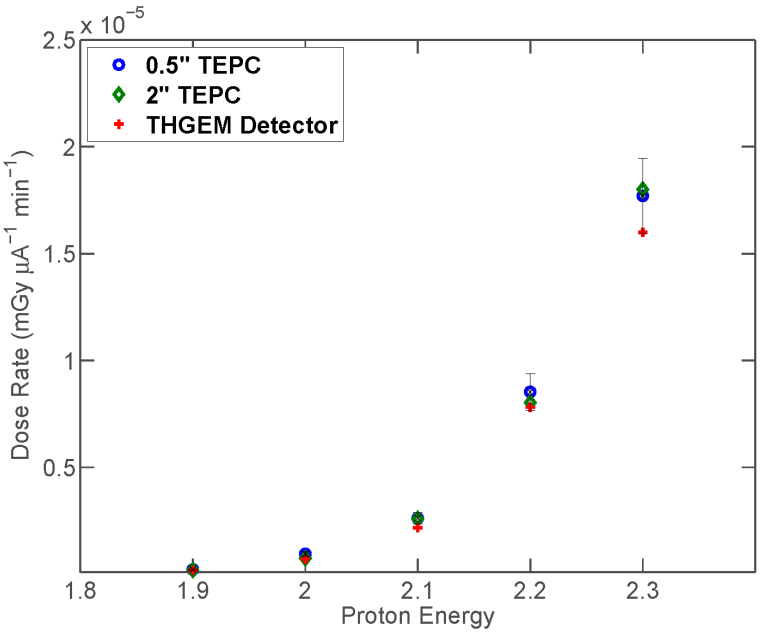

Figure 5.14: Measured dose rates obtained from the prototype multi-element THGEM detector, 0.5 and 2 inch standard TEPCs at different proton energies.

2 inch TEPC are lower compared to 0.5 inch TEPC for all energies, excluding the proton energy of 2.3 MeV. It was expected as the proton beam is not collimated and is more concentrated towards the center of the cavity and this was confirmed with our measurements obtained by the center and corner sensitive volumes of the THGEM detector (see subsection 5.3.3). The deviation of the measured absorbed dose at 2.3 MeV from this trend might be attributed to the uncertainties in beam parameters such as the proton beam energy and beam current and uncertainties due to the lineal energy calibration or gamma component elimination.

The systematic underestimation in the measured absorbed dose by the prototype detector can be partly related to the geometrical differences of the detector structure compared to the standard ones and also the scattering of the neutron beam within the different layers of the multi-element THGEM detector that can lead to a lower fluence to dose conversion coefficient.

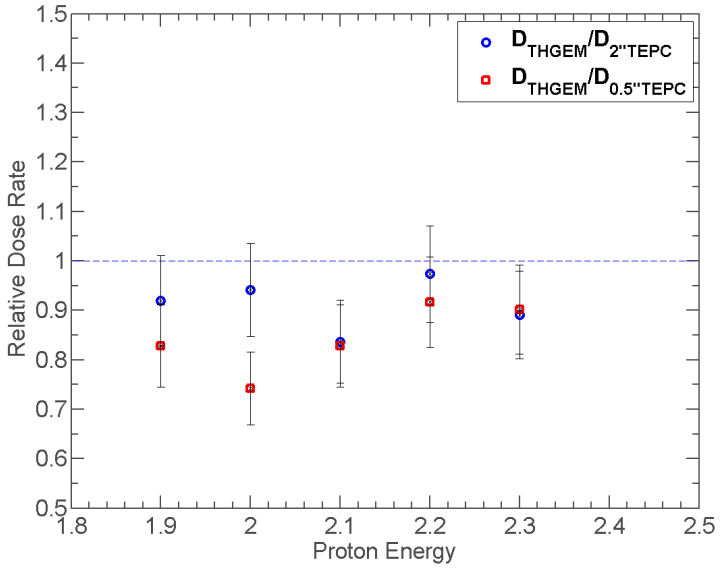

Figure 5.15: Ratios of the measured dose rates obtained from the prototype multi-element THGEM detector to that of 2 and 0.5 inch standard TEPCs at different proton energies.

5.4.3 Detector Response in Different Proton Currents

Figure 5.16 shows the lineal energy distributions collected by the prototype detector for different proton currents. These measurements were conducted to determine the consistency of the microdosimetric patterns in experimental conditions when experiments require varying count rates at a given proton energy. The yN(y) distributions are normalized to the total proton charge and are corrected for the dead time. The pulse height spectra were collected at the proton energy of 2.3 MeV and different proton beam current ranging fron 20 to 200 μA. The THGEM bias voltage ΔV_{THGEM} was set at 516 V. It is obvious from the figure that the spectra compare well with each other in the applied proton current range up to 100 μA. For the proton current of 200 μA, several sets of discharges were observed during the data collection that corrupted the amplitude measurements and they appeared as spikes in the data set. By lowering the proton current it was observed that the multiplication gain was reduced significantly and the detector wasn't functioning properly. This measurement was

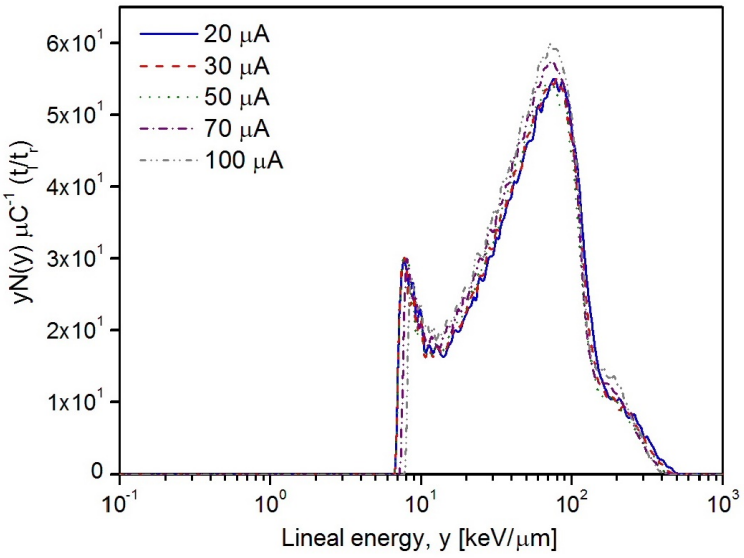

Figure 5.16: The prototype THGEM detector response for different proton current at Ep: 2.3 MeV.

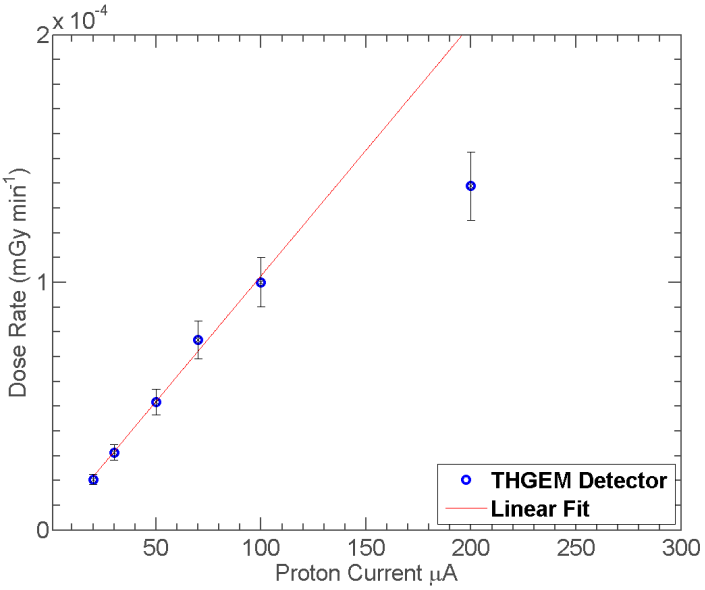

Figure 5.17: Neutron dose rate as a function of proton beam current at the proton energy of 2.3 MeV.

repeated with a new set of THGEMs and a similar outcome was observed for proton currents above 200 μA. Based on these observations, it was concluded that when the prototype detector is exposed to high proton beam currents leading to release of a large amount of charge in the sensitive volume, a breakdown of the gas may occur. The linearity of the absorbed dose rate versus the proton beam current is illustrated in Figure 5.17.

5.5 Conclusion

Following our extensive Geant4 simulation study [73], an advanced prototype multi-element detector based on the THGEM technology was designed and successfully developed to enhance neutron detection efficiency of the tissue equivalent neutron dosemeters. The detector tests were carried out in a mixed neutron-gamma radiation field of the McMaster Tandetron accelerator lab facility and the overall performance of the prototype detector was evaluated with reference to the standard wire-based TEPCs. Compared to standard 2 inch TEPC response that has an overall size comparable to the THGEM detector, the detector gave a consistent microdosimetric response. Moreover, it was found that the neutron detection efficiency has been improved by a factor of 3.0 from the benchmark measurements between the THGEM multi-element detector and the 2 inch TEPC.

Chapter 6

THGEMs: From Production to Use

6.1 Introduction

As described before, the THGEM geometry is derived from the standard GEM design, with its various dimensions being enlarged by a factor of about 10. The larger hole diameter of THGEMs compared to the standard GEM allows a different and probably less delicate production procedure. THGEMs can be economically fabricated using standard PCB techniques out of a copper clad insulator substrate. In most applications, FR4 (Flame Retardant 4) is used as insulator layer. FR4 is a composite of a resin epoxy reinforced with a woven fiberglass material and a yellowish color. The THGEM holes are created by mechanically drilling the fiberglass by a milling tool mounted on a Computer Numerical Control (CNC) machine. The quality of the hole shape depends on the frequency of the tool replacement and the precision of the CNC machine.

The first THGEM developed by our group was fabricated manually in our lab by drilling 32 micro holes in a FR4 plate using a homemade drilling machine [54]. This method, however, seems not efficient for production of THGEMs with large active area. The THGEMs used by Hanu [74], with outer dimensions of 42×42 mm^2, were fabricated industrially and ordered online from MyroPCB Inc. (www.myropcb.com). Orchard and Hanu both studied responses of THGEMs of different hole dimensions.

However, all studied THGEM samples feature a same characteristic of having a chemically etched rim (about 0.1 mm) around each hole. This geometry is recommended for reducing the probability of gas breakdowns and achieving higher permissible voltages and hence higher electron amplification gain [67].

To develop the THGEMs for this study, I adopted the geometrical parameters recommended by the previous investigations of our group and applied a slight adjustment in the THGEM design by having the THGEM holes arranged in a triangular pattern, as seen in the standard GEM, instead of a square pattern used by Orchard and Hanu. The first package of the THGEMs used in this study was also ordered from MyroPCB Inc.. However the THGEMs were of a very poor quality causing unexpected difficulties in experimental measurements, as discussed in the following sections. The rest of the THGEMs were produced at Milplex Circuit Inc. (www.milplexcircuit.com) where some further adjustment in the THGEM design and the cleaning protocol applied after drilling was curried out.

This chapter summarizes the steps taken to develop the THGEMs that were used in the prototype multi-element detector for the measurement results presented and discussed in the previous chapter.

6.2 Manufacturing and Description

A summary of the extensive studies performed regarding the influence of the THGEM geometrical parameters variations and the gas mixtures employed on the THGEM performance is reported in ref. [67, 69, 83, 99, 100]. Shalem et al. [67, 69] conducted a broad systematic study to optimize the THGEM geometrical parameters for different applications at atmospheric and low gas pressures. Their THGEM production procedure consists of the standard etching using photolithographic masks. In this method a photoresistive layer is applied to the Cu-clad fiberglass plate before drilling. After drilling the holes, THGEMs are dipped in acid. Acid attacks the uncovered copper

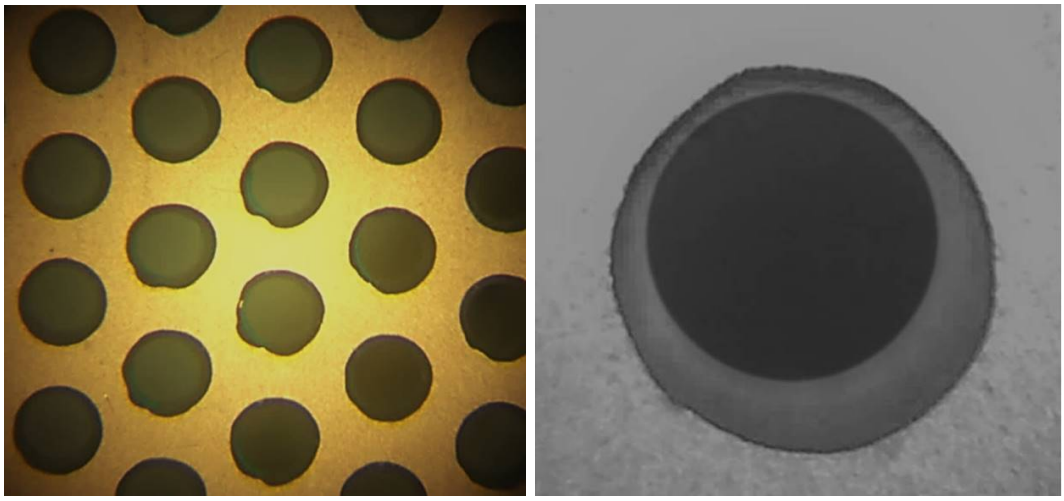

(a) (b)

Figure 6.1: a) THGEMs with rim manufactured by MyroPCB Inc.. b) A microscopic view of a THGEM hole showing an off-center rim.

surface at the hole edges created by drilling. This leads to creation of a clearance in the copper layer around the hole. Then the photoresistive layer is stripped away. They noted that a 0.1 mm clearance around the drilled holes can improve the maximum gain by up to an order of magnitude. They also stressed the importance of having the etched and drilled patterns precisely centered. It was observed that the electrodes in which the etched pattern was largely displaced from the drilled one did not function properly [67].

Having this in mind, the first set of THGEMs used in our study was ordered from MyroPCB Inc. Each THGEM houses a triangular pattern of about 4000 holes spaced by 0.8 mm with a hole diameter of 0.4 mm and a 0.1 mm clearance around each hole. Figure 6.1a shows a microscopic view of a THGEM sample produced at MyroPCB. From visual observation of THGEMs under microscope, it is apparent that THGEMs suffer severely from irregular hole shapes and sharp edges. Also as illustrated in Figure 6.1b, some holes failed in having a centered rim. Given the fact that the THGEM hole geometry affects directly the field inside the hole and hence the multiplication gain, these variations can change the THGEM electron multiplication gain locally and

lead to malfunctioning of the proportional counter, i.e. non-uniformity in the electron amplification. Also, having sharp edges and eccentric hole-rim pattern makes the THGEM more open to spark induced breakdowns that limits the highest achievable gain. Considering that the gain enhancement was our original motivation for adding a rim around each hole, in further THGEM development we decided to remove the rim in the THGEM design.

To eliminate irregular hole borders and defects related to the drilling and production procedure and accomplish perfect round hole edges, an innovative approach was used at CERN for production of the large area THGEMs (300×300 cm^2). The details of the results concerning the production procedure, in particular the cleaning and polishing stages, and related tests are described by Alexeev et al. [86]. The geometrical parameters of the THGEMs studied are a hole diameter of 0.4 mm pitched by 0.8 mm with different thicknesses and without an etched rim. A microscopic photograph of a THGEM sample before treatment is shown in Figure 6.2a. The applied THGEM treatment procedure is based on a combination of a mechanical polishing and a mild chemical processes. After drilling the holes, the copper surface is polished with pumice powder as displayed in Figure 6.2b followed by high pressure water cleaning to remove the pumice residuals. Then, THGEMs were placed in an ultrasonic bath at 50°C for about 1 hr in a very mild etching solution to smooth the hole borders and remove copper debris that may have been generated during polishing process. Finally, the THGEMs are washed using demineralized water followed by 24 hours drying at 180°C to totally remove all moisture. A microscopic photograph of the THGEMs after treatment is shown in the Figure 6.2c.

Taking inspiration from the exceptional result delivered by the CERN treatment procedure, a similar approach was implemented for development of the THGEM prototypes in this work. It is obvious that the aforementioned procedure requires developing a custom production process and the related tools. Therefore, to have THGEMs that meet the requirements to be used as the multiplying element in a

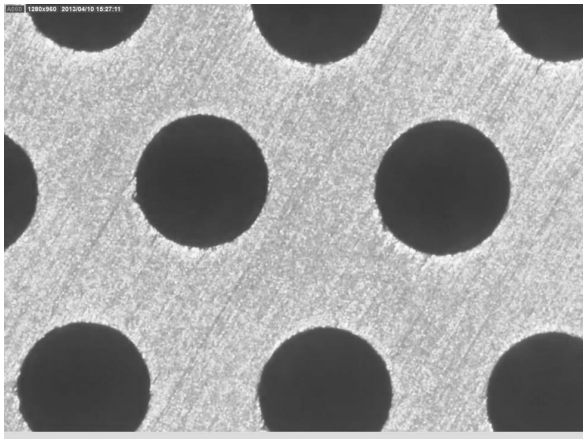

(a)

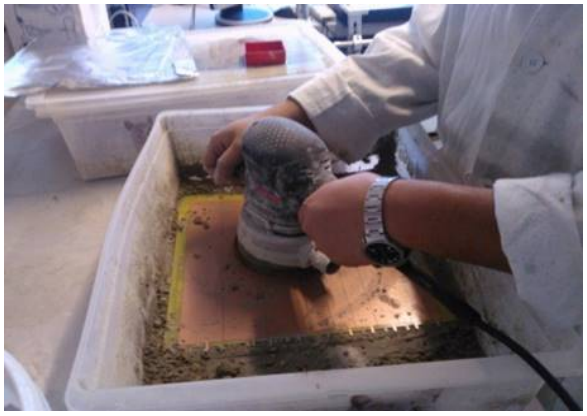

(b)

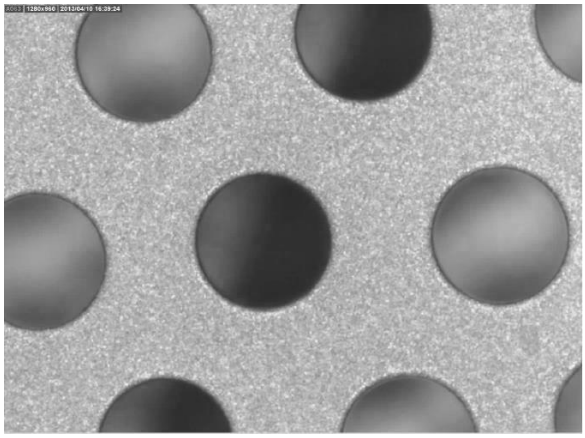

(c)

Figure 6.2: a) A microscopic photograph of a THGEM before treatment. b) The polishing process of the THGEM with pumice powder. c) A microscopic photograph of the same THGEM after the treatment [86].

gaseous THGEM detector, we returned into industry for help one more time. The required polishing and cleaning stages as proposed by CERN were discussed with an engineering team at Milplex Circuit Inc.. After initial negotiations, the team suggested that they can deliver similar result; however, the development procedure needs to be adapted based on the available equipment at the manufacturer. This simply means that the THGEM production procedure has to be adapted and optimized again through several trials. Therefore, three different packages were ordered one by one. Each time based on the visual inspection of the THGEMs via microscope and primary test results, I asked for some specific corrections on the treatment procedure. The treatment and conditioning procedures implemented in this study for development of the final THGEM package consist of the following steps:

1. Mechanical drilling.
2. Brushing using conveyorized brushing machine (Deburr) equipped with 500 grit high speed rotating brushes.
3. Global chemical etching
4. Polishing with pumice stone using a conveyorized jet pumice machine that pumps slurry of pumice and water at high pressure on the PCB.
5. Micro etching using a conveyorized chemical spray system with 10% nitric acid at 110 °F.
6. Rinsing with the demineralised water followed by a baking cycle to dry the THGEMs.
7. Packing the THGEMs in vacuum bags.

The THGEM cost varies depending on the number of holes to be drilled, the number of mills used and the post production cleaning procedure. Each THGEM produced at Milplex Circuit Inc. cost us in average about $20.

A summary of the geometrical parameters of the THGEMs studied in this work is listed in Table 6.1. The following sections describe the preliminary tests and the experimental setup used for initial performance evaluation of the prototype THGEMs in neutron-gamma radiation fields.

Table 6.1: A summary of the geometrical parameters of the THGEMs studied in this work (values are in mm).

THGEM	Package #	Drilled hole Diam.	Rim	Pitch	Thickness
MyroPCB Inc.	1	0.4	0.1	0.8	0.4
Milplex Circuit Inc.	1,2 and 3	0.4	-	0.8	0.4

6.3 Detector Assembly and Experimental Setup

All THGEMs were individually inspected and tested before mounting. To prevent organic contamination, gloves had to be worn during tests and assembling. For storage and later use, after visual inspection, cleaning and primary tests, each THGEM was placed in a clean bag inside a vacuum container to avoid exposure to dust and moisture. Before using each THGEM within the detector for experimental measurements, an inspection was done by eye, followed by a more extensive survey performed under a microscope for both sides of the THGEM to check the uniformity of the hole diameter and search for irregularities and sharp edges and other possible defects. The presence of defects was recorded and if they were only a few, the THGEM was accepted for further tests.

Before mounting, the THGEM was blown using an open flow of high pressure nitrogen to remove dust and other residual particles. Then the THGEM was used in a single layer detector assembly to be tested in neutron-gamma fields as outlined in the previous chapters. The high voltage connections, insulation and potential difference across different layers were controlled regularly at different steps during the construction. To avoid concentration and deposition of vapor, especially during winter, the assembly and aluminum chamber were heated slightly using a heat gun before and after closing the aluminum chamber cap.

All primary THGEM tests in neutron radiation fields were carried out for the detector configuration consisting of the following elements unless otherwise stated:

- a 1 mm thick A-150 as the drift cathode.

- a layer of a Rexolite hexagon housing seven sensitive volumes with heights and diameters of 17 mm.
- a THGEM and a charge-collecting electrode with seven circular pads of 17 mm diameter and a collection gap of 1 mm.

6.4 Performance Evaluation of THGEMs in Neutron-Gamma Fields

6.4.1 THGEMs with Rim/ Produced at MyroPCB

Despite the fact that the MyroPCB THGEMs appearance under the microscope was disappointing, their performance was evaluated in neutron-gamma radiation field to gain some insight regarding treatment and conditioning protocol required to deliver better shaped holes. Figure 6.3a shows a sample pulse height spectrum collected with a proton beam energy of 2.3 MeV and a proton current of 50 μA, for the THGEM bias voltage ΔV_{THGEM} of 590 V and collection time of 10 min. It can be seen from the figure that the energy deposition events are extended above the recoil proton drop point in channel number of about 4 k up to 12 k.

Figure 6.3b shows the corresponding lineal energy distribution after calibration. The collected data are calibrated in such a way that the main peak of the spectrum matches the proton peak of the collected spectrum by the standard 0.5 inch TEPC. In order to compare the shapes of the spectra, the THGEM spectrum is normalized to the standard TEPC spectrum.

It is apparent from the figure that the extended events after the proton drop point in the pulse height spectrum give rise to a second peak in the lineal energy spectrum. Except for the second peak, the general pattern of the lineal energy spectrum collected with the THGEM detector is in a very good agreement with that of the standard detector.

As discussed earlier, the event sizes that are laid above the proton drop point can be tracked back to high electric field values created in THGEM holes that result from sharp edges, irregularities and eccentric hole-rim pattern observed in the THGEM structure leading to multiple amplification gains.

A comparison between the lineal energy spectra collected by the THGEM detector and the standard 0.5 inch TEPC after normalization to the proton charge and mass of the gas is shown in Figure 6.3c. The fact that the THGEM lineal energy distribution is lower compare to the standard one for all the lineal energy values up to the proton edge supports the idea that some event sizes are affected by non-uniformity in the amplification gain. It was concluded that these missing events must have experienced high field values created at sharp edges and hence landed on high lineal energy values above the proton edge. Similar results were obtained for the other THGEM samples tested from this package for different proton beam energies.

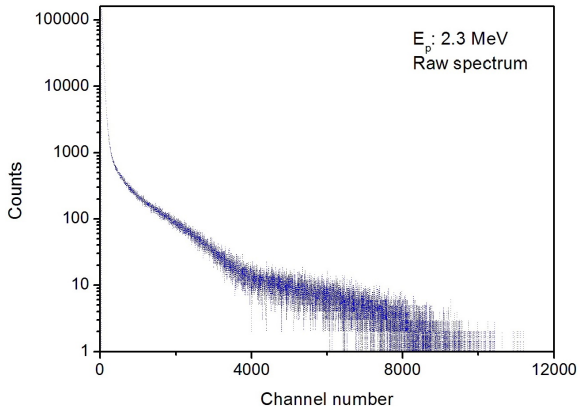

(a)

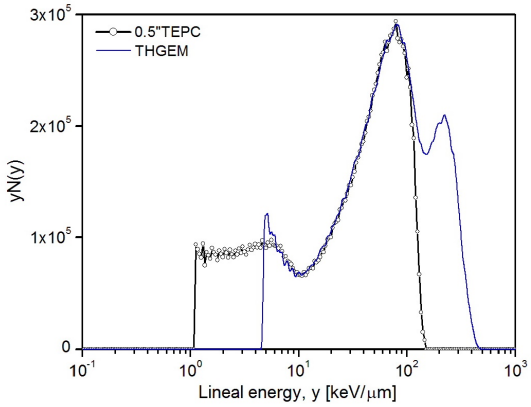

(b)

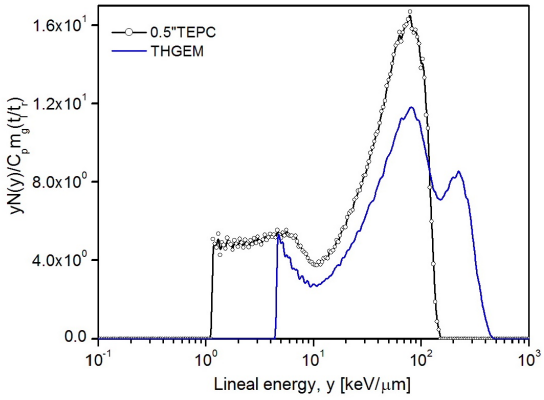

(c)

Figure 6.3: a) A sample pulse height spectrum collected using a THGEM with rim fabricated at MyroPCB Inc.. b) The corresponding lineal energy spectrum normalized to the standard TEPC spectrum. c) A comparison between the collected spectra with the THGEM detector and 0.5" TEPC. The spectra are normalized to the proton charge and mass of the gas.

6.4.2 THGEMs without Rim/ Produced at Milplex Circuit

6.4.2.1 Package Number One

Figure 6.4a displays the pulse height distribution recorded from the THGEM detector for a THGEM sample without rim from the package number one when the detector was exposed to the 2.3 MeV proton beam. Compared to the pulse height distribution in Figure 6.3a, the proton drop point is more evident (about channel number 4 k) and the number of event sizes that are positioned above the proton edge is relatively smaller. This can be seen in N(y) distributions in Figure 6.4b. The figure illustrates the distribution of the number of events versus lineal energy for the collected data using the THGEM detector for THGEMs with and without rim and the 2 inch TEPC detector. When comparing the area under the curves for the lineal energy region above the proton edge, the number of events is higher by a factor of about 2.14 for the Myro THGEM with rim compared to the Milplex THGEM without rim.

The THGEM detector response was tested for several THGEM samples that were selected after visual inspection from this package. Figure 6.4c displays the three spectra obtained with three different THGEMs and the standard 2 inch TEPC collected using the same beam parameters. All the spectra are obtained with the ΔV_{THGEM} of 458 V. It is evident from the figure that the microdosimetric distribution patterns are consistent for all samples. Compared to MyroPCB THGEMs that have a rim around the holes, a significant improvement is observed in the distribution pattern above the proton edge for THGEMs without Rim. However, with respect to the 2 inch standard TEPC, the lineal energy curve still extends to higher values.

A visual inspection of the THGEMs without rim via microscope reveals that with the new implemented fabrication and treatment procedure the irregular hole borders, sharp edges and defects related to the production procedure seen in THGEMs with rims are lessened a lot and THGEMs with an overall better quality are achieved. However, the quality of holes cannot meet the required criteria as some holes still suffer from copper debris generated during the drilling process shown in Figure 6.5a. The debris is not

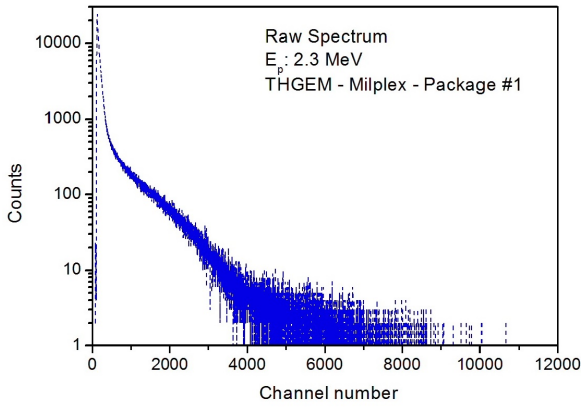

(a)

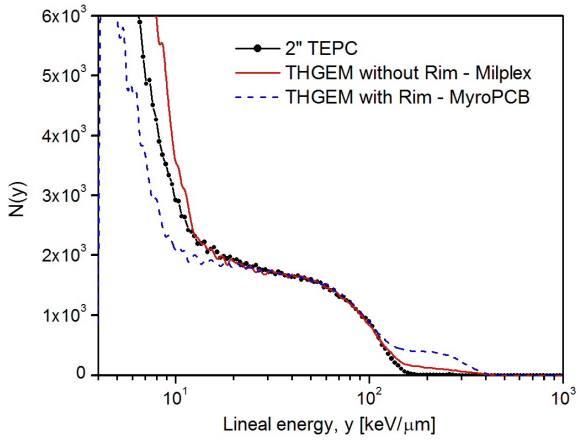

(b)

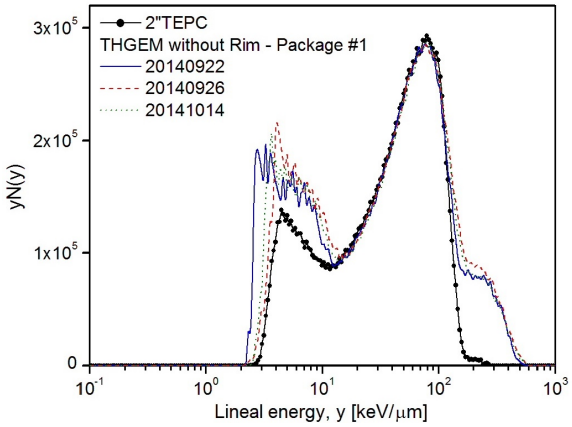

(c)

Figure 6.4: a) Pulse height distribution recorded from a THGEM sample without rim. b) Distribution of number of events versus lineal energy for the collected data using the THGEM detector for THGEMs with and without rim and the 2 inch TEPC detector. c) The spectra obtained with three different THGEMs from package number 1.

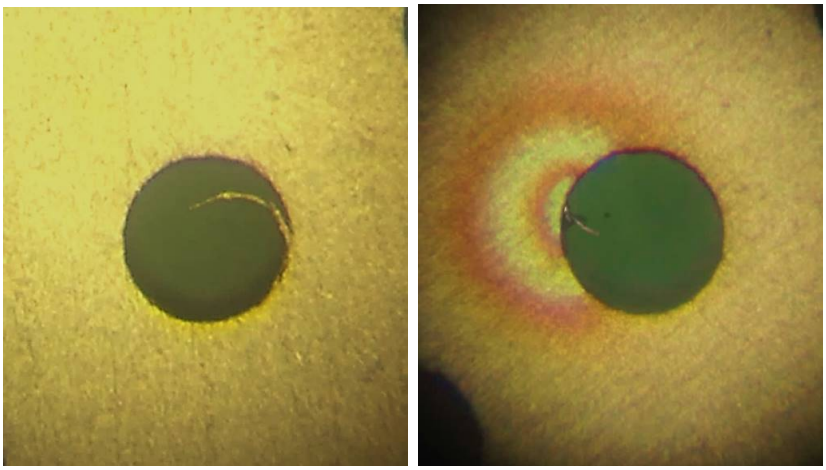

(a) (b)

Figure 6.5: a) A photograph of a THGEM hole under a microscope showing debris generated during drilling process and b) the resulting spark induced damage. The THGEM belongs to the package number one manufactured at Milplex Circuit Inc.

only causing a non-uniform local amplification gain but is also fatal for the THGEM as it may create shortcuts between the upper and lower copper cladded sides under operation or cause sparks that corrupt the amplitude measurements (see Figure 6.5b). Some of the debris is extremely small or hidden in the THGEM holes and is not easily detectable through visual inspection via a microscope. The existence of debris indicates that the post production treatment procedure implemented by the manufacturer has not been efficient. Suspecting the sharp edges and deep surface scratches to be responsible for the extension of events after the proton edge, a second package was ordered. The result obtained with the THGEM samples from the package number two is presented in the following section.

6.4.2.2 Package Number Two

As mentioned earlier, not being satisfied by the outcomes from the first THGEM package manufactured by Milplex Circuit Inc., we ordered the second package asking for a longer polishing process with pumice stone and a more intense micro chemical

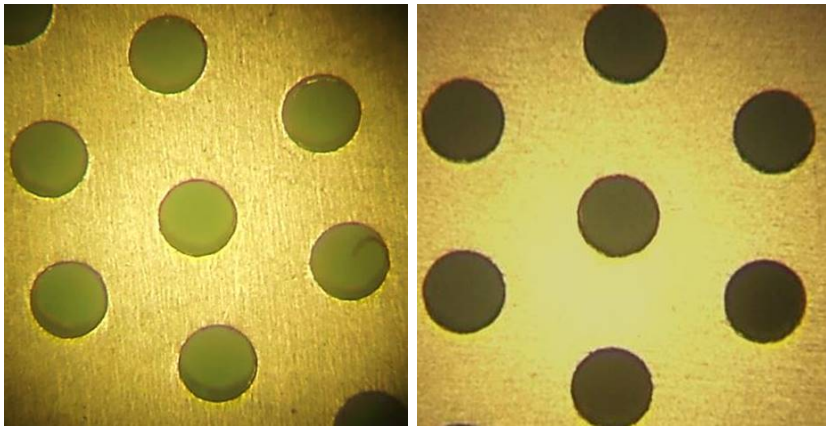

(a) (b)

Figure 6.6: A visual comparison of the hole quality of THGEMs without rim from a) package number one and b) package number two manufactured at Milplex Circuit Inc. The post production treatment treatment resulted in a reduction of THGEM surface scratches and irregularities and an overall improvement for holes shape.

etching process to minimize the existence of debris, sharp edges and surface scratches. When examining the THGEMs under microscope, the effectiveness of the implemented treatment procedure is visible. Figure 6.6a and Figure 6.6b are microscopic photos showing the hole quality of THGEMs from package number one and two. It is apparent from the figure that with reference to a THGEM sample from the first Milplex package, the post production treatment resulted in a noticeable reduction of the surface scratches and size of irregularities.

To see how these improvements are translated in terms of the lineal energy distribution pattern, the THGEMs were tested within the detector assembly with identical operational conditions as used with the THGEM package one. Figure 6.7a illustrates the collected pulse height spectrum. The data set was obtained at the THGEM bias voltage ΔV_{THGEM} of 458 V. The proton drop point that is about the channel number of 2 k for this data set is now clearly evident from the raw data spectrum. The corresponding lineal energy spectrum after calibration is shown in Figure 6.7b. The figure also displays the two spectra obtained with a THGEM from the package number one and the standard 2 inch TEPC using the same beam parameters.

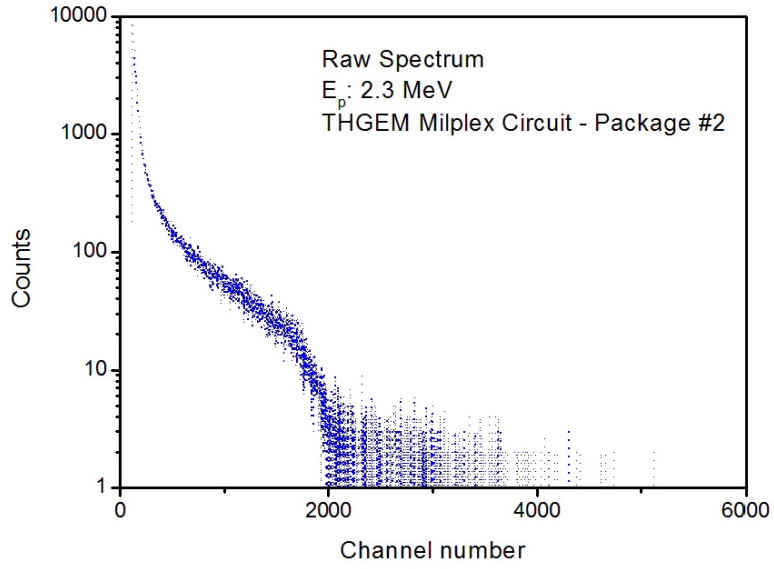

(a)

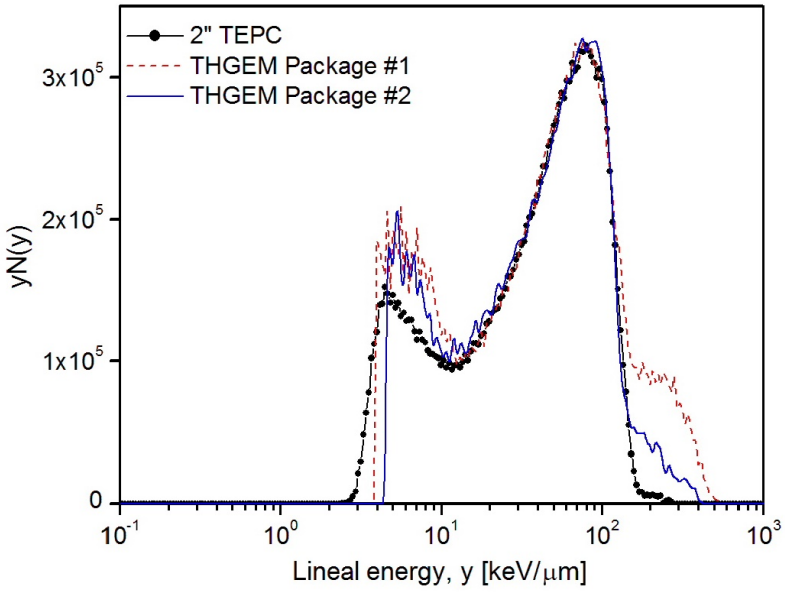

(b)

Figure 6.7: a) The collected pulse height spectrum using the prototype detector with a THGEM from the package number two. The data obtained at the THGEM bias voltage ΔV_{THGEM} of 458 V. The proton drop point is evident about the channel number of 2k. b) The corresponding lineal energy spectrum after calibration along with the two spectra obtained with a THGEM from the package number one and the standard 2 inch TEPC at the proton energy of 2.3 MeV.

When comparing the lineal energy distributions, it is clear that the improvements in the THGEM hole quality result in a considerable progress in the elimination of lineal energy events above the proton edge. The relative area under yN(y) distribution for lineal energy values above the proton edge to the total area under the proton peak improves from about 18% for a THGEM sample from package number one to about 7% for the THGEM package number two. This achievement supports the idea that having a high quality THGEM with perfect round hole such as those that are produced at CERN will help to have a better field uniformity and total removal of the extended tail towards high lineal energy values.

Except for slightly higher relative counts for the gamma-ray component region, the THGEM detector exhibits a comparable spectral distribution with respect to the standard 2 inch TEPC. This is a very promising result for pursuing further steps in the development of the prototype multi-element THGEM detector.

6.4.2.3 Package Number Three

The last relevant comment concerns the high leakage current across the layers leading to a high lineal energy cut off in collected microdosimetric spectra; in particular for the prototype multi-elements THGEM detector with 21 sub-element presented in the previous chapter.

Compared to package number two, the last THGEM package tested within the detector had only a slight correction concerning its design.

To stack the various THGEM detector layers within the aluminum chamber, four holes at the four corners are precisely drilled at needed distances. Four Teflon threaded pins are screwed in these four holes to build a square frame (see Figure 4.10). These pins are used to position the various layers during assembly. The drift cathodes, Rexolite insulators, THGEMs and the readout boards (all shown in Figure 4.4) are mounted on this square frame using four holes in the corners of each layer. As schematically illustrated in a 3D view in Figure 6.8, to maintain the gap across the charge collection

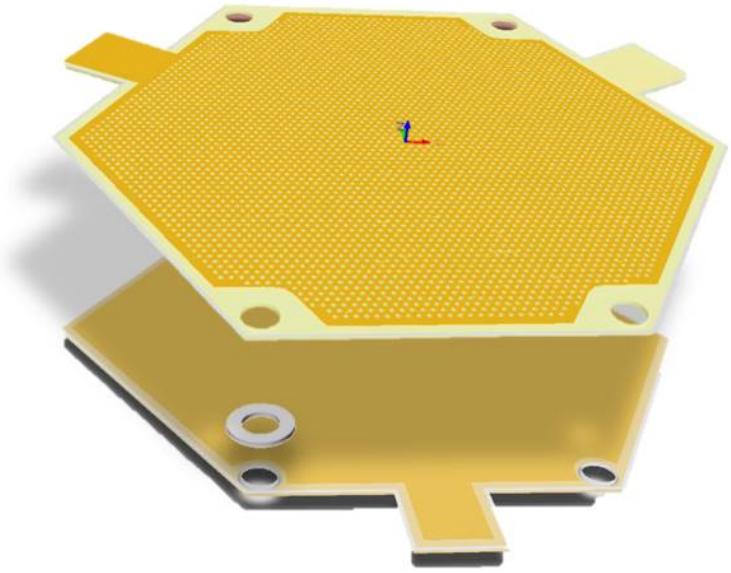

Figure 6.8: A 3D view of the arrangement of the constituent components across the collection gap.

region in each layer, a matrix of four spacers of thickness of 1 mm was used.

Within different stages of the multi-element THGEM detector development, it was noticed that the lineal energy cut off shifts towards higher lineal energy values by increasing the number of sub-elements. In initial attempts of collecting lineal energy distribution using the triple layer assembly, the increase in the lineal energy cut off led to a serious source of concern as the gamma-ray component and part of neutron events were missing in the collected spectra with a common applied THGEM bias voltage. This issue is shown in Figure 6.9. It can be seen that the cut off for the 21 elements (triple layers) increases to about 24 keV/μm for a THGEM bias voltage of 500 V. The cut off lineal energy can be lowered down to about 15 keV/μm for the triple layer assembly by pushing ΔV_{THGEM} very slowly to the maximum safe voltage of 533 V; however, this leads to a distortion in the lineal energy distribution pattern.

To reduce the leakage current across the layers, a critical correction was made in the THGEM design.

In the old design, the copper layer on top and bottom sides of the THGEMs has a

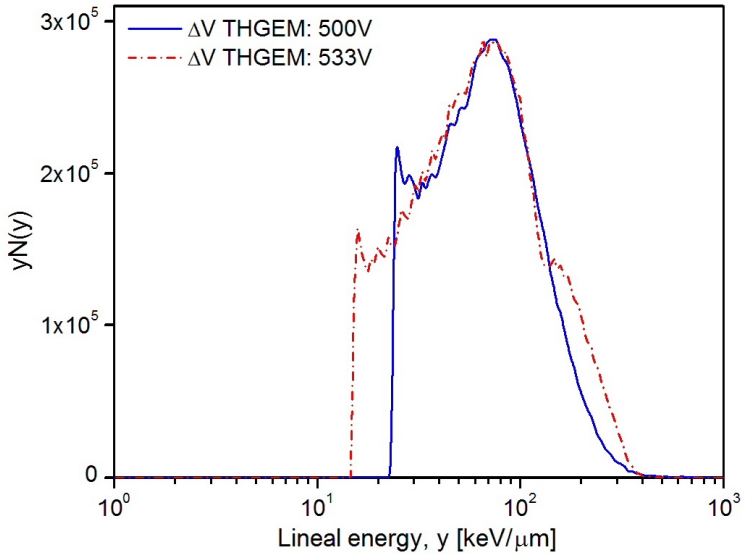

Figure 6.9: The lineal energy distributions obtained in initial attempts with triple layer assembly with different THGEM bias voltages at the proton energy of 2.3 MeV.

narrow clearance around the frame holes. So the inserted spacers were in physical contact with the copper clad layers on THGEMs and readout boards leading to an increase in the leakage current across the layers and worse signal to noise ratios.

This issue was corrected in the third THGEM package by pushing back the copper clad around the frame holes in a way that the spacers are not in touch with the copper layers. This adjustment is displayed in Figure 6.10.

The collected lineal energy distribution with the triple layer assembly after the THGEM adjustment is shown in Figure 6.11. It can be seen that the cut off in the lineal energy is moved back to about 6 keV/μm for the applied THGEM bias voltage ΔV_{THGEM} of 500 V.

Table 6.2 lists the treatment procedures and corrections applied for different THGEM packages.

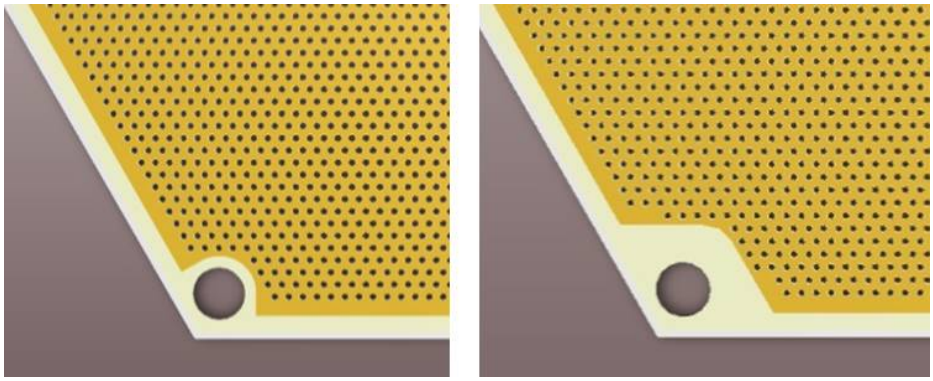

Figure 6.10: Schematic views of the THGEMs before (left side) and after (right side) copper clad correction.

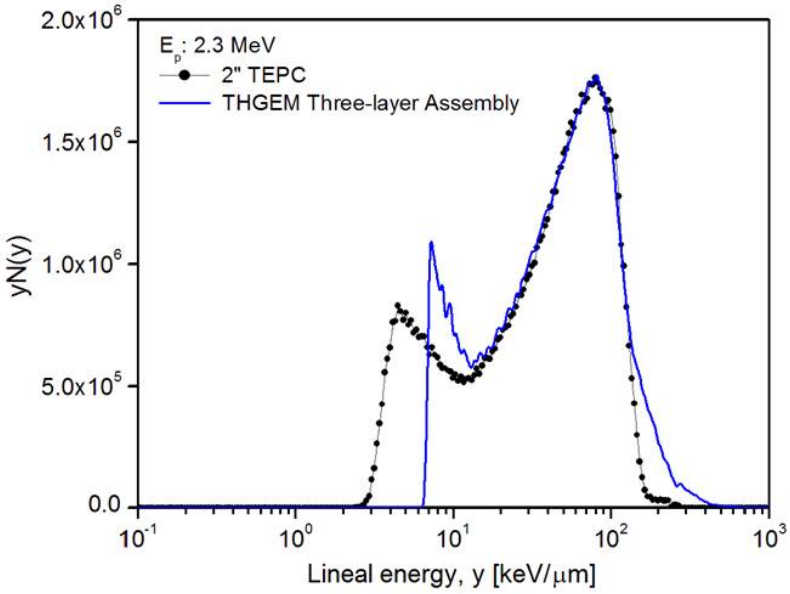

Figure 6.11: The lineal energy distributions obtained with the triple layer assembly after copper clad adjustment at the proton energy of 2.3 MeV.

Table 6.2: Treatment procedures and applied corrections for different THGEM packages.

THGEM	Package #	Rim (mm)	Post Production Treatment
Myro PCB	1	0.1	none
Milplex Circuit	1	0	mechanical: brushing + polishing with pumice chemical: micro etching
Milplex Circuit	2	0	mechanical: longer polishing process with pumice chemical: more intense micro etch
Milplex Circuit	3	0	adding a larger clearance around the corner holes

6.4.3 Verification of the Other Parameters Influences

Some additional tests were conducted using THGEM samples without rim by focusing on the high lineal energy value events to verify the influence of the other parameters on the microdosimetric spectrum pattern. The purpose of these tests was to ensure that the extension of lineal energy values above the proton edge is not related to the detector design or the proton beam parameters. These parameters and the tests outcomes are described and discussed in the following.

6.4.3.1 Dose Rate

In a study by Qashua and Waker [101], the effect of high dose rate on TEPC measurements for both low and high LET components of the radiation field was investigated. The measurements were conducted with a 2 inch standard TEPC. The Tandetron accelerator laboratory at McMaster University was employed as the radiation source to generate high dose rates of mixed fields by varying the beam current from 400 µA to 10 µA at a selected beam energy that gave rise to dead times as high as 75% and as low as 5%. The proton energies investigated for these measurements range from 2.0 to 2.5 MeV. They showed that in high dose rates, the pile up of events leads in extending the event size distribution towards higher lineal energy values and as a result the proton peak position and proton edge are shifted towards higher lineal energies with an extended tail after the recoil proton edge. This effect becomes less obvious as the dead time is reduced and is almost negligible for a dead time below 25%.

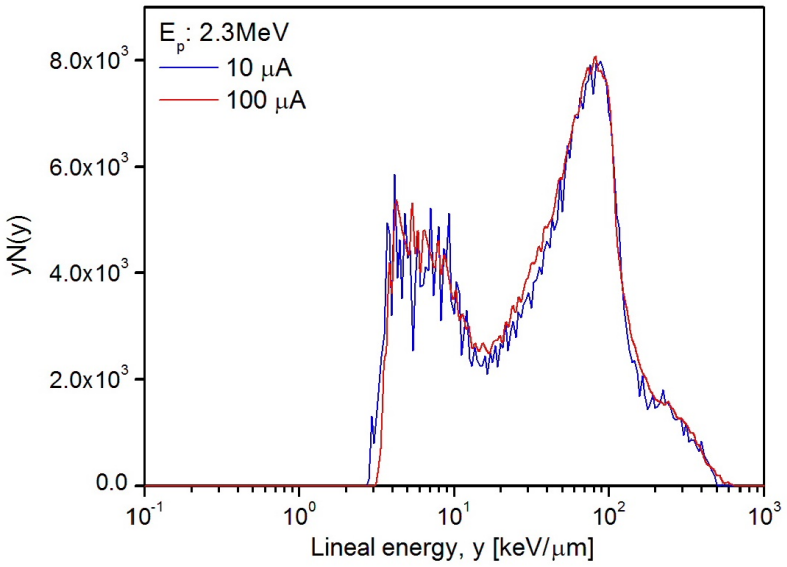

Figure 6.12: The prototype THGEM detector response for the proton current of 10 and 100 (μA) at proton energy of 2.3 MeV (the THGEM sample is chosen from the package two - THGEM without rim).

For experimental results presented in this chapter, all measurements were carried out with a proton current of 50 μA resulting in a dead time less than 5% with the single element THGEM-based TEPC. To ensure that the collected lineal energy distribution pattern is not affected by the applied proton current, the single element THGEM detector response was collected for the proton currents of 10 and 100 μA resulting in the count rates of about 400 cps and 4 kcps, respectively, and negligible dead times at the proton energy of 2.3 MeV. The resulting lineal energy distributions are shown in Figure 6.12. For a qualitative comparison, the spectra are scaled. It can be seen from the figure that in spite of a slightly better peak resolution for the 10 μA proton current, the collected distributions are consistent as expected. Given the fact that the count rates obtained with the THGEM detector at typical operational conditions are not leading to a high pile up effect, it was concluded the high lineal energy tail in the dose distribution pattern is not related to the proton beam current.

6.4.3.2 Proton Beam energy

The THGEM detector response was studied for different proton beam energies. For instance Figure 6.13a and Figure 6.13b show a pulse height spectrum and the corresponding lineal energy distribution, respectively, collected at the proton energy of 2.1 MeV and the proton current of 50 μA. The data set is collected using a THGEM chosen from the package number two - THGEM without rim. The THGEM bias voltage ΔV_{THGEM} was set at 458 V. The proton peak is normalized to the standard TEPC data for comparison.

It can be seen from the lineal energy distributions that similar to the distribution obtain at the proton energy of 2.3 MeV, the THGEM detector shows a relatively higher gamma-ray component to neutron's with reference to the standard 2 inch TEPC. In the neutron lineal energy region the THGEM detector distribution compares well with 2 inch TEPC. However, the distribution is still extended towards higher values above the recoil proton edge.

6.4.3.3 Sensitive Volume Size

The effect of a geometrical parameter has been investigated by comparing the behavior of a THGEM within the detector assembly with two different sensitive volume sizes. This was achieved by replacing the Rexolite insulator hexagon housing seven sensitive volumes with another Rexolite layer casing a single sensitive volume with reduced diameter as illustrated in Figure 6.14. This geometry allows the assessment of the THGEM response for a sensitive volume with a smaller physical dimension and at the same time eliminates any possible interfering from the neighboring sensitive volumes in the previous arrangement. The new Rexolite layer houses a sensitive volume with equal height and diameter of 0.98 cm filled with tissue equivalent gas at the pressure of 85.14 torr to simulate a 2 μm site size. The measurement conditions have been kept as similar as possible. The detector voltage settings used were a drift voltage ΔV_{drift} of 100 V and THGEM bias voltage ΔV_{THGEM} of 583 V. The results are presented

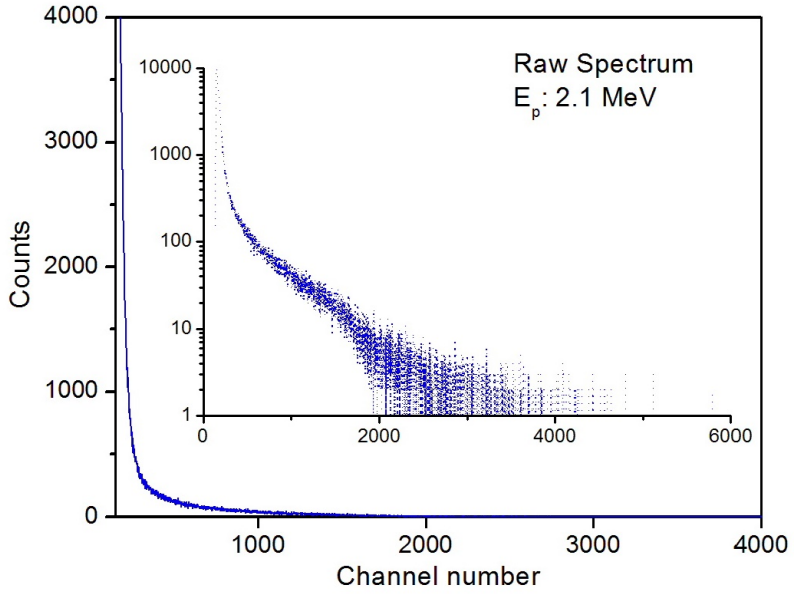

(a)

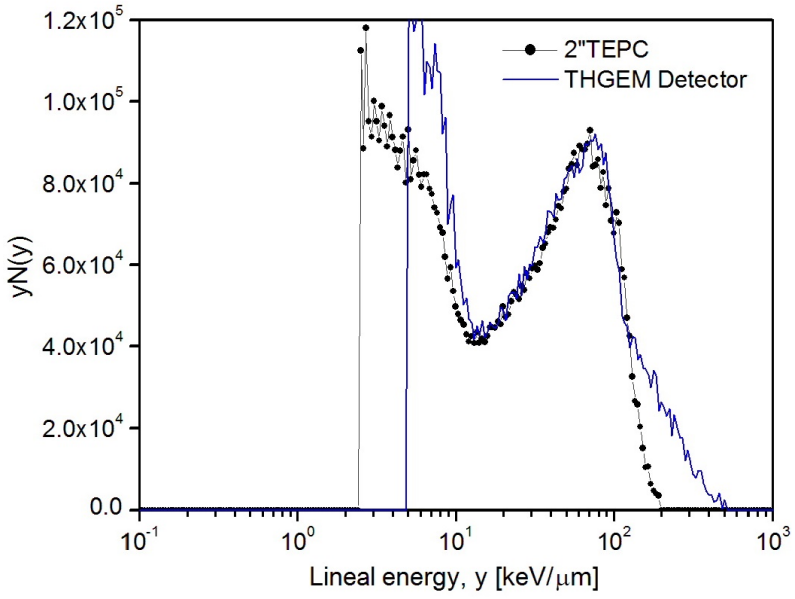

(b)

Figure 6.13: a) The collected pulse height spectrum using the prototype detector with a THGEM from the package number two. The data obtained at the THGEM bias voltage ΔV_{THGEM} of 458 V. The proton drop point is evident about the channel number of 2 k. b) The corresponding lineal energy spectrum after calibration along with the two spectra obtained with a THGEM from the package number one and the standard 2 inch TEPC at the proton energy of 2.1 MeV.

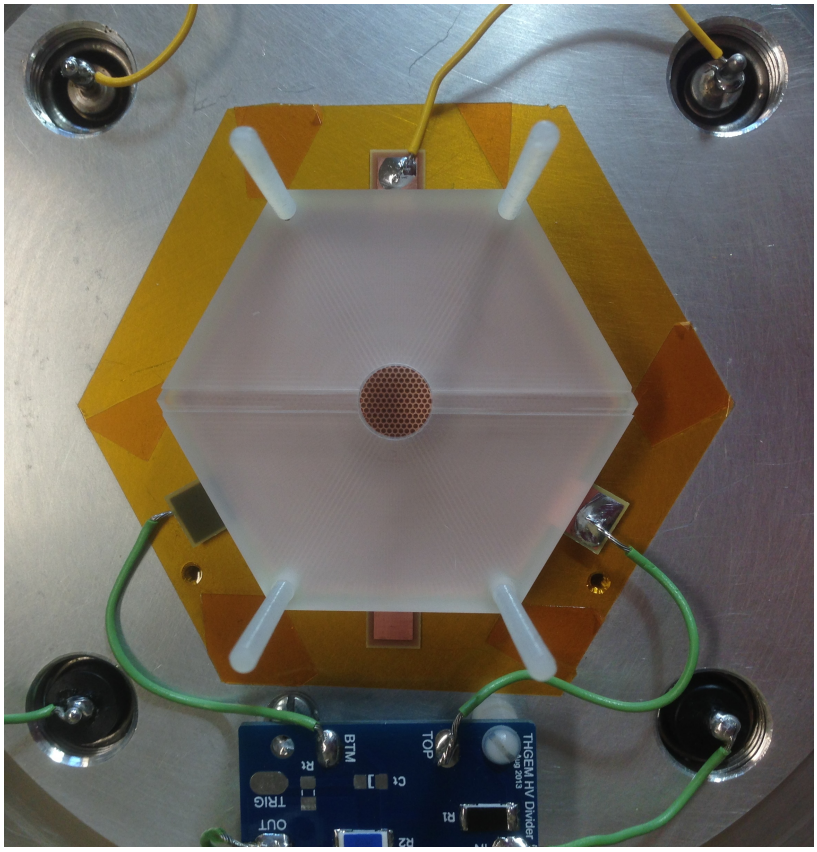

Figure 6.14: A top view of the Rexolite insulator with a single sensitive volume of equal height and diameter of 0.98 cm within the THGEM detector assembly.

in Figure 6.15. It can be seen that the distribution patterns compare well for the neutron component region. A slightly better resolution was obtained with the smaller sensitive volume as expected. No noticeable difference was observed for events above the recoil proton edge. It is apparent from the figure that for the gamma component region, the 0.98 cm sensitive volume shows a lower relative gamma dose to neutrons with respect to 1.7 cm volume. In addition, the minimum detectable lineal energy is lower for the smaller sensitive volume that stems from the fact that the detector capacitance increases with the increase of the sensitive volume size leading to a lower signal to noise ratio. Overall, this observation shows that the behaviors of both detector configurations are comparable in particular for neutron lineal energy region.

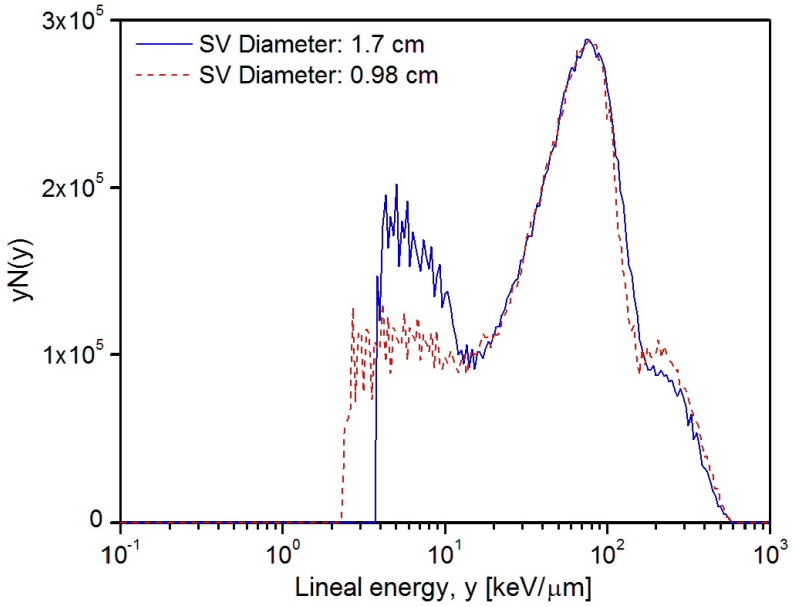

Figure 6.15: The lineal energy distributions obtained from the THGEM detector for two different sensitive volume sizes at the proton energy of 2.3 MeV (the THGEM sample is chosen from the package one - THGEM without rim).

6.4.3.4 Collection Gap

The application of appropriate voltage differences across the electrodes plays a very important role in extraction of a desired signal from the detector. By applying a suitable electric field in the drift region, the charge produced by the interaction of ionizing radiation can be guided into the THGEM holes and amplified inside them. The establishment of another electric field across the collection gap assures the extraction of the resulting charge by the means of the readout board.

The response study of a prototype THGEM for various voltage differences across the bottom of the THGEM and readout board was carried out by Orchard using different resistor values. In the current study a collection gap of 1 mm and the fixed resistor values of 10 and 2 MΩ were used for all data collections, as recommended by the previous studies of our group. However as a case study, the response of the prototype THGEM detector was probed for two collection gaps of 1.0 and 3.0 mm. The collected lineal energy distributions are shown in Figure 6.16. Even though the 3.0 mm

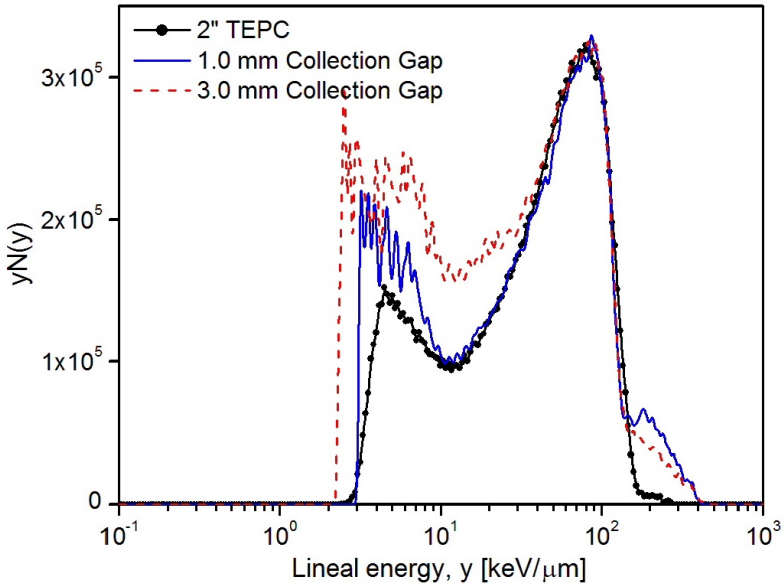

Figure 6.16: The prototype THGEM detector responses for different collection gaps. The event size distributions were collected for two detector configurations with 1.0 and 3.0 mm collection gaps at the identical irradiation conditions (the THGEM sample is chosen from the package two - THGEM without rim).

gap shows a slight improvement in the high lineal energy tail above the proton edge compared to a 1.0 mm collection gap, for the lower lineal energy values the distribution pattern deviates significantly from the standard one. It was observed that the 3 mm gap led to a wider proton peak. It also allowed higher applicable high voltage before discharge observation that resulted in a lower lineal energy cutoff.

6.5 Conclusion

The production, treatment and conditioning procedures of the THGEM samples used in this study were explained. Also, the preliminary tests and experimental setup used for initial performance evaluation of the prototype THGEMs in neutron-gamma radiation fields were described and discussed. It was observed that irregularities in the THGEM holes structure and pattern can heavily influence the performance of a

THGEM as a multiplying element. To eliminate irregular hole borders and defects related to the drilling and production procedure and accomplish perfect round hole edges, an innovative approach was used at CERN for production of the large area THGEMs. A similar approach was implemented for development of the THGEM prototypes in this work including a chain of mechanical and chemical treatments and a post production conditioning process that improved the THGEM performances.
It was realized that the typical industrial PCB techniques and quality control tests dedicated to electronics application are not suitable for development of THGEMs adequate for use in a THGEM-based microdosimetric detector and the inclusion of an extra step to the manufacturing process of the THGEM is needed. To this end development of a custom production process and the related tools is required.

Chapter 7

Conclusion and Future Work

7.1 Summary and Conclusion

Tissue Equivalent Proportional Counters (TEPCs) are considered the standard instrument for microdosimetry [16], aiming at measuring the distribution of the energy deposited by ionizing radiation in a micrometric target, and have been employed for a number of radiation physics, radiation protection and radiation biology applications for many decades [37, 59, 102–104]. Particularly, owing to their excellent capability of decomposing different linear energy transfer components, the TEPC-based instruments have been widely used for measuring radiation doses for mixed neutron-gamma radiation fields where accurate determination of the photon and neutron doses is desired [19, 20, 105].

The basic structure of a traditional TEPC [17] includes a spherical gas cavity in a conducting tissue equivalent A-150 plastic [58] with a central anode wire. Operated in the pulse mode, the TEPC provides a pulse height distribution of amplified signals that are proportional to the individual energy deposition events inside the gas cavity. Since TEPC-based dosemeters are built using tissue equivalent materials, they have a sound physical foundation in determining the radiation dose [6, 16].

In spite of the excellent tissue equivalent material composition, small TEPCs are not

suitable for the neutron dose rates generally encountered in nuclear power plants since their neutron detection efficiency is low, resulting in impractically long counting time. Larger TEPCs, typically 5 inch dia., are certainly better suited, however, they are not sensitive enough for weak fields. This shortcoming arises from the low cross section of the neutron elastic scattering with proton in contrast to the ^{3}He(n,p) and ^{10}B(n,α) reactions that are commonly employed in moderator-based neutron dosemeters [8].

As a solution for the low efficiency problem, a so-called "multi-element" structure, consisting of an array of gaseous cavities rather than a single volume, can improve the neutron detection efficiency greatly while keeping the overall detector size relatively small [43, 44, 73]. However, building a multi-element detector using the traditional proportional counter technology is extremely challenging and expensive, particularly when the dimensions of the individual sensitive volumes are reduced.

For the last decade, TEPC-based instruments have been developed by a few groups using alternative techniques [47, 49, 52, 54, 55] as reviewed explicitly by Agosteo [106]. Among them, the most advanced implemented techniques are Gas Electron Multiplier (GEM) [48] and more recently THick GEM (THGEM) [107] that use hole-type structures for electron multiplication. Unlike the standard GEM which uses polyimide foil with etched holes, the THGEM can be manufactured industrially using the standard printed circuit board (PCB) techniques, allowing the holes to be machined by drilling. This makes THGEM fabrication inexpensive and flexible. The THGEM, descendant of the standard GEM with the physical dimensions of holes, pitch and thickness up to one order of magnitude larger, provides a confined gas multiplication region within sub-millimeter diameter holes. THGEMs were studied and implemented by several groups over a broad range of applications reviewed in Ref. [70] and [83].

In the course of this dissertation, the feasibility of the construction of a multi-element THGEM-based TEPC was investigated. To assess the dependence of the neutron dosimetric response and detection efficiency on detector design, five designs with a different number of gas cavities and an identical outer diameter of about 5 cm were

created. For each design, a Geant4 simulation code was developed reporting the deposited energy per event in the sub-element sensitive volumes for mono-energetic neutron beams with the energy range of 10 keV to 2 MeV. From the simulation results, the lineal energy distributions and microdosimetric quantities were derived for each multi-element design. The absorbed dose responses of all the designs were consistent with the responses of the conventional single cavity detector. The quality factor and the dose equivalent responses were compared with the reference data and showed reasonable agreement with the ideal values for neutron energies above 300 keV while underestimating in the lower energy region. From the neutron detection efficiency analysis, it was demonstrated that the detection efficiency is proportional to the surface area of the detector and increases with increasing the number of the multi-element cavities. The efficiency of the highest cavity density with 61 $\times$ 9 multi elements was on average 5.6 times higher than that of the single cavity design of the same size.

Founded on the extensive Geant4 simulation study, an advanced prototype multi-element gaseous microdosimetric detector was developed using the Thick Gas Electron Multiplier (THGEM) technique. The prototype THGEM multi-element detector consists of three alternating layers of tissue equivalent plastic hexagons and each layer houses an hexagonal array of seven cylindrical gas cavity elements with equal heights and diameters of 17 mm. The final detector structure incorporates 21 gaseous volumes. Owing to the absence of wire electrodes, the THGEM multi-element detector offers flexible and convenient fabrication. The fundamental signal and stability performance of the THGEM detector was tested using a ^{244}Cm alpha source. The detector responses to neutron and gamma-ray were investigated using the McMaster Tandetron ^{7}Li(p,n) neutron source. The dosimetric performance of the detector is presented in contrast to the response of a commercial tissue equivalent proportional counter. The acquired spectra show the expected microdosimetric distribution patterns and the measured dose rates compare well with those obtained by the standard TEPCs collected at

identical conditions. It was observed that for the proton beam energy range of 1.9 to 2.3 MeV the estimated dose rates with the prototype detector is consistently smaller than that of the standard detectors with the maximum discrepancies of 26% and 15% for 0.5 and 2 inch TEPCs, respectively. Compared to the standard 2 inch TEPC that has an overall equivalent size as the prototype detector, an improvement of a factor of 3.0 in neutron detection efficiency has been accomplished without a noticeable degradation in energy resolution. However, to gain reliable spectral and absorbed dose information for the gamma-ray component the minimum detectable lineal energy needs to be improved significantly. This can be achieved via improving the electron multiplication gain either by making better THGEMs with round and smooth holes edges or by employing a cascade of THGEMs in each layer.

7.2 Future work

The detector is a prototype and some refinements are required to improve further the performance of the THGEM-based multi-element TEPC in order to be used in workplaces as an accurate area monitoring device. The following suggestions and recommendations may be beneficial in a future revision of the detector.

7.2.1 Dose Equivalent Response

In the analysis of the dose equivalent response of the THGEM detectors, it was realized that the detector response agrees well with the ambient dose equivalent for the MeV energy region; however, similar to the conventional TEPC-based instruments the detector response deviates from the operational area monitoring quantity $H^*(10)$ for the neutron energy range below 300 keV.

As discussed in subsection 2.3.5, designed to be used as a portable area monitor in mixed neutron-gamma radiation fields, the detector design can be revised by covering

the device with a layer of polyethylene of a specific thickness so that its neutron dose equivalent response matches the ambient dose equivalent at the energy range of interest. This is illustrated schematically in Figure 7.1. It will be beneficial to find the optimal moderator thickness for the multi-element THGEM detector. The optimization of the moderator thickness will be performed in future using Geant4 Monte Carlo Simulation for the revised design of the detector embedded with polyethylene of various thickness. Currently the simulation work is in progress for a single element THGEM detector exposed to varying mono-energetic neutron beams.

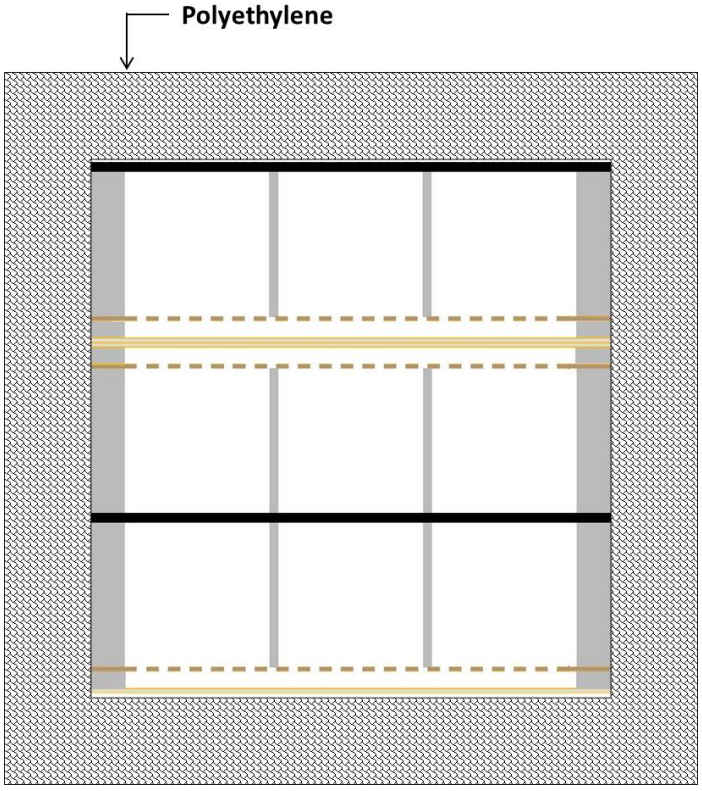

Figure 7.1: A schematic view of the prototype detector embedded with a layer of polyethylene.

7.2.2 Detection Efficiency

The THGEM-based multi-element detector construed in the course of this study is founded on the Monte Carlo simulation study presented in Chapter 3. The detector is a prototype based on the simplest proposed design, i.e. THGEM7×3, and is constructed as a proof of principle. Through Geant4 simulation it was shown that for a given detector volume size the detection efficiency of the multi-element TEPC designs increases by increasing the number of sub-elements and is linearly proportional to the detector surface area. This suggests that the surface area of the ultimate multi-element design needs to be comparable to that of a standard spherical TEPC of a given diameter that is able to measure radiation protection quantities with required statistical precision in a reasonable interval of time. For example, the surface area of the THGEM37×7 is comparable to that of a 5 inch standard TEPC which is a 12.7 cm spherical detector with a surface area of about 506 cm^2. Therefore, it is expected that the THGEM37×7 will be a portable compact alternative to the commercially available 5 inch standard TEPC. Then in future, depending on the application the detector design can be adjusted to achieve an adequate detection efficiency for monitoring weak neutron radiation fields.

7.2.3 Minimum Detectable Lineal Energy

As discussed in section 5.4 the gamma-ray component is evident in the dose distributions obtained by the single element THGEM detector with a cut off lineal energy value of about 3 keV/μm. Increasing the number of subelements and as a consequence the detector capacitance results in a lower signal to noise ratio. This increases the minimum detectable lineal energy value to about 6 keV/μm for the 21 elements for the same applied THGEM bias voltage.

In order to measure gamma-ray dose reliably a significant improvement in the THGEM gain is required for the multi-element configurations. To decrease the cut off lineal energy to values as low as 1 keV/μm a cascade of the THGEM layers will be used in

future. Figure 7.2 shows a schematic diagram of such a possibility with an arrangement of two THGEMs in each layer. By the use of a series of proper electric field values and directions, the charge produced in the first THGEM of each layer is transferred to the second one were it is further multiplied resulting in an overall higher gain across the detector. A signal to noise ratio improvement of a factor of about 10 is expected with the double THGEM assembly. This configurations allows the THGEMs to be operated at lower voltages resulting in increased stability and hence lower probability of THGEM breakdown [99].

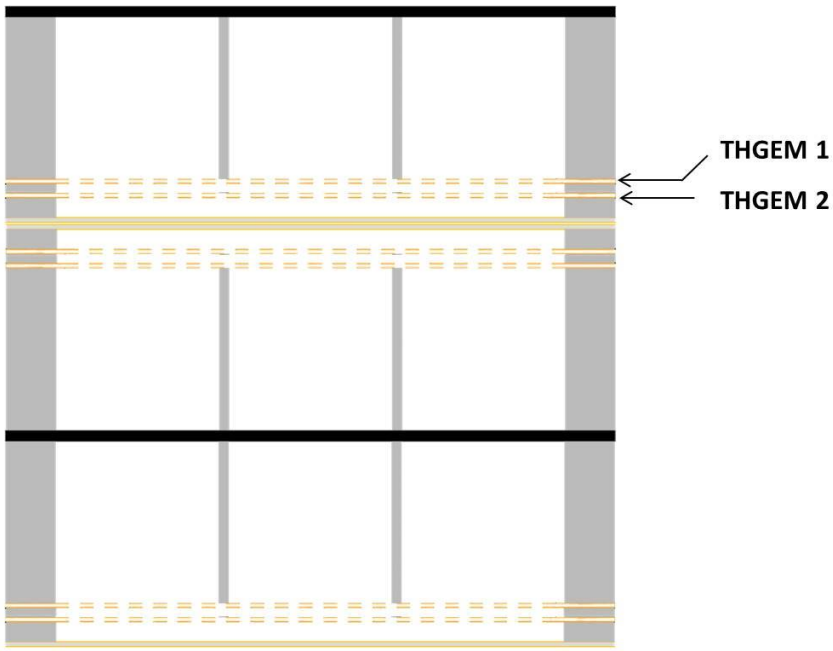

Figure 7.2: A schematic diagram of the arrangement of the various layers for the prototype double THGEM multi-element detector.

7.2.4 Angular Response

It is desired that the detection efficiency remains constant regardless of the incident angle of the neutron beam on the counter. Based on the Geant4 simulation results presented in Chapter 3, for the prototype multi-element THGEM detector it is expected

that for neutrons in the energy range of about hundred keV, the dose equivalent is almost independent of angle and the detector response is close to the ideal case. However, for the MeV energy region, the detector dose equivalent response can show a considerable angular dependency so that the dose equivalent at the incident angle of 180°, with respect to the central vertical axis of the detector, can drop to about 75% of that at 0°.

To overcome this issue, the detector design can be adjusted by adding another layer to

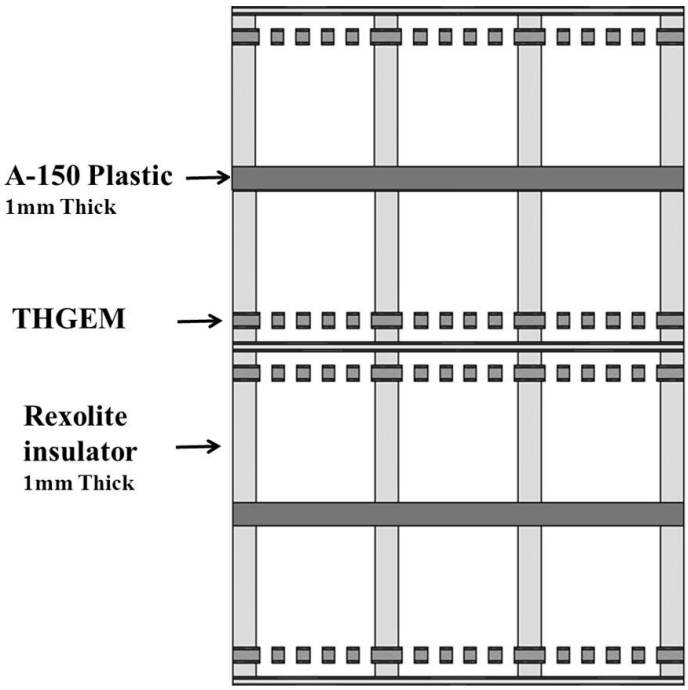

Figure 7.3: A schematic view of the proposed multi-element THGEM detector configuration consisting of four alternating layers of Rexolite hexagons.

the detector stack as shown in Figure 7.3. It can be seen that the arrangement of layers looks identical around the horizontal axis of the detector. In future, it is definitely worth investigating the angular response of the proposed detector configuration in the higher energy neutron fields using either the the plutonium-beryllium source, PuBe-238 (model 2720, Monsanto Inc.), or D-D and D-T neutron fields at the KN accelerator lab (Model KN 3MV Van De Graaff Accelerator). The McMaster Pu-Be

neutron source consists of two individual cylindrical units of plutonium-238 oxide mixed with beryllium-9 with the nominal activities of 9.1 and 8.3 Ci. Both sources are encapsulated in a stainless steel container which is handled with a holding rod. The Pu-Be source has a half-life of 87.4 years and emits neutrons via $^{9}Be(\alpha, n)^{12}C$ reaction. For experimental measurements the source is placed into a shielded collimator along with a cylindrical beryllium moderator of the same size. The emitted neutrons leave the source with a continuous energy spectrum having an average energy of about 4 MeV and maximum energy of 11 MeV. The Pu-Be source and the collimation assembly have been simulated using the Geant4 code by the author and further investigation on this matter is underway.

7.2.5 THGEM Production

In spite of the achievements in the development of a post production treatment and conditioning procedure described in Chapter 6, it was realized that the typical industrial PCB techniques and quality control tests dedicated to electronics application can not meet the requirements for development of THGEMs adequate for use in a THGEM-based microdosimetric detector and more work is required to ensure better performance of THGEM multipliers.

After visual examination and preliminary tests, it turns out that in each package most of the THGEMs were not usable for various reasons, where the acceptance criteria could not be met and the THGEM was removed and replaced. Some of the most seen issues are as the following.

Figure 7.4 shows microscopic views of a THGEM sample from the last THGEM package. As can be seen from Figure 7.4a, the employed treatment procedure resulted in a significant improvement in overall quality of the THGEMs and smoothing of the copper edges at the holes, in particular compare to the MyroPCB THGEM samples. However, in a closer look micro sized sharp points and very fine copper debris are still detectable in some holes under microscope (see Figure 7.4b). As each THGEM sample

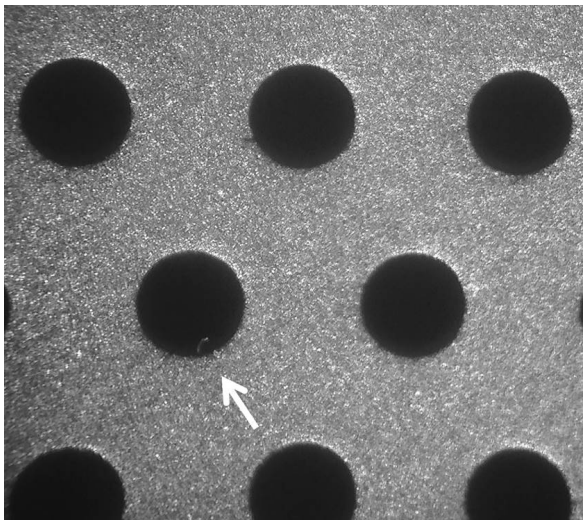

(a)

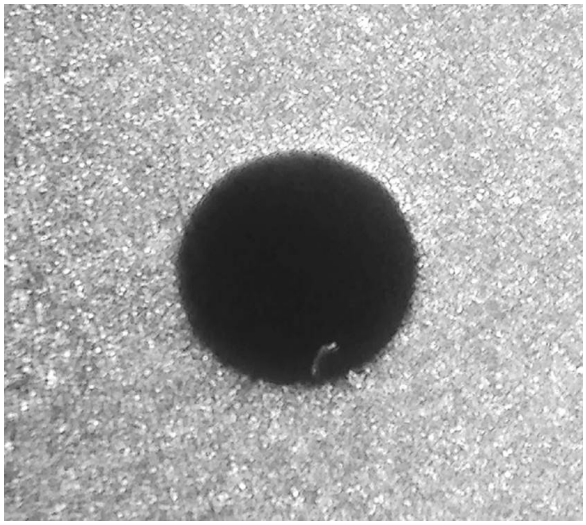

(b)

Figure 7.4: a) A microscopic view of a THGEM sample from the package number three fabricated at Milplex Circut. b) A closeup view of a single THGEM hole showing leftover metal from drilling process.

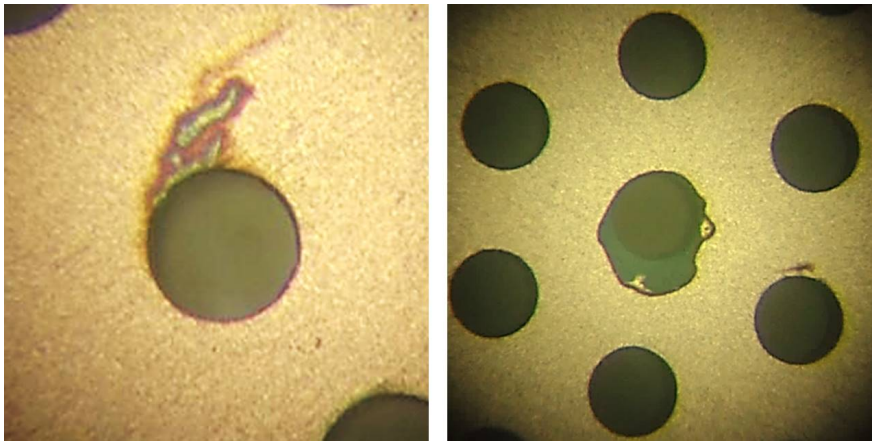

Figure 7.5: Microscopic photographs showing traces of chemical removal of the copper layer generated during micro etching process (left side) and irregular copper clearance produced after global etching (right side).

contains about 4000 holes, detection of such micro size sharp edges and debris via visual inspection under the microscope is not practical or effective.

Also due to irregularities in the material, local defects such as partial or non-uniform removal of the copper layer may occur during micro and global chemical etching process, as displayed in Figure 7.5, making the THGEM not usable.

Carbonized layers produced during the drilling process were observed on the THGEM holes walls as shown in Figure 7.6a. This issue basically wastes the THGEM as it increases the leakage current across the copper layers. As mentioned earlier the milling tools need to be replaced frequently to avoid burning the holes.

The existence of dust particles, glue and other chemical residues was also a big concern during inspection and preparation of THGEMs (see Figure 7.6b). In spite of our request for washing and careful storage and handling of the THGEMs, the delivered packages were not satisfactory on this matter. To avoid this problem, development of an in-lab cleaning protocol to be used before implementation of the THGEMs can save us a lot of time and efforts. The aim of the cleaning procedure is complete removal of the chemical impurities and the manufacture residues in order to improve the electrical characteristics of the THGEMs. The protocol proposed and used at

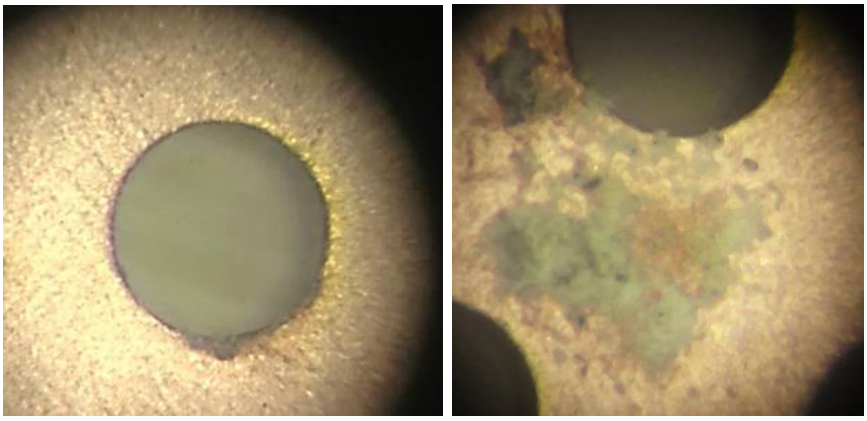

(a) (b)

Figure 7.6: a) A close up view of a hole burned through drilling and created carbonized layer. b) Observed impurities such as dust particles, glue and other chemical residuaes.

CERN for production of large area THGEMs is a good example and is outlined in the following steps:

1. An ultrasonic bath in Sonica pcb solution at 50-60 °C.

2. A rinsing phase in ultrasonic bath with demineralised water and washing with ethanol.

3. A baking phase in an oven at 180 °C for 24 hours.

When inserting the THGEM within the detector, the existence of rugged edges and debris creates high local electric fields resulting in non-uniformity in the electron multiplication gain. Due to high potential difference across the layers, devastating discharges can easily happen at certain sharp edges. This shortcoming limits the amplification gain of the THGEMs. So it is fundamental to avoid irregularities and sharp edges as much as possible. To this end, optimizing the production and post production procedures, even if industrial, sounds vital in development of a reliable THGEM-based neutron dosemeter.

Appendix A

Multi-element Detector Geant4 Simulation Code

The microdosimetric responses of the varying detector geometries discussed in Chapter 3 were simulated using Geant4 Monte Carlo code. Simulations are compilable C++ programs that are supplied with the geometry, the list of physics processes and the initial states. For each detector design a number of simulations were performed for varying incident neutron energies. All the simulations utilize the same physics processes and methods for radiation transport and are written based on a code developed by Hanu [74] that simulates the microdosimetric response of a single cylindrical sensitive volume of height and diameter of 5 mm. The following is the code script for `DetectorConstruction.cc` module that reflects the supplied geometrical parameters written for the THGEM61×9 detector geometry listed as an example. The other modules including the `RunAction.cc, EventAction.cc, SteppingAction.cc` and `PrimaryGeneratorAction.cc` are almost similar to what can be found in ref. [74] and hence are not listed here.

Listing A.1: DetectorConstruction.cc

```
// ********************************************************************
// Based on a simulation code by Andrei Hanu simulating a single sensitive volume of
    5 mm diameter.
// Modified by Zahra Anjomani on October 2012 to simulate a THGEM detector response
    with 549 sensitive volumes of height and diameter of 17 mm arrayed in a hexagonal
     pattern of 61 subelements and 9 layers.
// ********************************************************************
#include "DetectorConstruction.hh"
#include "DetectorConstructionMessenger.hh"
#include "G4Box.hh"
#include "G4Colour.hh"
#include "G4LogicalVolume.hh"
#include "G4Material.hh"
// Include G4NistManager
#include "G4NistManager.hh"
#include "G4PVParameterised.hh"
#include "G4PVPlacement.hh"
#include "G4RunManager.hh"
#include "G4Tubs.hh"
#include "G4Sphere.hh"
#include "G4Cons.hh"
#include "G4VisAttributes.hh"
// Include Boolean Operations
#include "G4UnionSolid.hh"
#include "G4SubtractionSolid.hh"
#include "G4IntersectionSolid.hh"
// Scoring Components
#include "G4VSensitiveDetector.hh"
#include "G4SDManager.hh"
#include <math.h>
DetectorConstruction::DetectorConstruction():fpWorldLogical(0),fpWorldPhysical(0)
{
    // Default Parameters
    A150_Top_Thickness = 1.00*mm;
    A150_Bottom_Thickness = 1.00*mm;
    A150_Extra_Modifier = 0.*mm;
    SignalPad_Thickness = 0.2*mm;
    LowerInsulator_Thickness = 0.2*mm;
    //SVDiameter = .84*mm; // Right Cylinder Approach (ie. Diameter=Height)
    SVHeight = 53.0*mm; //
    SVWall_thickness = 1.*mm;
```

```
    YMax = 4;
    // SV_Width = 50.0*mm;   // Width = Length
    GEM_Insulator_Thickness = 0.6*mm;
    GEM_Conductor_Thickness = 0.05*mm;
    GEM_Hole_Diameter = 0.6*mm;
    GEM_Hole_Pitch = 2*GEM_Hole_Diameter;
    GEM_Diameter = 55.0*mm;
    // GEM_Width = 54.0*mm;
    GEM_Height = A150_Top_Thickness + SVHeight + A150_Extra_Modifier +
        GEM_Conductor_Thickness*2 + GEM_Insulator_Thickness +
        LowerInsulator_Thickness + SignalPad_Thickness + A150_Bottom_Thickness;
    DetectorAngle = 0*deg;

    // materials
    DefineMaterials();

    // Create Interactive Commands For Detector
    detectorMessenger = new DetectorConstructionMessenger(this);
}

DetectorConstruction::~DetectorConstruction()
{
    delete detectorMessenger;
}

G4VPhysicalVolume* DetectorConstruction::Construct()
{
  // Geometry Definition
  return SetupGeometry();
}

void DetectorConstruction::DefineMaterials()
{
  G4String symbol;
  G4double a, z, density;
  G4int ncomponents, natoms;
  G4double fractionmass;

  G4NistManager* manager = G4NistManager::Instance();

  // Define Elements
  G4Element* H = manager->FindOrBuildElement(1);
  G4Element* B = manager->FindOrBuildElement(5);
```

```
G4Element* C = manager->FindOrBuildElement(6);
G4Element* N = manager->FindOrBuildElement(7);
G4Element* O = manager->FindOrBuildElement(8);
G4Element* F = manager->FindOrBuildElement(9);
G4Element* Na = manager->FindOrBuildElement(11);
G4Element* Mg = manager->FindOrBuildElement(12);
G4Element* Al = manager->FindOrBuildElement(13);
G4Element* Si = manager->FindOrBuildElement(14);
G4Element* K = manager->FindOrBuildElement(19);
G4Element* Ca = manager->FindOrBuildElement(20);
G4Element* Ti = manager->FindOrBuildElement(22);
G4Element* Fe = manager->FindOrBuildElement(26);
G4Element* Cu = manager->FindOrBuildElement(29);

// Define A150(Plastic)
G4Material* A150 = new G4Material("A150Plastic", density= 1.138*g/cm3, ncomponents
    =6);
A150->AddElement(H,fractionmass=0.102);
A150->AddElement(C,fractionmass=0.776);
A150->AddElement(N,fractionmass=0.035);
A150->AddElement(O,fractionmass=0.052);
A150->AddElement(F,fractionmass=0.017);
A150->AddElement(Ca,fractionmass=0.018);

// Define Rexolite (a.k.a.  Polystyrene)
G4Material* Rexolite = new G4Material("Rexolite", density= 1.05*g/cm3, ncomponents
    =2);
Rexolite->AddElement(H,fractionmass=0.077418);
Rexolite->AddElement(C,fractionmass=0.922582);

// Define SiO2
G4Material* SiO2 = new G4Material("SiO2", density= 2.64*g/cm3, ncomponents=2);
SiO2->AddElement(Si,natoms=1);
SiO2->AddElement(O,natoms=2);

// Define CaO
G4Material* CaO = new G4Material("CaO", density= 3.34*g/cm3, ncomponents=2);
CaO->AddElement(Ca,natoms=1);
CaO->AddElement(O,natoms=1);

// Define Al2O3
G4Material* Al2O3 = new G4Material("Al2O3", density= 3.97*g/cm3, ncomponents=2);
Al2O3->AddElement(Al,natoms=2);
```

```
Al2O3->AddElement(O,natoms=3);

// Define MgO
G4Material* MgO = new G4Material("MgO", density= 3.60*g/cm3, ncomponents=2);
MgO->AddElement(Mg,natoms=1);
MgO->AddElement(O,natoms=1);

// Define B2O3
G4Material* B2O3 = new G4Material("B2O3", density= 2.55*g/cm3, ncomponents=2);
B2O3->AddElement(B,natoms=2);
B2O3->AddElement(O,natoms=3);

// Define TiO2
G4Material* TiO2 = new G4Material("TiO2", density= 4.230*g/cm3, ncomponents=2);
TiO2->AddElement(Ti,natoms=1);
TiO2->AddElement(O,natoms=2);

// Define Na2O
G4Material* Na2O = new G4Material("Na2O", density= 2.270*g/cm3, ncomponents=2);
Na2O->AddElement(Na,natoms=2);
Na2O->AddElement(O,natoms=1);

// Define K2O
G4Material* K2O = new G4Material("K2O", density= 2.350*g/cm3, ncomponents=2);
K2O->AddElement(K,natoms=2);
K2O->AddElement(O,natoms=1);

// Define Fe2O3
G4Material* Fe2O3 = new G4Material("Fe2O3", density= 5.250*g/cm3, ncomponents=2);
Fe2O3->AddElement(Fe,natoms=2);
Fe2O3->AddElement(O,natoms=3);

// Define F2
G4Material* F2 = new G4Material("F2", density= 0.001580*g/cm3, ncomponents=1);
F2->AddElement(F,natoms=2);

// Define E-Glass Fiberglass
G4Material* E_Glass_Fiberglass = new G4Material("E_Glass_Fiberglass", density=
    2.61*g/cm3, ncomponents=10);
E_Glass_Fiberglass->AddMaterial(SiO2,fractionmass = 0.54);
E_Glass_Fiberglass->AddMaterial(CaO,fractionmass = 0.19);
E_Glass_Fiberglass->AddMaterial(Al2O3,fractionmass = 0.13);
E_Glass_Fiberglass->AddMaterial(MgO,fractionmass = 0.025);
```

```
E_Glass_Fiberglass->AddMaterial(B2O3,fractionmass = 0.075);
E_Glass_Fiberglass->AddMaterial(TiO2,fractionmass = 0.008);
E_Glass_Fiberglass->AddMaterial(Na2O,fractionmass = 0.01);
E_Glass_Fiberglass->AddMaterial(K2O,fractionmass = 0.01);
E_Glass_Fiberglass->AddMaterial(Fe2O3,fractionmass = 0.005);
E_Glass_Fiberglass->AddMaterial(F2,fractionmass = 0.007);

// Diglycidyl Ether of Bisphenol A (C19H20O4)
G4Material* C19H20O4 = new G4Material("C19H20O4", density= 1.16*g/cm3, ncomponents
    =3);
C19H20O4->AddElement(C,natoms=19);
C19H20O4->AddElement(H,natoms=20);
C19H20O4->AddElement(O,natoms=4);

// 1,4-Butanediol Diglycidyl (C10H18O4)
G4Material* C10H18O4 = new G4Material("C10H18O4", density= 1.10*g/cm3, ncomponents
    =3);
C10H18O4->AddElement(C,natoms=10);
C10H18O4->AddElement(H,natoms=18);
C10H18O4->AddElement(O,natoms=4);

// 1,4-Hexanediamine 2,2,4-trimethyl (C9H22N2)
G4Material* C9H22N2 = new G4Material("C9H22N2", density= 0.865*g/cm3, ncomponents
    =3);
C9H22N2->AddElement(C,natoms=9);
C9H22N2->AddElement(H,natoms=22);
C9H22N2->AddElement(N,natoms=2);

// Define Epoxy Resin Epotek 301-1
G4Material* Epoxy_Resin_Epotek_301_1 = new G4Material("Epoxy_Resin_Epotek_301_1",
    density= 1.19*g/cm3, ncomponents=3);
Epoxy_Resin_Epotek_301_1->AddMaterial(C19H20O4,fractionmass = 0.56);
Epoxy_Resin_Epotek_301_1->AddMaterial(C10H18O4,fractionmass = 0.24);
Epoxy_Resin_Epotek_301_1->AddMaterial(C9H22N2,fractionmass = 0.20);

// Define G10-FR4 Insulator
G4Material* G10_FR4 = new G4Material("G10_FR4", density= 1.80*g/cm3, ncomponents=2)
    ;
G10_FR4->AddMaterial(E_Glass_Fiberglass,fractionmass = 0.60);
G10_FR4->AddMaterial(Epoxy_Resin_Epotek_301_1,fractionmass = 0.40);

// Define Copper Pad
G4Material* Copper = new G4Material("Copper", density= 8.96*g/cm3, ncomponents=1);
```

```
  Copper->AddElement(Cu,fractionmass = 1.0);

  // Define TEP Gas
  G4double temperature = 293.15*kelvin;
  G4double pressure = 0.21960659*atmosphere;
  G4double TEPGas_density = 0.0004*g/cm3;
  G4Material* TEP_Gas = new G4Material("TEPGas", TEPGas_density, ncomponents=4,
      kStateGas,temperature,pressure);
  TEP_Gas->AddElement(H,fractionmass=0.1027);
  TEP_Gas->AddElement(C,fractionmass=0.5689);
  TEP_Gas->AddElement(N,fractionmass=0.035);
  TEP_Gas->AddElement(O,fractionmass=0.2934);

  // Define air
  G4Material* air = new G4Material("Air", density= 1.290*mg/cm3, ncomponents=2);
  air->AddElement(N, fractionmass=0.7);
  air->AddElement(O, fractionmass=0.3);
}

G4VPhysicalVolume* DetectorConstruction::SetupGeometry()
{
  //////////////////////////////////////////////////////////////////////////
  // G4 Starting Vector
  G4double G4PosX = 0.;
  G4double G4PosY = 0.;
  G4double G4PosZ = -10.055*cm; // Trying to Center The Sensitive Volume

  //////////////////////////////////////////////////////////////////////////
  // Grab All The Required Materials
  G4Material* a150 = G4Material::GetMaterial("A150Plastic");
  G4Material* rexolite = G4Material::GetMaterial("Rexolite");
  G4Material* copper = G4Material::GetMaterial("Copper");
  G4Material* tep_gas = G4Material::GetMaterial("TEPGas");
  G4Material* g10_fr4 = G4Material::GetMaterial("G10_FR4");
  G4Material* air = G4Material::GetMaterial("Air");

  //////////////////////////////////////////////////////////////////////////
  // Construct The World Volume
  G4Box* worldSolid = new G4Box("World_Solid",           // Name
              5.0*cm, 5.0*cm, 20.0*cm);    // Half lengths

  fpWorldLogical = new G4LogicalVolume(worldSolid,   // Solid
                       air,          // Material
```

```
                    "World_Logical"); // Name

fpWorldPhysical = new G4PVPlacement(0,             // Rotation matrix pointer
                    G4ThreeVector(),   // Translation vector
                    fpWorldLogical,    // Logical volume
                    "World_Physical",  // Name
                    0,         // Mother volume
                    false,          // Unused boolean parameter
                    0);        // Copy number

//////////////////////////////////////////////////////////////////////
// Geometry Details

GEM_Height = A150_Top_Thickness + SVHeight + A150_Extra_Modifier +
    GEM_Conductor_Thickness*2 + GEM_Insulator_Thickness + LowerInsulator_Thickness
    + SignalPad_Thickness + A150_Bottom_Thickness;

//////////////////////////////////////////////////////////////////////
// A150 Base Plastic (Top and Bottom) Mother Volume
G4VSolid* A150BaseSolid = new G4Tubs("A150Base_Solid",           // Name
             0.,GEM_Diameter/2, GEM_Height/2,0.,360.*deg);    // Half lengths

G4LogicalVolume* A150BaseLogical = new G4LogicalVolume(A150BaseSolid,
                                                       a150,
                                                       "A150Base_Logical");
G4RotationMatrix* Rotation = new G4RotationMatrix();
Rotation->rotateY(DetectorAngle); // Detector Rotational Angle
A150BasePhysical = new G4PVPlacement(Rotation,
                  G4ThreeVector(G4PosX,G4PosY,G4PosZ),
                  A150BaseLogical,
                  "A150Base_Physical",
                  fpWorldLogical,
                  false,
                  0,
                  false);

//////////////////////////////////////////////////////////////////////
// Signal Pad
G4VSolid* SignalPadSolid = new G4Tubs("SignalPad_Solid",           // Name
             0.,GEM_Diameter/2, SignalPad_Thickness/2,0.,360.*deg);    // Half
                 lengths

G4LogicalVolume* SignalPadLogical = new G4LogicalVolume(SignalPadSolid,
```

```
                                                    copper,
                                                    "SignalPad_Logical");

G4PosZ += SignalPad_Thickness/2;
SignalPadPhysical = new G4PVPlacement(0,
                  G4ThreeVector(0,0,(A150_Bottom_Thickness+SignalPad_Thickness/2-
                      GEM_Height/2)),
                  SignalPadLogical,
                  "SignalPad_Physical",
                  A150BaseLogical,
                  false,
                  0,
                  false);
////////////////////////////////////////////////////////////////////
// Lower Insulator (Rexolite)
G4VSolid* LowerInsulatorSolid = new G4Tubs("LowerInsulator_Cylinder",          //
    Name
              0.,GEM_Diameter/2, LowerInsulator_Thickness/2, 0., 360.*deg);    //
                  Half lengths

G4LogicalVolume* LowerInsulatorLogical = new G4LogicalVolume(LowerInsulatorSolid,
                                                    rexolite,
                                                    "LowerInsulator_Logical");

LowerInsulatorPhysical = new G4PVPlacement(0,
                  G4ThreeVector(0,0,(A150_Bottom_Thickness+SignalPad_Thickness+
                      LowerInsulator_Thickness/2-GEM_Height/2)),
                  LowerInsulatorLogical,
                  "LowerInsulator_Physical",
                  A150BaseLogical,
                  false,
                  0,
                  false);

////////////////////////////////////////////////////////////////////
// Lower Insulator Gas Cylinder (TEP Gas)
G4VSolid* LowerInsulatorSolid_Cylinder = new G4Tubs("LowerInsulatorSolid_Cylinder"
    ,0.,SVHeight/2,LowerInsulator_Thickness/2,0.,360.*deg);

G4LogicalVolume* LowerInsulator_Cylinder_Logical = new G4LogicalVolume(
    LowerInsulatorSolid_Cylinder,tep_gas,"LowerInsulator_Cylinder_Logical");

LowerInsulatorPhysical_Cylinder = new G4PVPlacement(0,
```

```
                    G4ThreeVector(0,0,0),
                    LowerInsulator_Cylinder_Logical,
                    "LowerInsulatorPhysical_Cylinder",
                    LowerInsulatorLogical,
                    false,
                    0,
                    false);

//////////////////////////////////////////////////////////////////////
// THGEM

  // Starting Volumes
  // G4VSolid* GEM_Hole_Cylinder = new G4Tubs("GEM_Hole_Cylinder",0.,
      GEM_Hole_Diameter/2,(GEM_Insulator_Thickness + 2*GEM_Conductor_Thickness+
      A150_Extra_Modifier)/2,0.,360.*deg);
  G4VSolid* GEM_Insulator_Cylinder = new G4Tubs("GEM_Insulator_Cylinder", 0.,
      GEM_Diameter/2,GEM_Insulator_Thickness/2,0.,360.*deg);
  G4VSolid* GEM_Conductor_Top_Cylinder = new G4Tubs("GEM_Conductor_Top_Cylinder"
      ,0., GEM_Diameter/2, GEM_Conductor_Thickness/2,0.,360.*deg);
  G4VSolid* GEM_Conductor_Bottom_Cylinder = new G4Tubs("
      GEM_Conductor_Bottom_Cylinder",0., GEM_Diameter/2, GEM_Conductor_Thickness
      /2,0.,360.*deg);


  // Create the Lower Conductor
  G4LogicalVolume* GEMConductorBottomLogical = new G4LogicalVolume(
      GEM_Conductor_Bottom_Cylinder, copper,"GEMConductorBottomLogical");

  GEMConductorBottomPhysical = new G4PVPlacement(0,
                      G4ThreeVector(0,0,(A150_Bottom_Thickness+SignalPad_Thickness+
                          LowerInsulator_Thickness+GEM_Conductor_Thickness/2-
                          GEM_Height/2)),
                      GEMConductorBottomLogical,
                      "GEMConductorBottom_Physical",
                      A150BaseLogical,
                      false,
                      0,
                      false);

  // Create the Insulator
  G4LogicalVolume* GEMInsulatorLogical = new G4LogicalVolume(GEM_Insulator_Cylinder
      , g10_fr4,"GEMInsulatorLogical");
```

```
    GEMInsulatorPhysical = new G4PVPlacement(0,
                        G4ThreeVector(0,0,(A150_Bottom_Thickness+SignalPad_Thickness+
                            LowerInsulator_Thickness+GEM_Conductor_Thickness+
                            GEM_Insulator_Thickness/2-GEM_Height/2)),
                        GEMInsulatorLogical,
                        "GEMInsulator_Physical",
                        A150BaseLogical,
                        false,
                        0,
                        false);

    G4PosZ += GEM_Insulator_Thickness/2;

    // Create the Top Conductor
    G4LogicalVolume* GEMConductorTopLogical = new G4LogicalVolume(
        GEM_Conductor_Top_Cylinder, copper,"GEMConductorTopLogical");

    GEMConductorTopPhysical = new G4PVPlacement(0,
                        G4ThreeVector(0,0,(A150_Bottom_Thickness+SignalPad_Thickness+
                            LowerInsulator_Thickness+GEM_Conductor_Thickness+
                            GEM_Insulator_Thickness+GEM_Conductor_Thickness/2-
                            GEM_Height/2)),
                        GEMConductorTopLogical,
                        "GEMConductorTop_Physical",
                        A150BaseLogical,
                        false,
                        0,
                        false);

////////////////////////////////////////////////////////////////////
  // Upper Insulator (Rexolite)

  // Insulator Cylinder
  G4VSolid* UpperInsulatorSolid = new G4Tubs("UpperInsulator_Cylinder",  // Name
                0.,GEM_Diameter/2, SVHeight/2,0.,360.*deg);    // Half lengths

                G4LogicalVolume* UpperInsulatorLogical = new G4LogicalVolume(
                    UpperInsulatorSolid, rexolite, "UpperInsulatorLogical");

  UpperInsulatorPhysical = new G4PVPlacement(0,
                    G4ThreeVector(0,0,(A150_Bottom_Thickness+SignalPad_Thickness+
                        LowerInsulator_Thickness+GEM_Insulator_Thickness+2*
                        GEM_Conductor_Thickness+A150_Extra_Modifier+SVHeight/2-
```

```
                    GEM_Height/2)),
                  UpperInsulatorLogical,
                  "UpperInsulatorPhysical",
                  A150BaseLogical,
                  false,
                  0,
                  false);

////////////////////////////////////////////////////////////////////
 // Sensitive Volume Multi_Cylinder

   G4double C_number = (YMax * 2) + 1;     // Circle number along diameter

   // Calculate Sensitive Volume Diameter
   SVDiameter = ((GEM_Diameter - ((C_number+1)*SVWall_thickness)) / C_number);
   G4double SVHeight_MV = SVDiameter;  // Height == Diameter

   // SV Cylinder Creation (Positioning Variables)
   G4double XLoc;
   G4double YLoc;
   G4double ZLoc;

   G4double Pitch = (SVDiameter + SVWall_thickness);
   G4double Y = (-YMax);

   G4double YLoc_Start = ((sqrt(3.)/2) * Pitch);
   G4double XLoc_Start = ((YMax/2)*Pitch);
   G4double ZLoc_start = (-YMax * Pitch);

   G4VSolid* UpperInsulator_SVCylinder = new G4Tubs("UpperInsulator_SVCylinder",0.,
       SVDiameter/2,SVHeight_MV/2,0.,360.*deg);

   UpperInsulator_SVCylinder_Logical = new G4LogicalVolume(UpperInsulator_SVCylinder
       , tep_gas, "UpperInsulator_SVCylinder_Logical");

   // Making SV Cylinders
   G4int  SV_Cylinder_ID = 1;
   ZLoc = ZLoc_start;

   for (G4int Layer = 1; Layer <= C_number; Layer++){

       while(Y <= YMax) {
```

```
        YLoc = (Y * YLoc_Start);
        XLoc = (-XLoc_Start);

        while(XLoc <= (XLoc_Start + .001)){

            // SV Cylinder Placement
            new G4PVPlacement(0,
                G4ThreeVector(XLoc,YLoc,ZLoc),
                UpperInsulator_SVCylinder_Logical,
                "UpperInsulator_SVCylinder_Physical",
                UpperInsulatorLogical,
                false,
                SV_Cylinder_ID,
                false);

            SV_Cylinder_ID++;
            XLoc += Pitch;
        }

        Y++;
        if (Y <= 0){
            XLoc_Start += (Pitch/2);
        }
        else{
            XLoc_Start -= (Pitch/2);
        }
    }
    Y = (-YMax);
    YLoc_Start = ((sqrt(3.)/2) * Pitch);
    XLoc_Start = ((YMax/2)*Pitch);
    ZLoc += Pitch;
    }

////////////////////////////////////////////////////////////////
  //  Layer Creation
  G4VSolid* UpperInsulator_Layer = new G4Tubs("UpperInsulator_Layer",0.,GEM_Diameter
      /2,SVWall_thickness/2,0.,360.*deg);

  G4LogicalVolume* UpperInsulator_Layer_Logical = new G4LogicalVolume(
      UpperInsulator_Layer, a150, "UpperInsulator_Layer_Logical");
  G4int Layer_ID = 1;
  G4double LLoc = SVHeight_MV + SVWall_thickness/2 - SVHeight/2 ;   //(-((YMax - 1)*
      Pitch + Pitch/2));
```

```
for (G4int NoLayer = 1;NoLayer <= (C_number - 1);NoLayer++){
    new G4PVPlacement(0,
              G4ThreeVector(0,0,LLoc),
              UpperInsulator_Layer_Logical,
              "UpperInsulator_Layer_Physical",
              UpperInsulatorLogical,
              false,
              Layer_ID,
              false);

          Layer_ID++;
          LLoc += Pitch;
}


////////////////////////////////////////////////////////////////////////
// Output Geometry Information
G4double Mass = UpperInsulator_SVCylinder_Logical->GetMass();
SVCylinderMass = (Mass * SV_Cylinder_ID);
G4cout    << "\n-------------------- START Geometry Details
    ----------------------------"
          << "\nGEM Height: " << GEM_Height/cm << " cm"
          << "\nGEM Diameter: " << GEM_Diameter/cm << " cm"
          //<< "\nGEM Length: " << GEM_Length/cm << " cm"
          << "\nSV Diameter: " << SVDiameter/cm << " cm"
          << "\nSV Height: " << SVHeight/cm << " cm"
          << "\nTOP A150: " << A150_Top_Thickness/cm << " cm"
          << "\nBOTTOM A150: " << A150_Bottom_Thickness/cm << " cm"
          << "\nSignal Pad: " << SignalPad_Thickness/mm << " mm"
          << "\nLower Insulator: " << LowerInsulator_Thickness/mm << " mm"
          << "\nGEM Hole Diameter: " << GEM_Hole_Diameter/mm << " mm"
          << "\nGEM Pitch: " << GEM_Hole_Pitch/mm << " mm"
          << "\nGEM Modifier Thickness: " << A150_Extra_Modifier/mm << " mm"
          << "\nDetector Angle: " << DetectorAngle/deg << " degrees"
          << "\nSensitive Volume Mass: " << SVCylinderMass/kg << " kg"
          << "\n---------------------- END Geometry Details
              ----------------------------\n"
          << G4endl;
////////////////////////////////////////////////////////////////////////
// Visualisation attributes
// A150
G4VisAttributes* A150Attributes = new G4VisAttributes(G4Colour(1.0,1.0,1.0,0.5));
```

```
  A150Attributes->SetForceSolid(true);
  A150BaseLogical->SetVisAttributes(A150Attributes);
  UpperInsulator_Layer_Logical->SetVisAttributes(A150Attributes);
  // SignalPad
  G4VisAttributes* SignalPadAttributes = new G4VisAttributes(G4Colour(1.0,0.,1.0,1.0)
      );
  SignalPadAttributes->SetForceSolid(true);
  SignalPadLogical->SetVisAttributes(SignalPadAttributes);
  // Insulator
  G4VisAttributes* InsulatorAttributes = new G4VisAttributes(G4Colour(0.,1.0,0.,1.0))
      ;
  InsulatorAttributes->SetForceSolid(true);
  LowerInsulatorLogical->SetVisAttributes(InsulatorAttributes);
  UpperInsulatorLogical->SetVisAttributes(InsulatorAttributes);
  // GEM Holes & Sensitive Volume
  G4VisAttributes* GEMHoleAttributes = new G4VisAttributes(G4Colour(1.0,0.,0.,1.0));
  GEMHoleAttributes->SetForceSolid(true);
  // GEM_Hole_Cylinder_Logical->SetVisAttributes(GEMHoleAttributes);
  LowerInsulator_Cylinder_Logical->SetVisAttributes(GEMHoleAttributes);
  UpperInsulator_SVCylinder_Logical->SetVisAttributes(GEMHoleAttributes);

  //////////////////////////////////////////////////////////////////////////

  // Return world volume
  return fpWorldPhysical;
}

void DetectorConstruction::SetDetectorAngle(G4double val)
{
  // change Detector Rotational Angle
  DetectorAngle = val;
}

void DetectorConstruction::SetModifierThickness(G4double val)
{
  // change Detector Rotational Angle
  A150_Extra_Modifier = val;
}

void DetectorConstruction::UpdateGeometry()
{
    G4RunManager::GetRunManager()->DefineWorldVolume(SetupGeometry());
}
```

Appendix B

Gain Measurements

The signal amplification takes place through the Townsend Avalanche process in which the drift electrons are accelerated further in the high electric field values within the THGEM holes and gain enough kinetic energy to initiate secondary ionization in collisions with the gas molecules and form a cascade of electrons. This leads to an exponential rise in the total amount of electrons in the electron cloud. For an initial number of electrons n_0 traveling a path length x in the detector, the number of electrons is given by

$$n(x) = n_0 \; exp(\alpha x) \tag{B.1}$$

where α is the first Townsend coefficient. It is defined as the mean number of secondary electrons produced per unit path length per electron and depends on the nature of the filling gas, gas pressure and electric field strength.

The electron multiplication gain is defined as the quotient of the collected electron to the initial number of electrons

$$Gas\ Gain = \frac{n}{n_0} = \frac{Collected\ charge}{Initial\ ionization\ charge} \tag{B.2}$$

To calculate the prototype detector gas gain the following steps were performed for different THGEM bias voltage leading to the expected exponential behavior discussed

in subsection 5.3.1.

Step 1. Initial ionization charge

The lineal energy value of the proton edge was used to calculate the maximum energy deposited by proton as following

$$\varepsilon = y \times \bar{l} = 115\ keV/\mu m \times 1.33\ \mu m = 153.3\ keV \tag{B.3}$$

Where the mean chord length is $\bar{l} = 2/3 \times 2\ \mu m$ and the lineal energy value of the recoil proton edge is 115 keV/μm from the collected lineal energy spectrum at the proton beam energy of 2.3 MeV. Then the corresponding number of electrons produced with this event size will be

$$initial\ number\ of\ electrons = \frac{\varepsilon}{w} \tag{B.4}$$

Where ω is the average energy lost by the ionizing particle per ion pair. A ω value of 28.2 eV from ref. [98] was used for protons in propane-based tissue equivalent gas.

Step 2. Collected charge

Using a pulse generator, a pulse amplitude of V_t was created and the corresponding channel number was recorded. For this pulse, the delivered charge on the preamplifier test input capacitor C_t can be calculated as

$$Q = V_t C_t \tag{B.5}$$

That is equivalent to the number of collected electrons of

$$number\ of\ collected\ electrons = \frac{Q}{e} = \frac{V_t C_t}{e} \tag{B.6}$$

or

$$number\ of\ electrons\ per\ channel = \frac{V_t C_t}{e \times test\ pulse\ channel\ number} \tag{B.7}$$

The proton drop point was defined from the collected pulse height spectrum and the corresponding channel number was recorded as the proton drop point channel number. So the number of electrons collected for the proton drop point is

$$number\ of\ electrons\ at\ proton\ drop\ point = \frac{proton\ ch\ number}{test\ pulse\ ch\ number} \times \frac{V_t C_t}{e} \tag{B.8}$$

Step 3. Gas gain

Now the gas gain can be calculated as

$$Gas\ Gain = \frac{Collected\ charge}{Initial\ ionization\ charge} \tag{B.9}$$

or

$$Gas\ Gain = \frac{proton\ ch\ number}{test\ pulse\ ch\ number} \times \frac{V_t C_t}{e} \times \frac{w}{\epsilon} \tag{B.10}$$

Bibliography

[1] *Determination of Dose Equivalents Resulting from External Radiation Sources*, ser. ICRU Report 39, Bethesda, 1985.

[2] *ICRP Publication 60: Recommendation of the International Commission on Radiological Protection*, ser. ICRP Publication. Oxford: International Commission on Radiological Protection, 1990.

[3] B. Siebert and H. Schuhmacher, "Quality factors, ambient and personal dose equivalent for neutrons, based on the new icru stopping power data for protons and alpha particles," *Radiation Protection Dosimetry*, vol. 58, no. 3, pp. 177–183, 1995.

[4] *ICRP Publication 74: Conversion Coefficients for Use in Radiological Protection Against External Radiation*, ser. ICRP Publication. Oxford: International Commission on Radiological Protection, 1996.

[5] *ICRP Publication 15: Protection against Ionizing Radiation from External Sources*, ser. ICRP Publication. Oxford:Pergamon: International Commission on Radiological Protection, 1970.

[6] J. Booz, "Advantages of introducing microdosimetric instruments and methods into radiation protection," *Radiation Protection Dosimetry*, vol. 9, no. 3, pp. 175–183, 1984.

[7] H. Schuhmacher, "Tissue-equivalent proportional counters in radiation protection dosimetry: Expectations and present state," *Radiation Protection Dosimetry*, vol. 44, no. 1-4, pp. 199–206, 1992.

[8] G. F. Knoll, *Radiation detection and measurement*. John Wiley & Sons, 2010.

[9] E. Amaldi, L. Hafstad, and M. Tuve, "Neutron yields from artificial sources," *Physical Review*, vol. 51, no. 11, p. 896, 1937.

[10] R. L. Bramblett, R. I. Ewing, and T. Bonner, "A new type of neutron spectrometer," *Nuclear Instruments and Methods*, vol. 9, no. 1, pp. 1–12, 1960.

[11] J. Leake, "A spherical dose equivalent neutron detector," *Nuclear Instruments and Methods*, vol. 45, no. 1, pp. 151–156, 1966.

[12] D. Hankins, "The substitution of a bf3 probe for the lii crystal in neutron rem-meters." *Health physics*, vol. 14, no. 5, pp. 518–520, 1968.

[13] J. W. Leake, "An improved spherical dose equivalent neutron detector," *Nuclear Instruments and Methods*, vol. 63, no. 3, pp. 329–332, 1968.

[14] I. Andersson and J. Braun, "Neutron Rem Counter with Uniform Sensitivity from 0.025 to 10 MeV," in *Proceedings of the IAEA Symposium on Neutron Dosimetry*, 1963, pp. 87–95.

[15] H. Tagziria, R. Tanner, D. Bartlett, and D. Thomas, "Evaluation and monte carlo modelling of the response function of the leake neutron area survey instrument," *Nuclear Instruments and Methods in Physics Research Section A*, vol. 531, no. 3, pp. 596 – 606, 2004.

[16] *Microdosimetry*, ser. ICRU Report 36, Bethesda, 1983.

[17] H. H. Rossi and W. Rosenzweig, "A device for the measurement of dose as a function of specific ionization," *Radiology*, vol. 64, pp. 404–411, 1955.

[18] G. Dietze, H. Menzel, and H. Schumacher, "Determination of dose equivalent with tissue-equivalent proportional counters," *Radiation Protection Dosimetry*, vol. 28, no. 1-2, pp. 77–81, 1989.

[19] A. Waker, "Principals of experimental microdosimetry," *Radiation Protection Dosimetry*, vol. 61, no. 4, pp. 297–308, 1995.

[20] A. Waker, K. Szornel, and J. Nunes, "TEPC performance in the CANDU workplace," *Radiation Protection Dosimetry*, vol. 70, no. 1-4, pp. 197–202, 1997.

[21] G. C. Taylor, R. D. Bentley, T. J. Conroy, R. Hunter, J. B. L. Jones, A. Pond, and D. J. Thomas, "The evaluation and use of a portable tepc system for measuring in-flight exposure to cosmic radiation," *Radiation Protection Dosimetry*, vol. 99, no. 1-4, pp. 435–438, 2002.

[22] R. Tayama, Y. Fujita, M. Tadokoro, H. Fujimaki, T. Sakae, and T. Terunuma, "Measurement of neutron dose distribution for a passive scattering nozzle at the proton medical research center (PMRC)," *Nuclear Instruments and Methods in Physics Research Section A*, vol. 564, no. 1, pp. 532 – 536, 2006.

[23] A. Marchetto, J. Leroux, Y. Herbaut, M. Latu, and P. Tinelli, "CIRCEG, a portable device for photon-neutron dosimetry," *Radiation Protection Dosimetry*, vol. 23, no. 1-4, pp. 253–256, 1988.

[24] W. Quam, T. Del Duca, W. Plake, G. Graves, and T. DeVore, "Pocket neutron rem meter," *Nuclear Science, IEEE Transactions on*, vol. 29, no. 1, pp. 637–640, 1982.

[25] T. Schmitz, K. Morstin, P. Olko, and J. Booz, "The KFA counter: A dosimetry system for use in radiation protection," *Radiation Protection Dosimetry*, vol. 31, no. 1-4, pp. 371–375, 1990.

[26] A. Kunz, E. Arend, E. Dietz, S. Gerdung, R. Grillmaier, T. Lim, and P. Pihet, "The Homburg Area Neutron Dosemeter HANDI: Characteristics and optimisation of the operational instrument," *Radiation Protection Dosimetry*, vol. 44, no. 1-4, pp. 213–218, 1992.

[27] M. Cosack and H. Lesiecki, "Dose equivalent survey meters," *Radiation Protection Dosimetry*, vol. 10, no. 1-4, pp. 111–119, 1985.

[28] G. Dietze, J. Booz, A. Edwards, S. Guldbakke, H. Kluge, J. Leroux, L. Lindborg, H. Menzel, V. Nguyen, T. Schmitz *et al.*, "Intercomparison of dose equivalent meters based on microdosimetric techniques," *Radiation Protection Dosimetry*, vol. 23, no. 1-4, pp. 227–234, 1988.

[29] H. Menzel, L. Lindborg, T. Schmitz, H. Schuhmacher, and A. Waker, "Intercomparison of dose equivalent meters based on microdosimetric techniques: detailed analysis and conclusions," *Radiation Protection Dosimetry*, vol. 29, no. 1-2, pp. 55–68, 1989.

[30] H. G. Menzel, L. Lindborg, T. Schmitz, H. Schuhmacher, and A. J. Waker, "Intercomparison of dose equivalent meters based on microdosimetric techniques: Detailed analysis and conclusions," *Radiation Protection Dosimetry*, vol. 29, no. 1-2, pp. 55–68, 1989.

[31] D. Thomas, A. Waker, J. Hunt, A. Bardell, and B. More, "An intercomparison of neutron field dosimetry systems," *Radiation Protection Dosimetry*, vol. 44, no. 1-4, pp. 219–222, 1992.

[32] A. Aroua, M. Boschung, F. Cartier, M. Grecescu, S. Prêtre, J. Valley, and C. Wernli, "Characterisation of the mixed neutron-gamma fields inside the swiss nuclear power plants by different active systems," *Radiation protection dosimetry*, vol. 51, no. 1, pp. 17–25, 1994.

[33] D. Rogers, "Why not to trust a neutron remmeter." *Health physics*, vol. 37, no. 6, pp. 735–742, 1979.

[34] J. Leake, "The effect of ICRP (74) on the response of neutron monitors," *Nuclear Instruments and Methods in Physics Research Section A*, vol. 421, no. 1–2, pp. 365 – 367, 1999.

[35] Y. Eisen, R. Brake, D. Vasilik, B. Erkkila, and G. Littlejohn, "The Performance of Low Pressure Tissue-Equivalent Chambers and a New Method for Parameterising the Dose Equivalent," *Radiation Protection Dosimetry*, vol. 15, no. 2, pp. 117–130, 1986.

[36] C. Hirning and A. Waker, "Needs and performance requirements for neutron monitoring in the nuclear power industry," *Radiation protection dosimetry*, vol. 70, no. 1-4, pp. 67–72, 1997.

[37] A. J. Waker, U. Schrewe, J. Burmeister, J. Dubeau, and R. A. Surette, "Classical microdosimetry in radiation protection dosimetry and monitoring," *Radiation protection dosimetry*, vol. 99, no. 1-4, pp. 311–316, 2002.

[38] B. Kawecka, K. Morstin, and J. Booz, "Optimisation of the design of microdosimetric dose equivalent meters," *Radiation Protection Dosimetry*, vol. 9, no. 3, pp. 203–206, 1984. [Online]. Available: http://rpd.oxfordjournals.org/content/9/3/203.abstract

[39] P. Pihet, H. Menzel, W. Alberts, and H. Kluge, "Response of tissue-equivalent proportional counters to low and intermediate energy neutrons using modified te-3he gas mixtures," *Radiation Protection Dosimetry*, vol. 29, no. 1-2, pp. 113–118, 1989.

[40] W. Alberts, E. Dietz, S. Guldbakke, H. Kluge, and H. Schuhmacher, "International intercomparison of tepc systems used for radiation protection," *Radiation Protection Dosimetry*, vol. 29, no. 1-2, pp. 47–53, 1989.

[41] P. Kliauga, A. Waker, and J. Barthe, "Design of Tissue-Equivalent Proportional Counters," *Radiation Protection Dosimetry*, vol. 61, no. 4, pp. 309–322, 1995.

[42] G. Tessler and S. Glickstein, "Monte Carlo Calculation of the Response of the Portable Neutron Monitor SNOOPY," *Health Physics*, vol. 28, no. 3, pp. 197–204, 1975.

[43] H. Rossi, "Multi-element dosimeters for radiation protection measurements," *Health Physics*, vol. 44, no. 4, pp. 403–405, 1983.

[44] P. Kliauga, H. Rossi, and G. Johnson, "A Multi-element Proportional Counter for Radiation Protection Measurements," *Health Physics*, vol. 57, no. 4, pp. 631–636, 1989.

[45] L. Braby, G. Johnson, and J. Barthe, "Practical Considerations in the Design and Construction of Tissue-Equivalent Proportional Counters," *Radiation Protection Dosimetry*, vol. 61, no. 4, pp. 351–379, 1995.

[46] Y. Giomataris, P. Rebourgeard, J. Robert, and G. Charpak, "MICROMEGAS: a high-granularity position-sensitive gaseous detector for high particle-flux environments ," *Nuclear Instruments and Methods in Physics Research Section A*, vol. 376, no. 1, pp. 29 – 35, 1996.

[47] J. Dubeau, A. Waker, M. Biggar, M. Rayner, E. Sommerville, and S. Welch, "Dosimetric Response to Gamma-rays and Neutrons of a Tissue-equivalent Microstrip Gas Counter," *Radiation Protection Dosimetry*, vol. 91, no. 4, pp. 391–401, 2000.

[48] F. Sauli, "GEM: A new concept for electron amplification in gas detectors," *Nuclear Instruments and Methods in Physics Research Section A*, vol. 386, no. 2–3, pp. 531 – 534, 1997.

[49] M. Farahmand, A. Bos, J. Huizenga, L. D. Nardo, and C. van Eijk, "Design of a new tissue-equivalent proportional counter based on a gas electron multiplier," *Nuclear Instruments and Methods in Physics Research Section A*, vol. 509, no. 1–3, pp. 262 – 267, 2003.

[50] J. Dubeau and A. Waker, "Neutron microdosimetric response of a gas electron multiplier," *Radiation Protection Dosimetry*, vol. 128, no. 4, pp. 413–420, 2008.

[51] A. Waker, J. Dubeau, and R. Surette, "The application of micropatterned devices for radiation protection dosimetry and monitoring," *Nuclear Technology*, vol. 168, no. 1, pp. 202–206, 2009.

[52] S. Byun, G. Spirou, A. Hanu, W. Prestwich, and A. Waker, "Simulation and First Test of a Microdosimetric Detector Based on a Thick Gas Electron Multiplier," *Nuclear Science, IEEE Transactions on*, vol. 56, no. 3, pp. 1108–1113, June 2009.

[53] A. Hanu, S. Byun, and W. Prestwich, "A monte carlo simulation of the microdosimetric response for thick gas electron multiplier," *Nuclear Instruments and Methods in Physics Research Section A*, vol. 622, no. 1, pp. 270 – 275, 2010.

[54] G. Orchard, K. Chin, W. Prestwich, A. Waker, and S. Byun, "Development of a thick gas electron multiplier for microdosimetry," *Nuclear Instruments and Methods in Physics Research Section A*, vol. 638, no. 1, pp. 122 – 126, 2011.

[55] C. Wang, M. Seidaliev, and A. Mandapaka, "Development and Test of a GEM-based TEPC for Neutron Protection Dosimetry," *Health Physics*, vol. 94, no. 5, pp. 440–448, 2008.

[56] *Microdosimetry and Its Applications*. Berlin: Springer, 1996.

[57] A. L. Cauchy, *Mémoire sur la rectification des courbes et la quadrature des surfaces courbes*, 1832.

[58] R. Shonka, J. Rose, and G. Failla, "Conducting plastic equivalent to tissue, air and polystyrene," in *Proceedings of the Second United Nations International Conference on Peaceful Uses of Atomic Energy*, 1958, pp. 184–187.

[59] S. Gerdung, P. Pihet, J. Grindborg, H. Roos, U. Schrewe, and H. Schuhmacher, "Operation and application of tissue equivalent proportional counters," *Radiation protection dosimetry*, vol. 61, no. 4, pp. 381–404, 1995.

[60] A. J. Waker, "Experimental uncertainties in microdosimetric measurements and an examination of the performance of three commercially produced proportional counters," *Nuclear Instruments and Methods in Physics Research Section A: Accelerators, Spectrometers, Detectors and Associated Equipment*, vol. 234, no. 2, pp. 354–360, 1985.

[61] S. H. Byun, A. Pejović-Milić, S. McMaster, W. Matysiak, Aslam, Z. Liu, L. M. Watters, W. V. Prestwich, F. E. McNeill, and D. R. Chettle, "Dosimetric characterization of the irradiation cavity for accelerator-based in vivo neutron activation analysis," *Physics in Medicine and Biology*, vol. 52, no. 6, p. 1693–1703, 2007.

[62] M. N. Varma, "Calibration of proportional counters in microdosimetry," Brookhaven National Lab., Tech. Rep., 1982.

[63] D. Srdoč, "Experimental technique of measurement of microscopic energy distribution in irradiated matter using rossi counters," *Radiation research*, vol. 43, no. 2, pp. 302–319, 1970.

[64] G. Dietze, H. Menzel, and G. Bühler, "Calibration of tissue-equivalent proportional counters used as radiation protection dosemeters," *Radiation Protection Dosimetry*, vol. 9, no. 3, pp. 245–249, 1984.

[65] T. Armstrong and K. Chandler, "SPAR, a FORTRAN program for computing stopping powers and ranges for muons, charged pions, protons, and heavy ions," *ORNL-4869, Oak Ridge National Laboratory*, 1973.

[66] J. Booz, P. Olko, T. Schmitz, K. Morstin, and L. Feinendegen, "The KFA counter, its photon and neutron responses and its potential for future developments," *Radiation Protection Dosimetry*, vol. 29, no. 1-2, pp. 87–92, 1989.

[67] C. Shalem, R. Chechik, A. Breskin, and K. Michaeli, "Advances in Thick GEM-like gaseous electron multipliers—Part I: atmospheric pressure operation," *Nuclear Instruments and Methods in Physics Research Section A: Accelerators, Spectrometers, Detectors and Associated Equipment*, vol. 558, no. 2, pp. 475–489, 2006.

[68] F. Sauli, "Gas detectors: achievements and trends," *Nuclear Instruments and Methods in Physics Research Section A: Accelerators, Spectrometers, Detectors and Associated Equipment*, vol. 461, no. 1, pp. 47–54, 2001.

[69] C. Shalem, R. Chechik, A. Breskin, K. Michaeli, and N. Ben-Haim, "Advances in thick GEM-like gaseous electron multipliers Part II: Low-pressure operation," *Nuclear Instruments and Methods in Physics Research Section A: Accelerators, Spectrometers, Detectors and Associated Equipment*, vol. 558, no. 2, pp. 468–474, 2006.

[70] R. Chechik, A. Breskin, C. Shalem, and D. Mörmann, "Thick GEM-like hole multipliers: properties and possible applications," *Nuclear Instruments and Methods in Physics Research Section A: Accelerators, Spectrometers, Detectors and Associated Equipment*, vol. 535, no. 1, pp. 303–308, 2004.

[71] M. Cortesi, R. Alon, R. Chechik, A. Breskin, D. Vartsky, and V. Dangendorf, "Investigations of a THGEM-based imaging detector," *Journal of Instrumentation*, vol. 2, no. 09, p. P09002, 2007.

[72] F. D. van den Berg, *Gas-filled micro-patterned radiation detectors*. TU Delft, Delft University of Technology, 2000.

[73] Z. Anjomani, A. R. Hanu, W. V. Prestwich, and S. H. Byun, "Monte Carlo design study for thick gas electron multiplier-based multi-element microdosimetric detector," *Nuclear Instruments and Methods in Physics Research Section A: Accelerators, Spectrometers, Detectors and Associated Equipment*, vol. 757, pp. 67–74, 2014.

[74] A. Hanu, "Development of a THGEM imaging detector with delay line readout," 2014.

[75] R. Veenhof, "Garfield, recent developments," *Nuclear Instruments and Methods in Physics Research Section A: Accelerators, Spectrometers, Detectors and Associated Equipment*, vol. 419, no. 2–3, pp. 726 – 730, 1998. [Online]. Available: http://www.sciencedirect.com/science/article/pii/S0168900298008511

[76] F. M. Khan and J. P. Gibbons, *Khan's the physics of radiation therapy*. Lippincott Williams & Wilkins, 2014.

[77] D. Srdoč, "Experimental Technique of Measurement of Microscopic Energy Distribution in Irradiated Matter Using Rossi Counters," *Radiation Research*, vol. 43, no. 2, pp. 302–319, Aug. 1970.

[78] Shared hierarchical academic research computing network (sharcnet). [Online]. Available: http://www.sharcnet.ca

[79] *ICRU report 49: Stopping Powers and Ranges for Protons and Alpha Particles*, ser. ICRU Report. Bethesda: International Commission on Radiation Units and Measurements, 1993.

[80] G. Leuthold, V. Mares, and H. Schraube, "Calculation of the neutron ambient dose equivalent on the basis of the icrp revised quality factors," *Radiation Protection Dosimetry*, vol. 40, no. 2, pp. 77–84, 1992.

[81] G. M. Spirou, S. H. Byun, and W. V. Prestwich, "Comparison of three pulse processing systems for microdosimetry," *IEEE Transactions on Nuclear Science*, vol. 55, no. 5, pp. 2621–2626, 2008.

[82] Z. Anjomani, A. Hanu, W. Prestwich, and S. Byun, "Development of a multi-element microdosimetric detector based on a thick gas electron multiplier," *Nuclear Instruments and Methods in Physics Research Section A: Accelerators, Spectrometers, Detectors and Associated Equipment*, vol. 847, pp. 117 – 124, 2017.

[83] A. Breskin, R. Alon, M. Cortesi, R. Chechik, J. Miyamoto, V. Dangendorf, J. Maia, and J. Dos Santos, "A concise review on THGEM detectors," *Nuclear Instruments and Methods in Physics Research Section A: Accelerators, Spectrometers, Detectors and Associated Equipment*, vol. 598, no. 1, pp. 107–111, 2009.

[84] A. Breskin, M. Cortesi, R. Alon, J. Miyamoto, V. Peskov, G. Bartesaghi, R. Chechik, V. Dangendorf, J. Maia, and J. dos Santos, "The THGEM: A thick robust gaseous electron multiplier for radiation detectors," *Nuclear Instruments and Methods in Physics Research Section A: Accelerators, Spectrometers, Detectors and Associated Equipment*, vol. 623, no. 1, pp. 132–134, 2010.

[85] M. Alexeev, R. Birsa, F. Bradamante, A. Bressan, M. Chiosso, P. Ciliberti, G. Croci, M. Colantoni, S. Dalla Torre, S. D. Pinto *et al.*, "THGEM based photon detector for cherenkov imaging applications," *Nuclear Instruments and Methods in Physics Research Section A: Accelerators, Spectrometers, Detectors and Associated Equipment*, vol. 617, no. 1, pp. 396–397, 2010.

[86] M. Alexeev, R. Birsa, F. Bradamante, A. Bressan, M. Büchele, M. Chiosso, P. Ciliberti, S. Dalla Torre, S. Dasgupta, O. Denisov *et al.*, "Progresses in the production of large-size THGEM boards," *Journal of Instrumentation*, vol. 9, no. 03, p. C03046, 2014.

[87] A. Waker, "Gas gain characteristics of some walled proportional counters used in microdosimetry," in *Proc. 8th Symp. on Microdosimetry (Jülich)*, 1983, pp. 1017–30.

[88] D. White, "Tissue substitutes in experimental radiation physics," *Medical physics*, vol. 5, no. 6, pp. 467–479, 1978.

[89] L. De Nardo and M. Farahmand, "Operation of gas electron multiplier GEM with propane gas at low pressure and comparison with tissue-equivalent gas mixtures," *Nuclear Instruments and Methods in Physics Research Section A: Accelerators, Spectrometers, Detectors and Associated Equipment*, vol. 819, pp. 154–162, 2016.

[90] M. Farahmand, A. Bos, and C. van Eijk, "Gas electron multiplier GEM operation with tissue-equivalent gases at various pressures," *Nuclear Instruments and Methods in Physics Research Section A: Accelerators, Spectrometers, Detectors and Associated Equipment*, vol. 506, no. 1, pp. 160–165, 2003.

[91] W. Matysiak, W. V. Prestwich, and S. H. Byun, "Measurement of the thick target ^{7}Li(p, n) neutron source spectrum using a ^{3}He ionization chamber," *Nuclear Instruments and Methods in Physics Research Section A: Accelerators, Spectrometers, Detectors and Associated Equipment*, vol. 592, no. 3, pp. 316–324, 2008.

[92] Aslam, W. Prestwich, F. McNeill, and A. Waker, "Monte Carlo simulation of neutron irradiation facility developed for accelerator based in vivo neutron

activation measurements in human hand bones," *Applied Radiation and Isotopes*, vol. 64, no. 1, pp. 63–84, 2006.

[93] Aslam, W. Prestwich, F. McNeill, and A. Waker, "Investigating the TEPC radiation quality factor response for low energy accelerator based clinical applications," *Radiation protection dosimetry*, vol. 103, no. 4, pp. 311–322, 2003.

[94] C. Lee and X.-L. Zhou, "Thick target neutron yields for the ^{7}Li(p, n)^{7}Be reaction near threshold," *Nuclear Instruments and Methods in Physics Research Section B: Beam Interactions with Materials and Atoms*, vol. 152, no. 1, pp. 1–11, 1999.

[95] A. Waker, "Performance of a high sensitivity multi-element tissue equivalent proportional counter for radiation protection neutron monitoring measurements," *Health physics*, vol. 98, no. 5, pp. 692–703, 2010.

[96] A. Pejović-Milić, M. Arnold, F. McNeill, and D. Chettle, "Monte carlo design study for in vivo bone aluminum measurement using a low energy accelerator beam," *Applied Radiation and Isotopes*, vol. 53, no. 4, pp. 657–664, 2000.

[97] A. Pejović-Milić, S. Byun, D. Chettle, F. McNeill, and W. Prestwich, "Development of an irradiation/shielding cavity for in vivo neutron activation analysis of manganese in human bone," *Journal of radioanalytical and nuclear chemistry*, vol. 269, no. 2, pp. 417–420, 2006.

[98] I. Bronic, "W values in propane-based tissue-equivalent gas," *Radiation protection dosimetry*, vol. 70, no. 1-4, pp. 33–36, 1997.

[99] M. Cortesi, V. Peskov, G. Bartesaghi, J. Miyamoto, S. Cohen, R. Chechik, J. Maia, J. dos Santos, G. Gambarini, V. Dangendorf *et al.*, "THGEM operation in Ne and Ne/CH4," *Journal of Instrumentation*, vol. 4, no. 08, p. P08001, 2009.

[100] R. Alon, J. Miyamoto, M. Cortesi, A. Breskin, R. Chechik, I. Carne, J. Maia, J. dos Santos, M. Gai, D. McKinsey *et al.*, "Operation of a thick gas electron

multiplier (thgem) in ar, xe and ar-xe," *Journal of Instrumentation*, vol. 3, no. 01, p. P01005, 2008.

[101] N. Qashua and A. Waker, "Study of the effect of high dose rate on tissue equivalent proportional counter microdosimetric measurements in mixed photon and neutron fields," *Nuclear Instruments and Methods in Physics Research Section A: Accelerators, Spectrometers, Detectors and Associated Equipment*, vol. 652, no. 1, pp. 854–857, 2011.

[102] C. Barth and C. Wernli, "Putting microdosimetry to work: The measurement campaigns of 1987 at KKG, KKL and PSI," *Radiation Protection Dosimetry*, vol. 23, no. 1-4, pp. 257–260, 1988.

[103] K. Folkerts, H. Menzel, H. Schuhmacher, and E. Arend, "TEPC radiation protection dosimetry in the environment of accelerators and at nuclear facilities," *Radiation Protection Dosimetry*, vol. 23, no. 1-4, pp. 261–264, 1988.

[104] H. Schuhmacher, "Tissue-equivalent proportional counters in radiation protection dosimetry: expectations and present state," *Radiation Protection Dosimetry*, vol. 44, no. 1-4, pp. 199–206, 1992.

[105] U. J. Schrewe, H. J. Brede, and G. Dietze, "Dosimetry in mixed neutron-photon fields with tissue-equivalent proportional counters," *Radiation Protection Dosimetry*, vol. 29, no. 1-2, pp. 41–45, 1989.

[106] S. Agosteo, "Overview of novel techniques for radiation protection and dosimetry," *Radiation Measurements*, vol. 45, no. 10, pp. 1171–1177, 2010.

[107] L. Periale, V. Peskov, P. Carlson, T. Francke, P. Pavlopoulos, P. Picchi, and F. Pietropaolo, "Detection of the primary scintillation light from dense Ar, Kr and Xe with novel photosensitive gaseous detectors," *Nuclear Instruments and Methods in Physics Research Section A: Accelerators, Spectrometers, Detectors and Associated Equipment*, vol. 478, no. 1, pp. 377–383, 2002.